Design and Development of High Performance III-Nitrides Photovoltaics

by

Xuanqi Huang

A Thesis Presented in Partial Fulfillment
of the Requirements for the Degree
Doctor of Philosophy

Approved March 2020 by the
Graduate Supervisory Committee:

Yuji Zhao, Chair
Stephen Goodnick
Richard King
Dragica Vasileska

ARIZONA STATE UNIVERSITY

May 2020

ABSTRACT

Wurtzite (In, Ga, Al) N semiconductors, especially InGaN material systems, demonstrate immense promises for the high efficiency thin film photovoltaic (PV) applications for future generation. Their unique and intriguing merits include continuously tunable wide band gap from 0.70 eV to 3.4 eV, strong absorption coefficient on the order of $\sim 10^5$ cm^{-1}, superior radiation resistance under harsh environment, and high saturation velocities and high mobility. Calculation from the detailed balance model also revealed that in multi-junction (MJ) solar cell device, materials with band gaps higher than 2.4 eV are required to achieve PV efficiencies greater than 50%, which is practically and easily feasible for InGaN materials. Other state-of-art modeling on InGaN solar cells also demonstrate great potential for applications of III-nitride solar cells in four-junction solar cell devices as well as in the integration with a non-III-nitride junction in multi-junction devices.

This dissertation first theoretically analyzed loss mechanisms and studied the theoretical limit of PV performance of InGaN solar cells with a semi-analytical model. Then three device design strategies are proposed to study and improve PV performance: band polarization engineering, structural design and band engineering. Moreover, three physical mechanisms related to high temperature performance of InGaN solar cells have been thoroughly investigated: thermal reliability issue, enhanced external quantum efficiency (EQE) and conversion efficiency with rising temperatures and carrier dynamics and localization effects inside nonpolar *m*-plane InGaN quantum wells (QWs) at high temperatures. In the end several future work will also be proposed.

Although still in its infancy, past and projected future progress of device design will ultimately achieve this very goal that III-nitride based solar cells will be indispensable for today and future's society, technologies and society.

ACKNOWLEDGMENTS

It has truly been a great pleasure and honor to complete this thesis under the guidance of my advisor Professor Yuji Zhao. His comprehensive knowledge of physics, rigorous style of work and sincere support have been a deep and constant inspiration not only to my research work, but also to my personal life. I'd also express my gratitude to my committee members: Prof. Stephen M. Goodnick, Prof. Richard R. King and Prof. Dragica Vasileska, for their constructive assistance and advice during my PhD study.

For the past five years I have been lucky enough to obtain timely and sufficient support from colleague students, researchers and friends. I want to thank all of our group members: Dr.Zhijian, Dr.Houqiang, Hong, Xiaodong, Jossue, Tsung-Han, Chen, Jingan, Dr.Kai, Xuguang and Xin, for all of the invaluable discussion and help. I'm also grateful for my collaborators at ASU: Jia Ding, Dr.Jacob Becker and Prof.Yong-Hang Zhang for photovoltaic measurements, Dongying Li, Dr.Lin Gan and Prof.Cun-Zheng Ning for PL and TRPL studies, Po-Yi Su and Prof. Fernando Ponce for STEM study, Dr.Yi Fang for simulation on solar cells and Dr.Chaomin Zhang and Prof. Christiana Honsberg for help on III-V solar cells. I'd also like to give special thanks to our collaborators off campus: Dr.Ding Ding, Dr. Wei Li and Prof. Shanhui Fan from Stanford, Dr. Brendan P. Gunning and Dr.Daniel D. Koleske from Sandia National Laboratories, Dr.Carlo De Santi from University of Padova. In addition, I want to sincerely thank every friend I met at ASU.

I would like to acknowledge dedicated staff from ASU NanoFab and LeRoy Eyring Center, and the funding support from NASA and NSF.

Finally, I am forever indebted to my parents, my family, my girlfriend Yiran Zhang and her parents. Your unconditional and everlasting love shapes me into the person I am today, empowering me to become better throughout the years.

TABLE OF CONTENTS

Page

LIST OF TABLES

Table Page

LIST OF FIGURES

Figure Page

Figure Page

CHAPTER 1

INTRODUCTION

1.1 Polar, nonpolar and semipolar III-nitrides

Wurtzite (In, Ga, Al) N semiconductors, especially InGaN material systems, demonstrate immense promises for the high efficiency thin film photovoltaic (PV) applications for future generation.[1] Their unique and intriguing merits include continuously tunable wide band gap from 0.70 eV to 3.4 eV, strong absorption coefficient on the order of $\sim 10^5$ cm^{-1}, superior radiation resistance under harsh environment, and high saturation velocities and high mobility.[2] Calculation from the detailed balance model also revealed that in multi-junction (MJ) solar cell device, materials with band gaps higher than 2.4 eV are required to achieve PV efficiencies greater than 50%, [3] which is practically and easily feasible for InGaN materials. Other state-of-art modeling on InGaN solar cells also demonstrate great potential for applications of III-nitride solar cells in four-junction solar cell devices as well as in the integration with a non-III-nitride junction in multi-junction devices. [4]–[6]

Different crystal planes of wurtzite GaN are shown in Fig.1.1. We can categorize them into polar planes such as (0001) or *c*-plane, nonpolar planes such as $(10\bar{1}0)$, and semipolar planes such as $(30\bar{3}1)$, $(20\bar{2}1)$, $(10\bar{1}1)$, $(10\bar{1}\bar{1})$ and $(11\bar{2}2)$. For *c*-plane devices, strong polarization-induced electric field exists inside the InGaN QWs, which will result in significant energy band tilting, a phenomenon known as quantum-confined Stark effect (QCSE). This distorted band diagram will greatly decrease the electron and hole's wavefunction overlap which will reduce the efficiency of LEDs. In contrast, nonpolar or

semipolar InGaN quantum wells (QWs) have eliminated or reduced QCSE, which will lead to a flatter QW profile and higher wavefunction overlap.

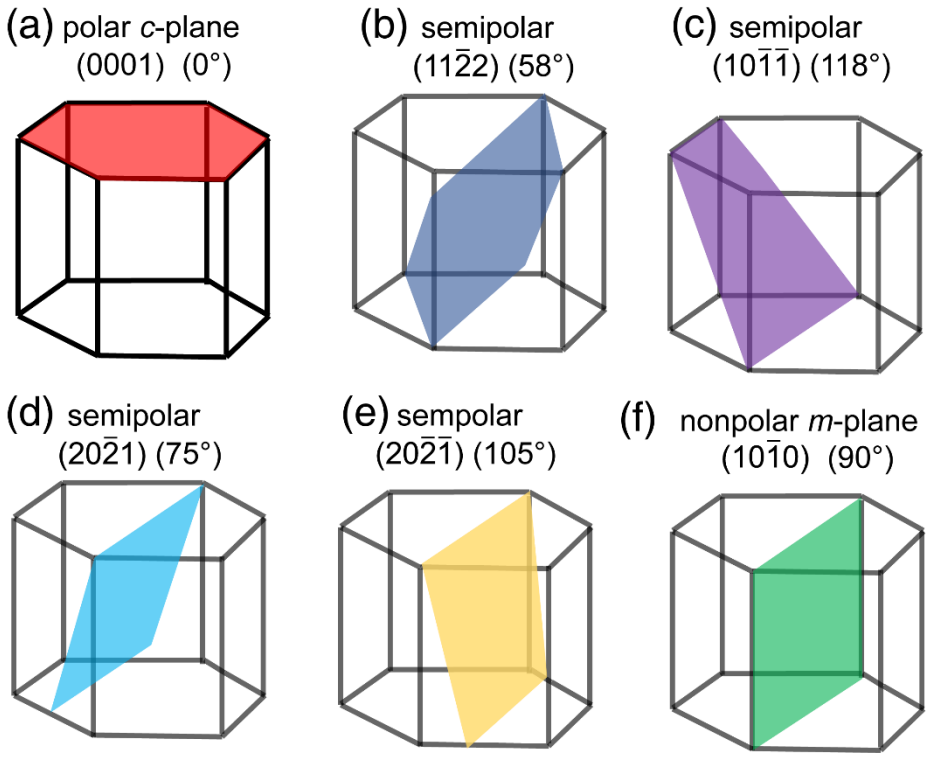

Figure 1.1. Schematics of (a) polar (*c*-plane), semipolar (b) $(11\bar{2}2)$, (c) $(10\bar{1}\bar{1})$, (d) $(20\bar{2}1)$, and (e) $(20\bar{2}\bar{1})$) and (f) nonpolar plane (*m*-plane) of III-nitride wurtzite crystal structure. The degrees indicate the inclination angles of the nonpolar and semipolar planes from *c*-plane. Adapted from reference[7].

Due to the lack of inversion symmetry, wurtzite III-nitride materials have strong spontaneous polarization along the [0001] *c*-axis. When InGaN QWs are coherently grown on GaN, the lattice-mismatch induced strain will also result in piezoelectric polarization. The combination of spontaneous polarization and piezoelectric polarization difference at the InGaN/GaN interface induces strong electric fields inside the InGaN QWs. A vivid example of surface charges and directions of electric field and polarization field for

spontaneous and piezoelectric polarization in III-nitride heterojunction is depicted in Figure 1.2. We can see from Fig.1.2 that the total polarization-induced field is in the opposite direction to the built-in field in the p-n junction, considering that fact that epitaxial growth usually starts with n-type layers on substrates first and finishes with p-type layers on top.

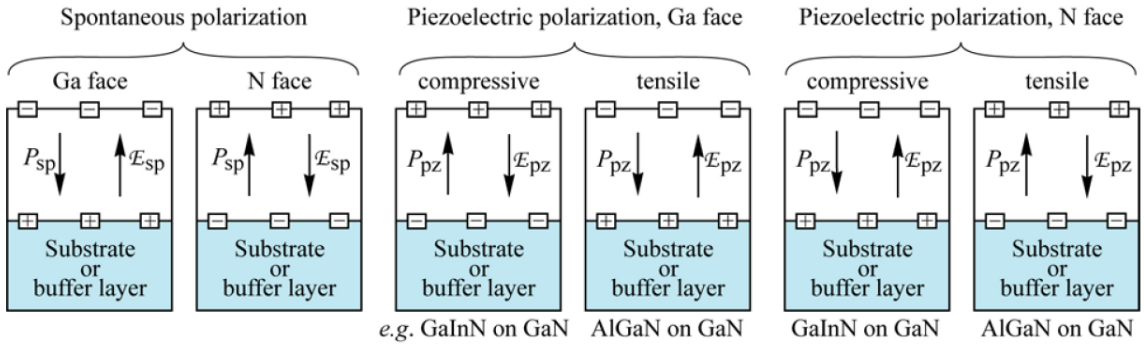

Figure 1.2. Surface charges and directions of electric field and polarization field for spontaneous and piezoelectric polarization in III-nitride heterojunction for Ga and N face [(0001) and $(000\bar{1})$]. Adapted from reference[8].

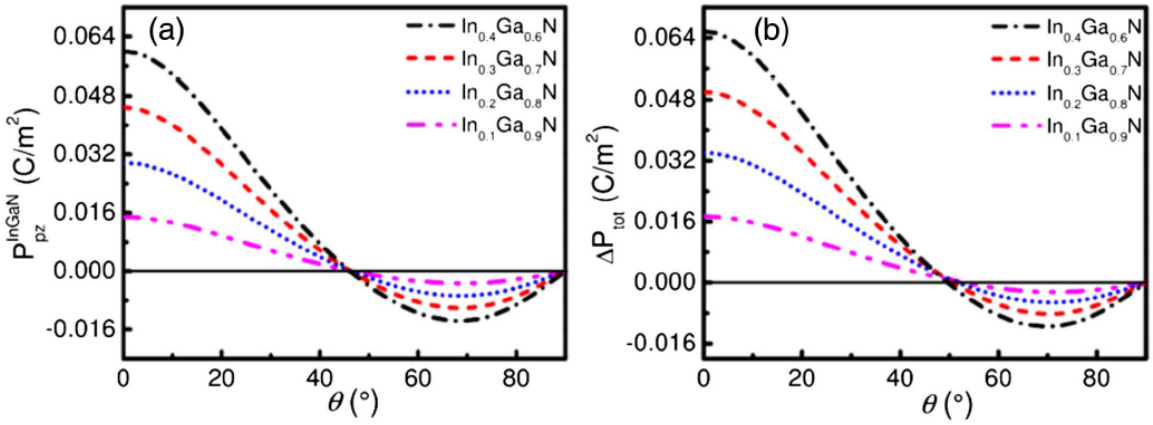

Figure 1.3. Calculated (a) piezoelectric polarization P_{pz} and (b) total polarization difference ΔP_{tot} as a function of semipolar plane orientation θ for InGaN/GaN heterostructure with In composition of 10%, 20%, 30% and 40%. Adapted from reference[7].

The polarizations of *c*-plane and nonpolar/semipolar planes can be calculated analytically by a recent method proposed by Romanov *et al* [1]. The primed coordinate z' is along the growth direction and x' and y' are in the substrate surface plane. For a plane titled from *c*-plane by an angle of θ, the total polarization difference along z' at InGaN/GaN interface can be expressed as a function of θ by

$$\Delta P_{tot} = P_{pz}^{InGaN} + (P_{sp}^{InGaN} + P_{sp}^{GaN})\cos\theta \tag{1.1}$$

where ΔP_{tot} is the total polarization difference between InGaN layer and GaN substrate, and P_{sp}^{InGaN} and P_{sp}^{GaN} are the spontaneous polarization of InGaN layer and GaN substrate, respectively. P_{pz}^{InGaN} is the strain-induced piezoelectric polarization in InGaN layer, which be expressed as

$$\begin{aligned} P_{pz}^{InGaN} = {} & e_{31}\cos\theta\,\varepsilon_{x'x'} + \left(e_{31}\cos^3\theta\,\varepsilon_{x'x'} + \frac{e_{33}-e_{15}}{2}\sin\theta\sin 2\theta\right)\varepsilon_{y'y'} \\ & + \frac{e_{33}+e_{15}}{2}\sin\theta\sin 2\theta + e_{33}\cos^3\theta)\varepsilon_{z'z'} \\ & + [(e_{31}-e_{33})\cos\theta\sin 2\theta + e_{15}\sin\theta\cos 2\theta]\varepsilon_{y'z'} \end{aligned} \tag{1.2}$$

where elements $\varepsilon_{k'm'}$ are the strain tensor components and elements e_{ij} are the components of piezoelectric tensor in Voigt notation. Figure 1.3 presents the P_{pz}^{InGaN} and ΔP_{tot} of InGaN/GaN with different indium composition as a function of θ. Since the P_{pz}^{InGaN} is dominant for InGaN/GaN heterostructure, ΔP_{tot} shows the minimal change with the addition of spontaneous polarization. ΔP_{tot} becomes zero at θ=45° (semipolar plane) and θ=90° (nonpolar plane). The two crossovers are almost not impacted by the indium composition. The polarization (absolute value) of several common GaN crystal planes are compared as following: *c*-plane (0001) > $(10\bar{1}\bar{1})$ > $(20\bar{2}1)$ = $(20\bar{2}\bar{1})$ > $(11\bar{2}2)$.

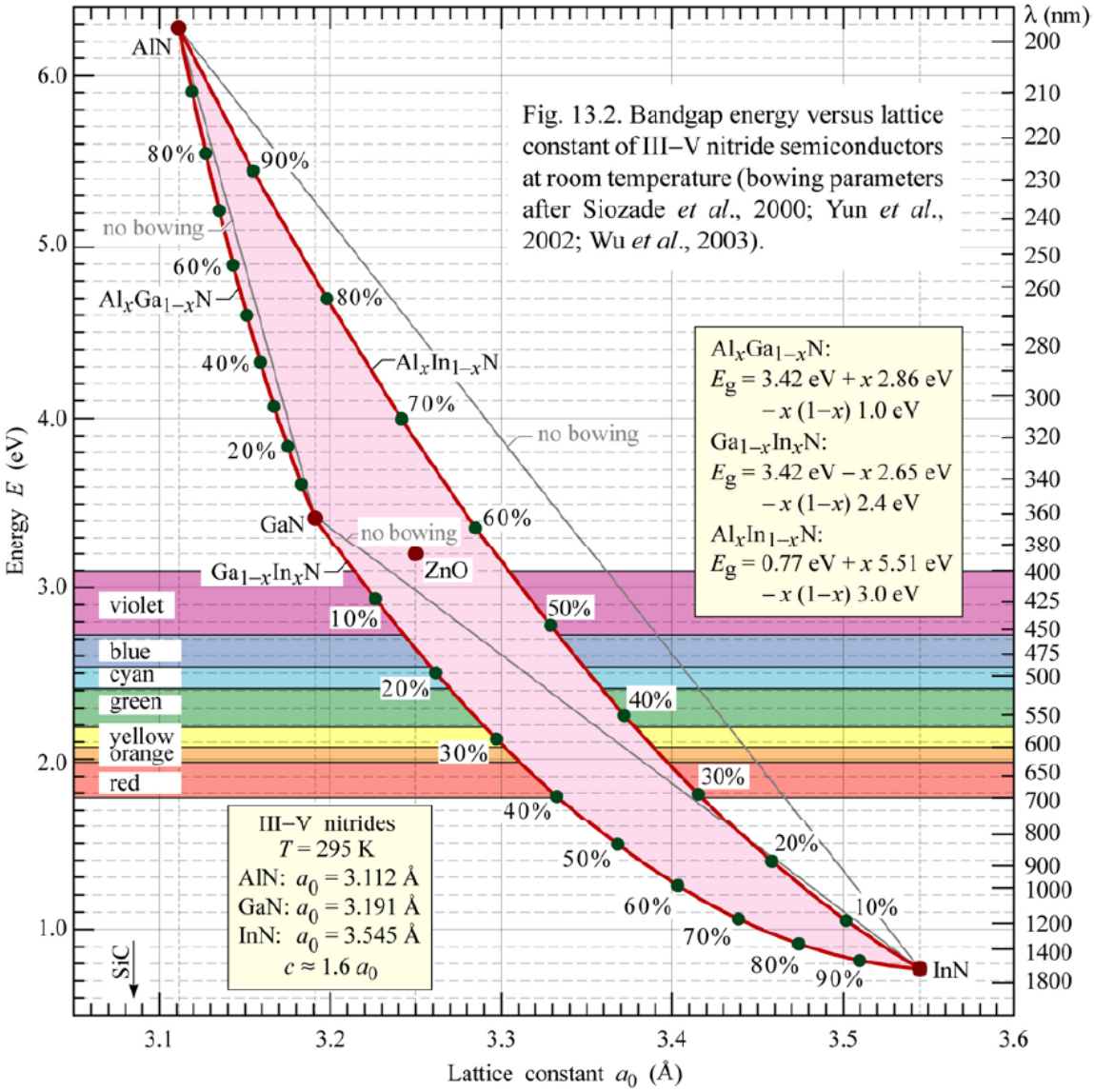

Figure 1.4. Bandgap energy versus lattice constant of III-nitrides at room temperatures. Adapted from reference[8].

1.2 Review of the state-of-the-art InGaN solar cells

The research interests in developing InGaN-based photovoltaics (PV) stems from their unique material properties. The InGaN alloys have been predicted as a fine candidate for full-solar spectrum PV applications due to the wide range of bandgap energies (~ 0.6 eV for InN and ~3.4eV for GaN) [2], as shown in Fig.1.4. In addition, they also have

outstanding thermal performance, and superior radiation resistance under harsh environments [2]. The early demonstrations of InGaN solar cells have been mainly based on bulk InGaN layers with either *p-i-n* or *p-n* structures [3], [9]–[14]. The common features of these cells with bulk InGaN layers lie in the low open-circuit voltage (V_{OC}) and the relatively high short-circuit current density (J_{SC}) values. Typical V_{OC} lower than 2 V as well as large voltage-bandgap offsets (W_{OC}) in such structures can be attributed to the low quality of the InGaN absorbing layers. Due to the large lattice mismatch between InN and GaN as well as the low indium miscibility in GaN, it has been experimentally difficult to preserve film quality while maintaining high indium incorporation and thick InGaN layer. Furthermore, the use of foreign substrates such as sapphire and Si exacerbates the material quality of InGaN and result in basal stacking faults and threading dislocations in an order of 10^9-10^{10} cm^{-3}. As a result, the indium mole fraction in the reported InGaN solar cells is generally below 20%, which corresponds to a bandgap energy of ~ 2.5 eV and a cut-off wavelength of ~ 500 nm. The trend of decreasing V_{OC} with increasing indium content is clearly shown in Fig.13 in the reference [4].

Therefore, the majority of research and progress in InGaN-based solar cells have been demonstrated in p-GaN/ InGaN / n-GaN heterojunction structures where multi-quantum wells (MQWs) or superlattice (SL) is employed [15]–[54]. The film quality of InGaN absorbing layers is thus better maintained in MQWs since each InGaN layer is below critical thickness and also strained in each QW period. Consequently InGaN solar cells with MQWs or SL generally exhibit V_{OC} values larger than 2 V and small W_{OC} of around 0.5 V despite relatively low J_{SC}. Transport and collection of photogenerated carriers inside QWs would be severely impacted if the barrier is too thick and the QW structure is

not properly designed, leading to a low J_{SC} and low fill factor (FF). Nonetheless, a total thickness of InGaN layers greater than 200 nm is required for the complete absorption of incoming sun light, which still remains a great hurdle even with MQWs or SL structures.

Moreover, InGaN solar cells have demonstrated superior PV performance under concentrated sunlight conditions [30], [17], [49], [55], [56] and at high temperatures [37], [40], [44], [49], [57], [58]. These reports have characterized and revealed the positive temperature coefficients of J_{SC}, FF and power conversion efficiency in certain ranges temperatures and concentrating ratios, in addition to superior thermal robustness. It's also worth noting that a four-junction (4J) solar cell with InGaN top cell has been demonstrated for the first time using wafer bonding technique [59]. The PV performance of the 4J cell will be expected to be greatly enhanced if the bonding process is optimized and the current matching is taken into consideration.

1.3 Dissertation synopsis

In the following of this thesis, we will propose and demonstrate solutions to improve the PV performance of InGaN solar cells, as well as analyze underlying physical mechanisms. Part of this thesis have been previously published in several journals [58], [60]–[64].

In Chapter 2, we will propose a semi-analytical model for solar cells to investigate the optical property, efficiency limits, and loss mechanisms in InGaN PV solar cells.

Chapter 3 studies the nonpolar and semipolar InGaN/GaN MQW solar cells. The solar cell performance showed a strong dependence on the polarization-related effects, where nonpolar m-plane solar cells exhibited the best PV performance due to the

eliminated polarization effects, which were further confirmed by bias-dependent EQE measurements and energy band diagram simulations.

Chapter 4 introduces the growth, characterizations and optimization of InGaN/GaN MQW solar cell devices. Both PV performance at RT and elevated temperatures are shown.

In Chapter 5, we demonstrate that energy band engineering of InGaN multi-quantum-well (MQW) solar cells using AlGaN electron- and hole-blocking layers enables the improving PV performance. These results indicate band engineering with AlGaN layers in the InGaN MQW solar cell structures can effectively enhance the carrier collection process and is a promising design for high efficiency InGaN solar cells for both room temperature and high temperature PV applications.

Chapter 6 discusses thermal stability of InGaN solar cells are investigated under thermal stress at elevated temperatures from 400°C to 500°C. Experimental results suggest that while InGaN solar cells have high thermal stability, the degradation in metal contact could be the major limiting factor for these devices under high temperature operation.

In Chapter 7, we demonstrate that the nonpolar InGaN solar cells showed a large working temperature range from room temperature (RT) to 450°C, with positive temperature coefficients up to 350°C. Using a mechanically-stacked tandem structure, we also demonstrated that the InGaN-GaAs tandem solar cell outperformed the sole GaAs solar cell at high temperatures beyond 350°C.

Chapter 8 analyzes different carrier dynamics of two nonpolar *m*-plane InGaN/GaN QWs at high temperatures by combining scanning transmission electron microscopy (STEM) and photophysical characterization. In addition detailed analysis on exciton-phonon scattering mechanisms reveals that both acoustic and optical phonon scatterings

play the dominant roles in the range of 300-600 K and afterwards impurity scattering is the main mechanism responsible for FWHM broadening.

Finally, we present the summary and conclusions in Chapter 9. Several future work topics will also be discussed to further enhance the performance of InGaN solar cells and realize its full potential for specific applications.

CHAPTER 2

ANALYSIS OF LOSS MECHANISMS IN INGAN SOLAR CELLS USING A SEMI-ANALYTICAL MODEL

Wurtzite (In, Ga, Al)N semiconductors, especially InGaN material systems, demonstrate immense promises for the high efficiency thin film photovoltaic (PV) applications for future generation[1]. Their unique and intriguing merits include continuously tunable wide band gap from 0.70 eV to 3.4 eV, strong absorption coefficient on the order of $10^5 cm^{-1}$, superior radiation resistance under harsh environment, and high saturation velocities and high mobility[2]. Calculation from the detailed balance model also revealed that in multi-junction solar cell device, materials with band gaps higher than 2.4 eV are required to achieve PV efficiencies greater than 50%[3], which is practically and easily feasible for InGaN materials. Other state-of-art modeling on InGaN solar cells also demonstrate great potential for applications of III-nitride solar cells in four-junction solar cell devices as well as in the integration with a non-III-nitride junction in multi-junction devices[4], [6], [65]. However, due to distinct material properties from conventional III-V PV materials, the fundamental PV processes and corresponding loss mechanisms in InGaN solar cells are still not well understood. It is therefore imperative to investigate the major loss mechanism in InGaN solar cells for the design and optimization of high efficiency InGaN solar cells.

In this work, a semi-analytical model for solar cells[66] is adopted to investigate the optical property, efficiency limits and loss mechanisms in InGaN PV solar cells. Compared to commercial software such as Silvaco or Crosslight, this model requires less time to calculate and is capable of revealing the intrinsic physical reasons straightforwardly.

In the simulation, we also incorporate non-ideal properties such as photon recycling, spontaneous emission coupling, the non-step absorptance and emittance of junctions and absorption tails below the bandgap. The equations and details of these non-ideal properties can be found in Ref. 7. These factors are all accounted for complicated physical processes in real solar cells. The efficiencies and device performance are calculated for four different solar cell structures, and the loss mechanisms are examined thoroughly to provide basic guidance for the design of InGaN solar cells.

We focus on four major loss mechanisms [66], [67] in InGaN solar cells: (i) transmission losses due to photons transmitting through the device without being absorbed; (ii) thermalization losses resulting from carriers in excited states returning to band edges; (iii) spatial relaxation losses due to carriers losing potential energy while being separated and collected at the contacts; and (iv) recombination losses due to Shockley-Read-Hall (SRH) and Auger recombination. [68] The expressions and details of losses and extracted power can be referred to Ref. 9. In order to focus on the intrinsic properties of materials and devices, this study do not take into account other losses, for instance, surface recombination, series resistance, and shunt resistance, which are closely related to the device fabrication process. The total current density of a single junction (1J) solar cell is given as

$$J_{total} = J_{sc} - J_{rad} - J_{SRH} - J_{Auger} \tag{2.1}$$

where Jsc is the short-circuit current density that is mainly determined by the absorptance of the cell, including below- bandgap absorption; J_{rad}, J_{SRH}, and J_{Auger} are the radiative, SRH, and Auger recombination current density, respectively.

2.1 Simulation methods and Optical properties

Figure 2.1 presents four planar structures with different surface configurations that are simulated in the analysis. Structure A and C both have the non-reflective interface between semiconductor and substrate with smooth (structure A)/textured upper surface (structure C), respectively; structure B and D both have 100% ideal reflective lower interface with smooth (structure B)/textured (structure D) upper surface, respectively. All of these structures are commonly used in InGaN solar cells while more complicated planar structures were explored in Ref. [69]. Note that in this work, upper surface corresponds to the front surface facing incident sunlight and lower surface indicates the bottom surface of a semiconductor attaching to the substrate. For InGaN solar cells, structure A is first proposed in Ref. [3] and is widely adopted due to the simple fabrication processes, while structure C is proven to be more effective to trap light and improve the device performance, both in conventional PIN structure and in quantum well structure. [18], [55], [70], [71] Note that for textured upper surface widely used in InGaN solar cells and light emitting diodes (LEDs), they are applied on the top layers like contacts or anti-reflecting layers. Structure B and D are investigated for comparison.

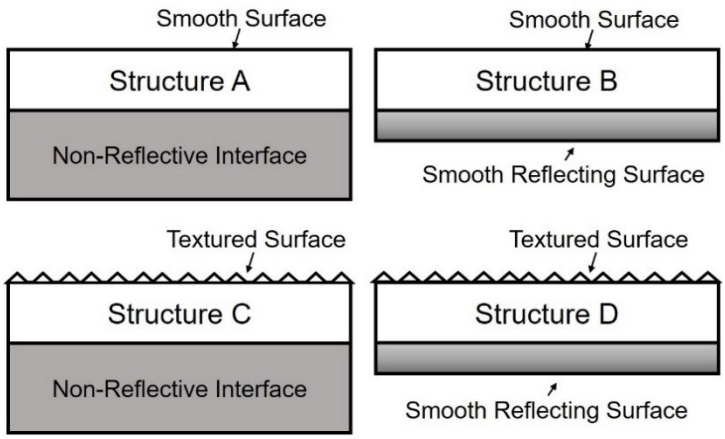

Figure. 2.1. Schematic diagrams of four planar solar cell structures used in the study

The AM1.5G solar spectrum is used in the calculation. $In_{.15}Ga_{.85}N$ is employed as the active layer for the study and published material parameters of bandgap energy Eg, [72] refractive index n_r, [73] and Urbach tail energy Eu =0.050 eV (Ref. [74]) are adopted. From statistical ray optics, the analytical equations of the absorptance are derived as follows:

$$A_\alpha \cong 1 - e^{-\alpha \cdot d}, \text{for structure A,} \tag{2.2}$$

$$A_\alpha \cong 1 - e^{-\alpha \cdot 2d}, \text{for structure B,} \tag{2.3}$$

$$A_\alpha = 1 - t_\alpha, \text{for structure C,} \tag{2.4}$$

$$A_\alpha = 1 - \frac{1 - t_\alpha}{1-(1-\frac{1}{n_r^2})t_\alpha}, \text{ for structure D,} \tag{2.5}$$

where α is the absorption coefficient, d is the semiconductor thickness, n_r is the refractive index, and t_α indicates the fraction of lost photons in a single pass through the slab, with

$$t_\alpha = \int_0^{\pi/2} e^{-\alpha \cdot d/cos\theta} 2cos\theta sin\theta d\theta \text{ , for structure C,} \tag{2.6}$$

$$t_\alpha = \int_0^{\pi/2} e^{-2\alpha \cdot d/cos\theta} 2cos\theta sin\theta d\theta \text{ , for structure D,} \tag{2.7}$$

where θ is the angle between the scattered light and the surface normal. By assuming the Lambertian scattering, the portion of light distributed in the solid angle $sin\theta d\theta$ is $2cos\theta$, which could also be modified by other scattering functions other than Lambertian scattering. The upper- and lower-surface emittance is given by

$$\varepsilon_{upper} = 1 - n_r^2 \int_0^{\pi/2} e^{-\alpha \cdot d/cos\theta} 2cos\theta sin\theta d\theta \text{ , for structure A,} \tag{2.8}$$

$$\varepsilon_{lower} = 1 - \int_0^{\theta_c} e^{-\alpha \cdot d/cos\theta} 2cos\theta sin\theta d\theta - \int_{\theta_c}^{\pi/2} e^{-2\alpha \cdot d/cos\theta} 2cos\theta sin\theta d\theta \text{ ,}$$
$$\text{for structure A,} \tag{2.9}$$

$$\varepsilon_{upper} = 1 - n_r^2 \int_0^{\pi/2} e^{-\alpha \cdot 2d/cos\theta} 2cos\theta sin\theta d\theta \text{ , for structure B,} \tag{2.10}$$

$$\varepsilon_{lower} = 0 \text{ ,for structure B and D,} \tag{2.11}$$

$$\varepsilon_{upper} = A_\alpha \text{ ,for structure C and D,} \tag{2.12}$$

$$\varepsilon_{lower} = (1 - t_\alpha)[1 + (1 - \frac{1}{n_r^2})t_\alpha], \text{ for structure C and D,} \tag{2.13}$$

where θ_c is the critical angle. When the solar light is incident from all angles, the emittance is equal to absorptance. [66] In structure C and D with same textured surfaces, the upper surface emittance is equivalent to absorptance due to the same absorption and emission path of incident light, while there is zero emittance of lower surface because of the reflecting substrate in structure C and D. In comparison, for structure A and B with same smooth upper surface, the emittance is somewhat larger than absorptance because of shorter absorption ray path compared to emission. The energy dependent effective absorptance and emittance are defined as

$$\bar{A}_\alpha = \frac{\int_0^\infty A_\alpha \cdot n_{sun} \cdot dh\nu}{\int_{E_g - E_u}^\infty n_{sun} \cdot dh\nu} \tag{2.14}$$

$$\bar{\varepsilon}_{upper} = \frac{\int_0^\infty \varepsilon_{upper} \cdot (n_{\nu,sp} - n_{\nu,bb}) \cdot (h\nu)^2 \, dh\nu}{\int_{E_g - E_u}^\infty (n_{\nu,sp} - n_{\nu,bb}) \cdot (h\nu)^2 \, dh\nu} \tag{2.15}$$

$$\bar{\varepsilon}_{lower} = \frac{\int_0^\infty \varepsilon_{lower} \cdot (n_{\nu,sp} - n_{\nu,bb}) \cdot (h\nu)^2 \, dh\nu}{\int_{E_g - E_u}^\infty (n_{\nu,sp} - n_{\nu,bb}) \cdot (h\nu)^2 \, dh\nu} \tag{2.16}$$

where n_{sun} refers to the solar photon flux density per unit area and $n_{\nu,sp}$ and $n_{\nu,bb}$ are photon occupation numbers of spontaneous emission and blackbody emission, respectively. Note that this model incorporates below-bandgap tail absorption that is substantial in the practical situation, which is different from detailed balance model that assumes step-like emittance and absorptance identical to emittance. Figure 2.2 presents the (a) effective absorptance and (b) emittance under AM1.5G spectrum as a function of physical thickness

for four types of structures of $In_{.15}Ga_{.85}N$. For a given device thickness, structure D has much higher absorptance than structure A, B, and C, due to both textured surface and reflecting substrate, which strongly enhances light trapping and photon recycling processes. The absorptance of structure B and C is higher than that of structure A, indicating that both textured surface roughening and reflecting substrate are effective ways to enhance the absorptance, while structure B (reflecting substrate) is slightly better than structure C (textured surface). Moreover, for the same absorptance, structures A, B, and C require much larger device thickness due to limited optical path of light scattering and reflecting. Figure 2(b) shows that the emittance of upper surface of structures A, B, and C is much smaller than that of structure D. It is noteworthy that the emittance of lower surfaces of structure A and C is higher than that of upper surfaces. This is attributed to the adoption of non-reflective substrates, which gives rise to larger radiation loss in the solar cells. As a result, recent reports on high efficiency InGaN solar cells have been focusing on surface roughening (textured surface) rather than structures with smooth surface and substrate. [18], [55], [70], [71] Other optoelectronic devices have been more inclined to employ pattern sapphire substrates (PSS) to enhance light extraction. [75]–[79] Furthermore, despite costly and complicated growth and fabrication process, there have been reports proposing using diffraction grating on the back of the device for InGaN solar cells to enhance the optical absorption, 23 which combines the textured surface and reflecting substrate. These reports are also consistent with our findings here.

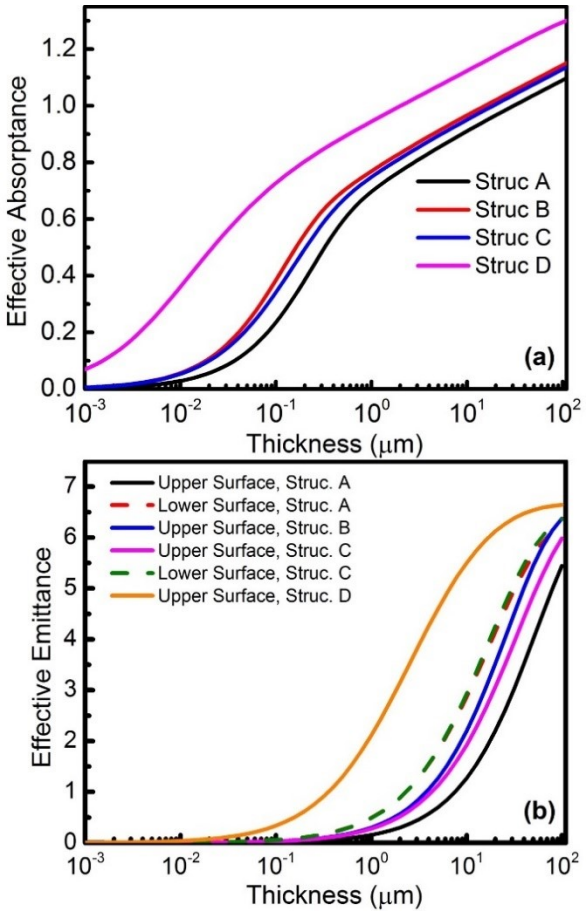

Figure. 2.2. (a) Effective absorptance vs. physical thickness and (b) effective emittance vs. physical thickness for $In_{0.15}Ga_{0.85}N$ solar cells in four structures.

Figure 2.3 presents effective emittance as a function of effective absorptance, i.e., optical thickness, using different (a) effective bandgaps and (b) Urbach energy (Eu) values as integration boundaries for upper surface in structure C. In this work, the effective emittance represents how many Urbach tail states would contribute to radiative recombination. Since Urbach tail energy (Eu) of III-nitrides is normally larger than that of GaAs [80] and Si [81], it is assumed that the variations of emittance of III-nitrides would be much more pronounced than those of GaAs and Si. Therefore, it is imperative to study different effective band gaps for integration boundaries to investigate the impacts on

optical properties and device performance of InGaN solar cells. In the calculation, different effective bandgaps and Urbach energy values have been applied, with integration boundary of Eg-Eu and Eu = 0.050 eV remaining the same, respectively. In Fig. 2.3(a), the effective emittance of upper surface maintains almost the same before effective absorptance of 0.8. Afterwards, the effective emittance gradually increases as Urbach tail energy (Eu) goes up. This trend suggests that within certain optical thickness, the value of Eu has little influence on the effective emittance. Meanwhile in Fig. 2.3(b), similar trends are also observed. As effective bandgap goes down, namely, more tail states contribute to radiative recombination, the effective emittance exceeds one and rises dramatically, which could be attributed to the facts that the effective band gap approaches the optimal bandgap of a single junction (1J) solar cell of about 1.4 eV (Ref. [82]) and much more emission would be generated than in an ideal semiconductor with band edge at Eg-Eu. It is noticeable that Eu is easily affected by extrinsic factors, for instance, the material quality of active layers, defect states, doping density, local stress, [83], [84] and device temperatures under operation, [85] which indicates that it would change under particular circumstances, even as high as 60meV. [74]

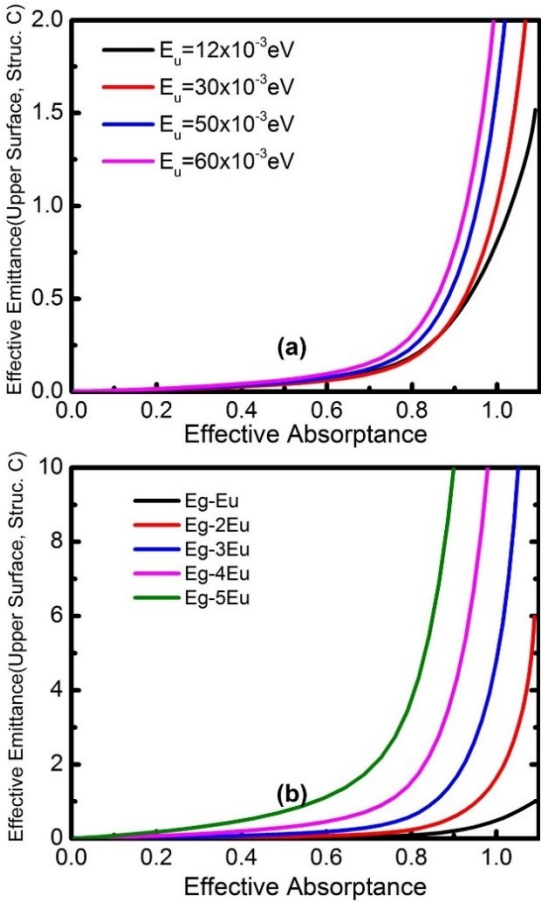

Figure. 2.3. Effective emittance vs. optical thickness using different (a) effective bandgaps and (b) Urbach energy values as integration boundaries, both for upper surface in structure C.

2.2 Analysis of loss mechanisms in single junction solar cell

In this section, we study the PV performance and loss mechanisms in single junction (1J) InGaN solar cells. Instead of physical thickness, the effective absorptance, i.e., the optical thickness, is explored in this part. The SRH recombination current densities per unit length (J_A/d) and Auger recombination current density per unit length (J_C/d) are calculated based on Ref. 9. Figure 2.4(a) presents the energy conversion efficiency as a function of absorptance for single junction $In_{0.15}Ga_{0.85}N$ solar cells in structure C with

various SRH recombination current densities per unit length (J_A/d). An energy conversion efficiency of 7.35% is obtained for typical reported material quality ($J_A/d = 1000\ Acm^{-2}\mu m^{-1}$), while the peak efficiency of 8.81% can be achieved for ideal materials ($J_A/d = 1\ Acm^{-2}\mu m^{-1}$). Therefore, improving InGaN quality offers an efficient method to increase the solar cell efficiency. In Fig. 2.4(b), the losses and efficiency distribution were extracted for single junction In0.15Ga0.85N solar cells with structure C under AM 1.5G one sun condition. Apparently, transmission loss dominates among all loss mechanisms due to large bandgap energy of III-nitrides than other III-V materials. The thermalization and spatial relaxation loss both rise with increasing effective absorptance due to larger portion of absorbed photons at larger thickness. It is noteworthy that the SRH loss accounts for most of the total recombination-related loss mechanisms, even though there are radiative loss generated from the loss of photon energies larger than bandgap (no reflecting surface employed in structure C) and Auger recombination loss owing to fairly large Auger recombination current density.

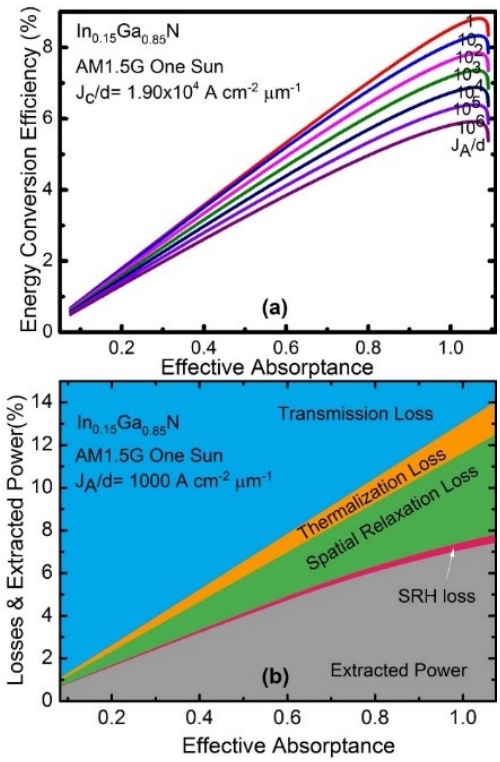

Figure. 2.4. (a) Energy conversion efficiency vs. effective absorptance (i.e., optical thickness) for 1J $In_{0.15}Ga_{0.85}N$ solar cells in structure C with particular SRH recombination current densities per unit length, J_A/d. (b) Losses and extracted power vs. absorptance for single junction In0.15Ga0.85N solar cell under AM 1.5G one sun condition, assuming SRH recombination current density per unit length $J_A/d = 1000\ Acm^{-2}\mu m^{-1}$.

Figure 2.5(a) demonstrates energy conversion efficiency as a function of SRH recombination current densities per unit length (J_A/d) for four structures with typical Auger recombination current density per unit length ($J_C/d = 1.9 \times 10^4\ Acm^{-2}\mu m^{-1}$). When J_A/d is lower than $1000\ Acm^{-2}\mu m^{-1}$, the conversion efficiency shows minimum difference. As J_A/d increases, the conversion efficiencies decrease collectively for all structures. These results reveal that SRH recombination plays a key role in degrading the conversion efficiency for InGaN solar cells. Furthermore, Fig. 2.5(b) illustrates the losses

and efficiency map for single junction In0.15Ga0.85N solar cells in structure C under AM 1.5G one sun condition. For clarity, we plot the losses and efficiency map only to 20% while transmission loss still dominates in the losses part that is not shown. Both transmission and thermalization losses remain almost constant over all J_A/d range at the given structure, while spatial relaxation loss accounts for the degradation of conversion efficiency as J_A/d is greater than 0.1 $Acm^{-2}\mu m^{-1}$. In recombination- related mechanisms, SRH recombination is still the primary mechanism, which is consistent with our previous results. This trend could be understood from Equation (2.1) that large amount of SRH recombination current diminishes the total collected current, thus deteriorating the performance of the solar cell.

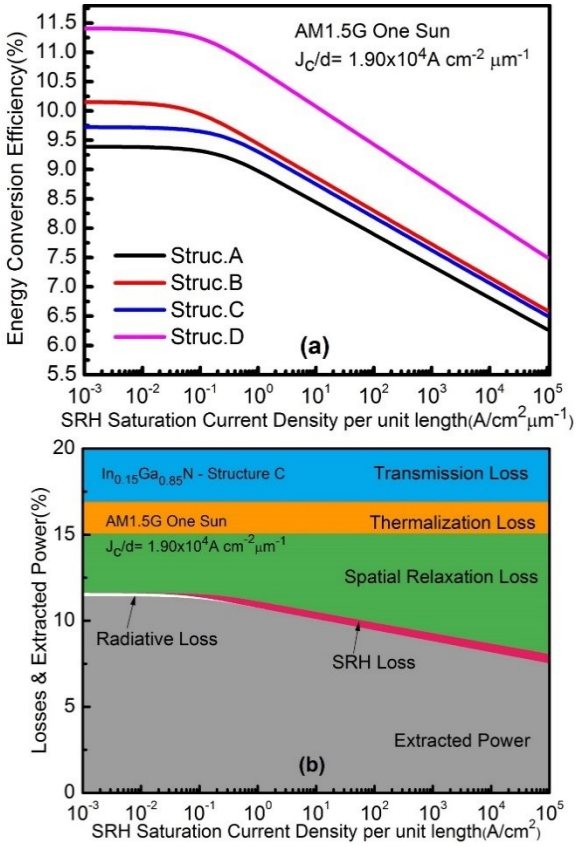

Figure. 2.5. (a) Energy conversion efficiency vs. SRH recombination current densities per unit length (J_A/d) for single junction $In_{0.15}Ga_{0.85}N$ solar cells in four structures; (b) losses and extracted power vs. SRH recombination current densities per unit length (J_A/d) for single junction $In_{0.15}Ga_{0.85}N$ solar cell under AM 1.5G one sun condition in structure C, at the optimal junction thickness, with typical Auger recombination current density per unit length $J_C/d = 1.9 \times 10^4\ Acm^{-2}\mu m^{-1}$.

By virtue of unique and favorable merits of InGaN materials, their application and operation for harsh environment like space exploration are desirable and growing solar concentration turns out to be a potent and practical approach to achieve high conversion efficiency. Figure 2.6(a) presents energy conversion efficiency vs. solar concentrations for single junction $In_{0.15}Ga_{0.85}N$ solar cells in four structures under AM 1.5G solar spectrum. The efficiencies of all four types of solar cell structures increase linearly with growing solar concentrations, where structure D has the highest efficiency. Note that in practical devices, the energy conversion efficiency will saturate due to the fact that the series resistance and other losses change with solar concentration, which are not considered in our model. Figure 2.6(b) presents the losses and efficiency maps vs. solar concentration for single junction $In_{0.15}Ga_{0.85}N$ solar cells in structure C, with typical $J_A/d = 1000\ Acm^{-2}\mu m^{-1}$and $J_C/d = 1.9 \times 10^4\ Acm^{-2}\mu m^{-1}$. The transmission loss still dominates over other loss mechanisms as a result of large bandgap of III-nitrides and there is minimum variation of transmission and thermalization losses with the specified structure. Moreover, spatial relaxation loss gradually drops as rising solar concentrations, which could be ascribed to the fact that the extractable energy of photogenerated carriers is enhanced with the solar concentration. It is noticeable that SRH recombination loss dominates over other recombination-related loss

mechanisms throughout the entire range of solar concentration. For GaAs solar cells, the radiative loss would take the lead after 500 suns. [66] This difference may be attributed to the large amount of subband transition induced from unavoidable defect states during the growth of InGaN materials.

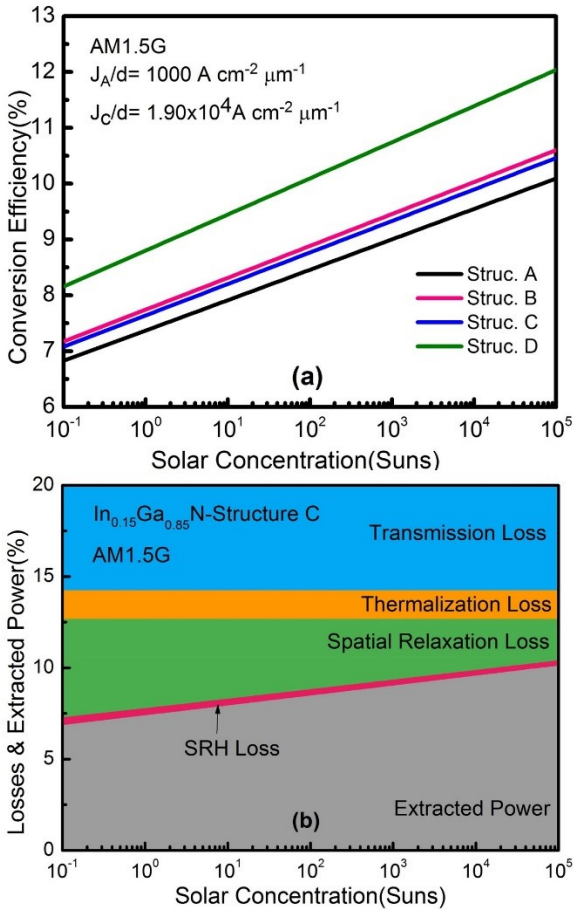

Figure. 2.6. (a) Energy conversion efficiency vs. solar concentration for single junction $In_{0.15}Ga_{0.85}N$ solar cells in four structures; (b) losses and extracted power vs. solar concentration for single junction $In_{0.15}Ga_{0.85}N$ solar cell under AM 1.5G one sun condition in structure C, at the optimal junction thickness, with typical SRH recombination current density per unit length $J_A/d = 1000\, Acm^{-2}\mu m^{-1}$ and Auger recombination current density per unit length $J_C/d = 1.9 \times 10^4\, Acm^{-2}\mu m^{-1}$.

2.3 Analysis of loss mechanisms in two junction solar cell

The large tunable direct bandgaps from InGaN material systems offer a unique and promising opportunity to design high-performance multi-junction (MJ) solar cells using a single ternary alloy system. In this section, we focus on the two-junction (2J) InGaN solar cells, which include two junctions in structure A. The loss analysis of 2J solar cell is based upon the typical material parameters and properties of InGaN. It is assumed in the model that the Urbach tail energy is 50meV, the effective absorptance of Aa =1, SRH recombination current density of $J_A/d = 1900\ Acm^{-2}\mu m^{-1}$ and Auger recombination current density $J_C/d = 3.8 \times 10^4\ Acm^{-2}\mu m^{-1}$, which are proper up-to-date values of InGaN materials. The equations of SRH recombination current densities (J_A) and Auger recombination current density (J_C/d) and the corresponding coefficients are based on Ref. 6. Figure 2.7 shows (a) bandgap energy and conversion efficiency vs. top-junction bandgap energy and (b) losses and extracted solar power vs. top-junction bandgap energy for 2J InGaN solar cells. The top junction bandgap window in Figs. 2.7(a) and 2.7(b) is very limited, which could be partly attributed to the perfect current matching condition assumed in the calculation. This was also found in the calculation of three- and four-junction InGaN solar cells (data not shown here), which could be a potential challenge for the design of MJ InGaN solar cells. With the top-junction bandgap varying from 1.68 eV to 1.82 eV, we can observe an efficiency of 43.5% under AM1.5G one sun radiation. The losses and efficiency map for 2J InGaN solar cells in Fig. 2.7(b) show that the transmission loss is no longer the major loss mechanism, while the spatial relaxation loss mainly accounts for the degradation of conversion efficiency, especially when the top junction bandgap exceeds 1.78 eV. These results indicate that 2- and multi-junction solar cells will reduce the transmission loss and

enhance the conversion efficiency compared to 1J structure. The drop of loss and extracted power at 1.78 eV may be attributed to the atmospheric features of AM 1.5G solar spectrum. Therefore, decreasing spatial relaxation loss will become a critical issue for the design of 2J InGaN solar cells. Meanwhile, SRH loss still dominates in the recombination-related losses, which is again due to the material quality of the InGaN active layers.

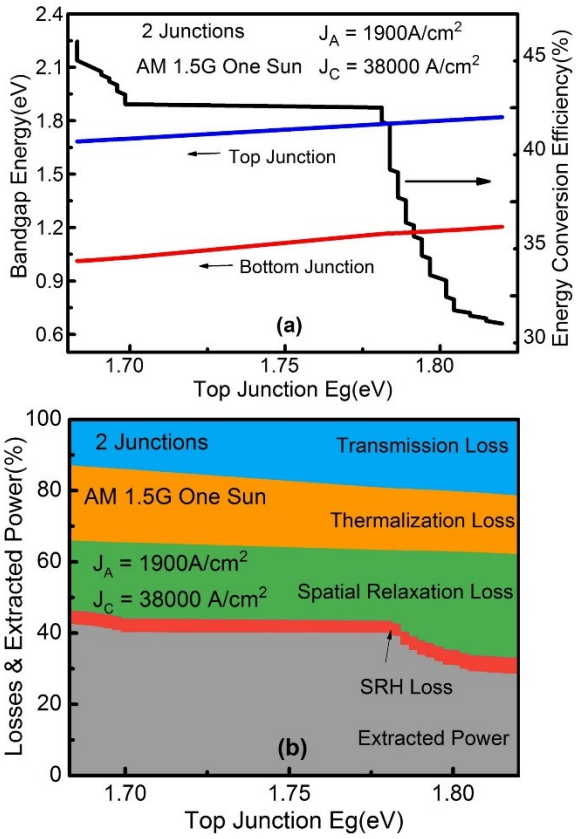

Figure. 2.7. (a) Bandgap energy and conversion efficiency vs. top-junction bandgap energy and (b) losses and extracted solar power vs. top-junction bandgap energy for 2J InGaN solar cells, with SRH recombination current density $J_A/d = 1900\ Acm^{-2}\mu m^{-1}$ and Auger recombination current density $J_C/d = 3.8 \times 10^4\ Acm^{-2}\mu m^{-1}$.

To further investigate the possible PV applications of InGaN materials system, the correlated bandgap energies and maximum energy conversion efficiency are plotted in Fig.

2.8(a) along with losses and extracted power in Fig. 2.8(b). Figure 2.8(a) presents that the optimal bandgap energies of top junction and bottom junction remain almost constant and decrease significantly at 200 suns concentrations, which could allow more photons to be absorbed. While in Figure. 2.8(b), both transmission loss and spatial relaxation loss reduce collectively and thermalization loss tends to rise, which could be ascribed to the decreasing optimal bandgap energy as growing solar concentrations. Aside from that, SRH loss still takes up the most part of the total recombination losses. Hence, rising solar concentration proves to be an efficient approach for high performance InGaN solar cells, which corresponds to our previous results of single junction InGaN solar cells.

To thoroughly investigate PV performance and loss mechanisms in InGaN solar cells, we apply a semi-analytical model to 1J and 2J solar cells. By considering photon recycling, spontaneous emission, non-radiative recombination losses, and non-step like absorptance and emittance, we explore four types of fundamental loss mechanisms with typical published material parameters. We determine that the width of Urbach energy has a significant effect on the emittance of surfaces, which is broad compared to other III-V materials and is not negligible in the whole solar spectrum. This below-bandgap tail boosts the light absorption, resulting in increasing the short-circuit current and reducing the open-circuit voltage.

Furthermore, we also investigate the roles of SRH recombination current densities per unit length and sun concentration for four structures. We identify that the transmission loss is the major cause responsible for loss and SRH loss is the dominant recombination loss mechanism under any solar concentration. As a result, both improving the material quality of InGaN active layers and rising solar concentration offer constructive ways to

enhance the performance of InGaN solar cells. With typical J_A/d and J_C/d values, the predicted energy conversion efficiency could be 7.6% for structure C. Moreover, conversion efficiency could be greatly enhanced by increasing solar concentration and the peak efficiency could be achieved as 9.0% under 1000 suns. As for 2J InGaN solar cells, the current matching issue would lead to the limited choice of top-junction bandgap while the efficiency as high as 43.5% is achieved with the top-junction bandgap from 1.68 eV to 1.82 eV. By analyzing the optical properties and loss mechanisms, these results provide fundamental insights and detailed guidance for the future designs and developments of InGaN solar cells.

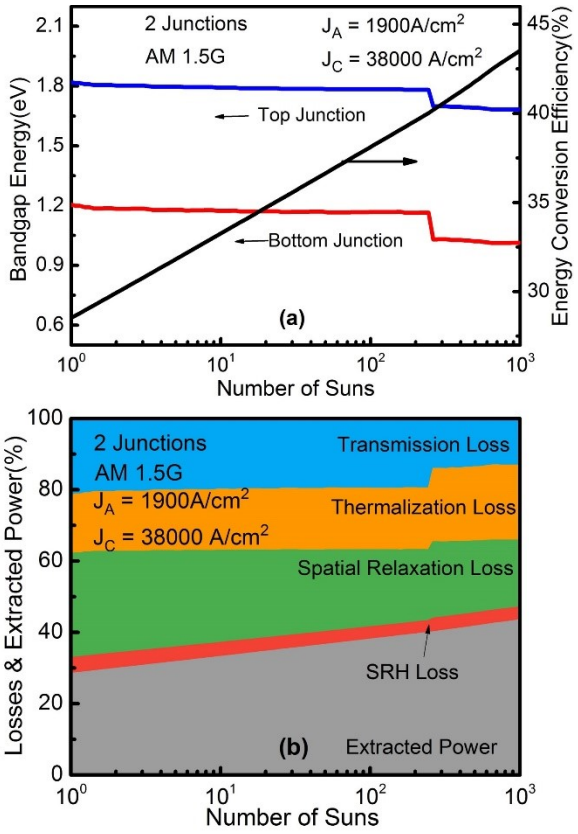

Fig. 2.8. (a) Bandgap energy and conversion efficiency vs. solar concentration and (b) losses and extracted solar power vs. solar concentration for 2J InGaN solar cells, with SRH

recombination current density $J_A/d = 1900\ Acm^{-2}\mu m^{-1}$ and Auger recombination current density $J_C/d = 3.8 \times 10^4\ Acm^{-2}\mu m^{-1}$.

CHAPTER 3

NONPOLAR AND SEMIPOLAR INGAN/GAN MULTIPLE-QUANTUM-WELL SOLAR CELLS WITH IMPROVED CARRIER COLLECTION EFFICIENCY

3.1 Motivations and research background

Recent years have seen an increasing interest in the development of III-nitride InGaN solar cells. This interest has been driven by the favorable physical properties of III-nitrides for photovoltaic (PV) applications such as strong absorption coefficients (on the order of 10^5 cm^{-1} near the band edge), tunable band gap from 0.70 eV to 3.4 eV, outstanding thermal performance, and superior radiation resistance under harsh environments[2]. The InGaN solar cell is therefore a promising candidate for future high-efficiency thin film PV applications, especially for the fabrication of top cells in ultra-high-efficiency multi-junction solar cells (e.g., > 50%), as well as for space and terrestrial concentrated PV applications. There have been many reports on the InGaN solar cells and their performance was steadily improved[3], [10], [12], [17], [18], [36], [86], [87]. The recent development of InGaN solar cells has further benefited from the comprehensive research efforts in other III-nitride optoelectronic devices[88]–[97] such as light-emitting diodes (LEDs)[88]–[91] and laser diodes (LDs)[88], [92]–[94], where InGaN/GaN multiple-quantum-well (MQW) structures are now being utilized for developing high-efficiency III-nitride solar cells[12], [15], [18], [24], [44], [86]. Despite the encouraging progress, the performance of current InGaN solar cells is still very low, especially compared with well-developed PV devices based on Si or III-V materials. Considerable materials and device challenges still need to be addressed before the full potential of InGaN solar cells can be realized.

3.2 Experimental details

InGaN/GaN MQW solar cells were grown by conventional metal-organic chemical vapor deposition (MOCVD) on nonpolar *m*-plane, semipolar $(20\bar{2}1)$ plane, and polar *c*-plane GaN substrates, respectively. All the samples have the same device structures where the MOCVD growth conditions were carefully adjusted to achieve In compositions of ~20% in the QWs. The device structure consists of 1 μm Si-doped n-GaN ([Si]=5×10^{18} cm^{-3}), 10 nm highly Si-doped n^+-GaN ([Si]=1×10^{19} cm^{-3}), 20 periods of InGaN (6 nm) / GaN (10 nm) MQWs, 30 nm Mg-doped smooth p^+-GaN ([Mg]=1×10^{19} cm^{-3}), 120 nm Mg-doped intentionally roughened p-GaN ([Mg]=3×10^{19} cm^{-3}), and 10 nm highly Mg-doped p^+-GaN contact layer ([Mg]=1×10^{20} cm^{-3}). The schematic device structure is shown in the inset of Fig. 1. Material characterizations such as high resolution x-ray diffraction (HRXRD) analysis and atomic force microscopy were performed (data not shown here), which revealed similar material properties for all the samples in terms of alloy composition and surface roughness. The transmission, reflectance and absorption spectra of the samples were measured using LAMBDA 950/1050 UV/VIS/NIR Spectrophotometer from Perkin Elmer. The samples were then fabricated into 1 mm × 1 mm mesas by standard contact lithography and inductively coupled plasma (ICP) etching. Ti/Al/Ni/Au n-type contacts were deposited around the perimeter of the mesa and Ni/Au p-type grid contacts with a center-to-center grid spacing of 200 μm were deposited via electron beam evaporation. The fabricated solar cell devices were characterized by illuminated J–V measurements with a Keithley 2420 source meter under an Oriel Class A Solar Simulator with AM1.5G and 1 sun condition. EQE measurement data was collected using a 150W Xenon arc lamp coupled with a Cornerstone 260 1/4m monochromator and calibrated with a reference Si

photodetector. Energy band diagrams were simulated using SiLENSe, developed by STR Group[98].

3.3 Results and discussions

Figure 3.1(a) presents the absorption spectra of InGaN/GaN MQW solar cell samples on nonpolar *m*-plane, semipolar $(20\bar{2}1)$ plane, and polar *c*-plane GaN substrates, respectively. The results show that the absorption cutoff wavelength of the devices redshifts with increasing polarizations inside the materials, i.e., *c*-plane > $(20\bar{2}1)$ plane > *m*-plane. This indicates a smaller effective bandgap in *c*-plane InGaN solar cells possibly due to a larger QW tilting caused by stronger polarization-related effects[99]. Figure 3.1(b) shows the Tauc's plots for all the samples. The effective bandgap energies (E_g) are 2.85 eV, 2.73 eV and 2.45 eV for *m*-plane, $(20\bar{2}1)$ plane and *c*-plane samples, respectively. Furthermore, it was also observed that the absorption edge tends to broaden with increasing polarization of the devices, which can be characterized by the Urbach tail energy (E_u). E_u is strongly related to the band structures[85], [100]. In this case, this broadening of absorption edge can be attributed to the different band structures, e.g., valence band states[7], due to different polarity of the GaN substrates. This trend is also in a good agreement with our previous theoretical analysis, which suggests that E_u can modify the effective bandgap energy, thus affecting the optical properties and device performance of the solar cells[60].

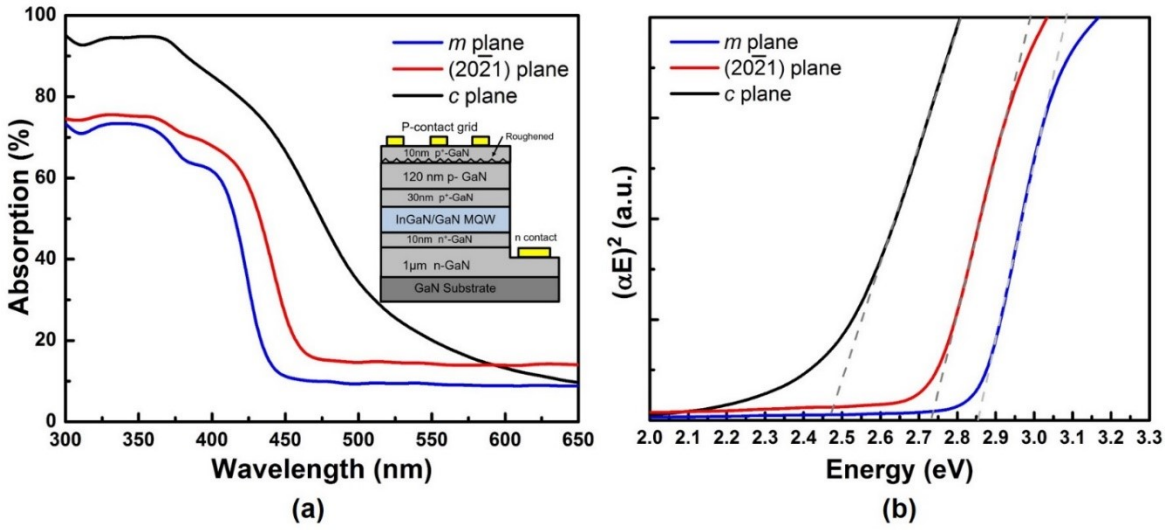

Figure. 3.1. (a) Room temperature transmission spectra and (b) Tauc's plots of *m*-plane, (20$\bar{2}$1) plane and *c*-plane InGaN MQW solar cells. The inset of Fig.1 shows the cross-section schematic structure of the MQW InGaN solar cells.

Figure 3.2 shows (a) illuminated J–V curves and (b) EQE spectra under zero bias and (c) IQE spectra for the fabricated nonpolar *m*-plane, semipolar (20$\bar{2}$1) plane, and polar *c*-plane InGaN/GaN MQW solar cells, respectively. Table I summaries the key device parameters including values of E_g from Tauc's plots, open circuit voltage (V_{oc}), bandgap-voltage offset (W_{oc}), short circuit current (J_{sc}), fill factor (FF), EQE, and IQE for all the devices. The IQE is defined as the ratio of EQE and absorption spectra: $IQE = EQE/absorption$, which is a fine gauge of carrier collection efficiency. The bandgap-voltage offset W_{oc} is defined as the difference between the effective bandgap and V_{oc}, which is an indicator of quasi-Fermi level splitting at the open circuit condition[101]. Nonpolar *m*-plane solar cell device showed the smallest W_{oc} value compared to other devices. Furthermore, it showed the best device performance, with a V_{oc} of 2.32 V, W_{oc} of 0.59 V, J_{sc} of 0.803 mA/cm^2, FF of 55.5%, and peak EQE of 39.4%. The performance of

m-plane InGaN solar cells is comparable to the previous reports of III-nitride solar cells, and further improvement can be expected with more advanced devices structures such as thicker absorption layers and better optical designs. Although polar c-plane solar cell initially showed the highest absorption in optical measurement [Fig. 3.1(a)], it showed lower EQE and IQE compared to nonpolar and semipolar $(20\bar{2}1)$ devices. This result is possibly due to the strongest polarization-related effects on polar *c*-plane devices, which resulted in a poor carrier transport and collection in the electric measurement. This is also evident from the low J_{sc} on the polar *c*-plane devices. The short circuit current J_{sc} can be approximated by the equation:

$$J_{sc} = \int_0^\infty qF(\lambda) \cdot EQE(\lambda) d\lambda = \int_0^\infty qF(\lambda) \cdot IQE(\lambda) \cdot absorption(\lambda) d\lambda, \qquad (3.1)$$

where $F(\lambda)$ is the photon flux of the given solar spectrum. It can be seen that J_{sc} is proportional to EQE, which is the product of IQE and absorption. Although the absorption spectra of *c*-plane solar cell is much higher than nonpolar and semipolar devices, the poor carrier collection efficiency, represented by IQE, leads to a very low J_{sc} and poor PV performance. Conversely, nonpolar *m*-plane and semipolar $(20\bar{2}1)$ solar cells showed higher EQE despite the lower absorption than polar *c*-plane device, which can be attributed to improved carrier collection efficiency from reduced polarization-related effect. This result suggests that the polarization-related effects will significantly impact the carrier collection efficiency and the PV performance of III-nitride InGaN solar cells.

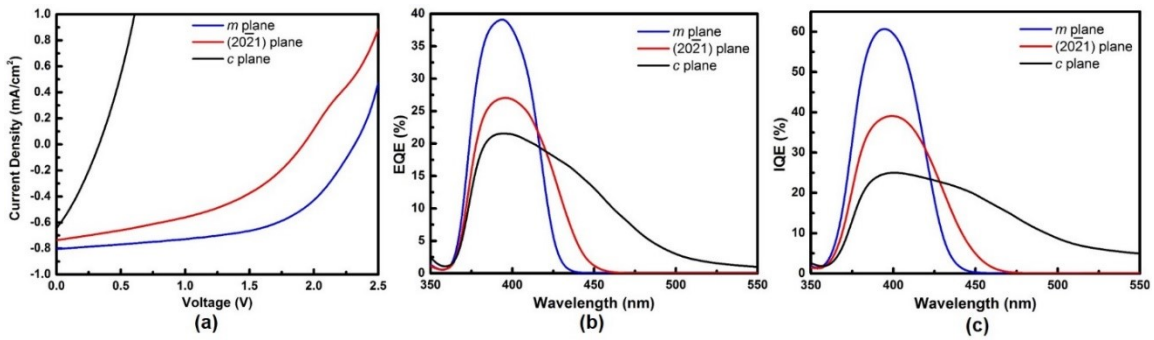

Figure. 3.2. (a) Illuminated J–V curves for *m*-plane, (20$\bar{2}$1) plane, *c*-plane and reference *c*-plane InGaN MQW solar cells. (b) EQE and (c) IQE curves for *m*-plane, (20$\bar{2}$1) plane, *c*-plane InGaN MQW solar cells.

Table 1 Summary of key device parameters for nonpolar *m*-plane, semipolar (20$\bar{2}$1) plane, and polar *c*-plane InGaN/GaN MQW solar cell devices.

	E_g(eV)	V_{oc}(V)	W_{oc}(V)	J_{sc}(mA/cm^2)	FF(%)	Peak EQE(%)	Peak IQE(%)
m-plane	2.85	2.32	0.53	0.803	55.5	39.4	61.4
(20$\bar{2}$1)	2.73	1.92	0.81	0.736	43.2	27.1	39.6
c-plane	2.45	0.33	-	0.644	29.9	21.5	25.2

To further investigate the effect of polarization field on carrier transport on InGaN MQW solar cells, the EQEs of nonpolar *m*-plane, and semipolar (20$\bar{2}$1) plane, and polar *c*-plane MQW solar cells were measured under different negative bias and the results were presented in Fig. 3.3(a)–3.3(c). In order to better quantify the difference of EQEs under different bias, relative EQE was plotted where the EQE spectra from zero bias to −4V reverse bias was normalized using the peak EQE value under zero condition. For polar *c*-plane solar cell, the ratio of peak EQE under −4V reverse bias and zero bias is as large as ~7. While the ratios are only ~1.60 and ~1.23 for semipolar (20$\bar{2}$1) plane device and nonpolar *m*-plane, respectively. The high ratio of EQEs under negative/zero bias on polar

c-plane solar cells is consistent with previous report and was attributed to the large polarization-related effects.[21] The large polarization field on polar *c*-plane structures creates higher barrier between the QWs, thus affecting carrier tunneling and transporting, which will lead to reduced carrier collection efficiency of the solar cells under zero bias. The applied negative bias will screen and partially offset the polarization-induced electric field, and enhance the carrier transport and collection in the QWs, leading to an increased EQE for the solar cells under negative bias. On the other hand, the small difference of EQEs under zero/negative bias on nonpolar and semipolar $(20\bar{2}1)$ solar cells clearly indicates the much smaller polarization-related effects in these devices and is consistent with previous EQE results. In addition, it can be also observed that for polar *c*-plane solar cell, the absorption edge, or the cutoff wavelength of EQE spectra increases when the applied negative bias increase, indicating a strong change in the QW energy band profile due to the previously mentioned screening effects on the polarization-induced electric field. In contrast, only negligible change was observed in the absorption edge of nonpolar *m*-plane device.

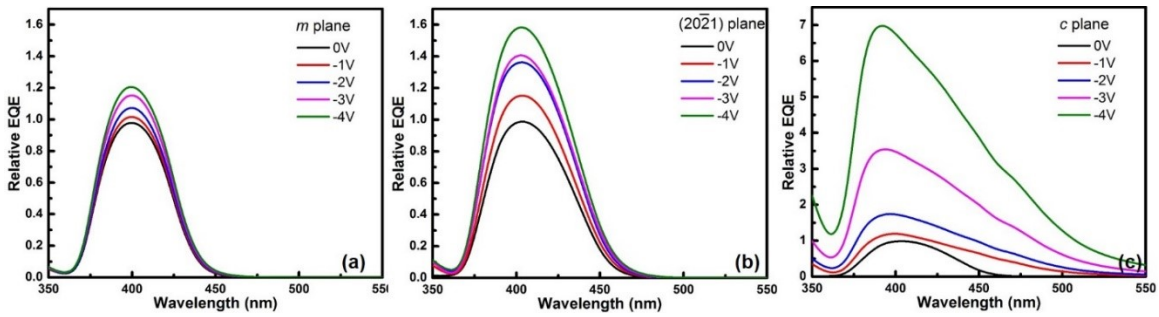

Figure. 3.3. EQE spectra under different reverse bias conditions of *m*-plane, $(20\bar{2}1)$ plane, *c*-plane InGaN MQW solar cells. Relative EQE was plotted where EQE spectra from zero bias to −4V reverse bias was normalized using the peak EQE value under zero condition.

To further illustrate the difference of polarizations-related effects on nonpolar *m*-plane, and semipolar $(20\bar{2}1)$ plane, and polar *c*-plane devices, simulations for InGaN/GaN MQW structures were carried out using the commercial package developed by the STR Group[98]. The potential distributions were calculated by solving the Schrodinger-Poisson equations self-consistently and include strain and polarization effects. The details of the methods can be found in Ref. 32. Figure 3.4 demonstrates the simulated energy band diagrams for $In_{0.20}Ga_{0.80}N$/GaN MQW solar cell with 6 nm InGaN QW and 10 nm GaN barrier on (a) nonpolar *m*-plane, (b) semipolar $(20\bar{2}1)$ plane, and (c) polar *c*-plane. Figure 12(d) shows the comparison zoom-in results of a single QW in three structures. For MQWs with 10 nm GaN barriers, tunneling is the dominant carrier transport mechanism in room temperature[34], [102]. Based on Wentzel-Kramers-Bruillouin (WKB) approximations, the tunneling lifetime of an electron in a QW is primarily determined by the barrier width and barrier height and is given by the following equation[102]:

$$\frac{1}{\tau_T} = \frac{n\pi\hbar}{2m^* L_w^2} \exp\left(\int_0^{L_b} -2\sqrt{\frac{2m^*(E_c(x) - E_n)}{\hbar^2}}\, dx \right) \tag{3.2}$$

where τ_T is the tunneling lifetime, m^* is the effective masses, $L_w$is the well thickness, $L_b$is the barrier thickness. To better quantify the effective barrier height for tunneling, H_e is defined as $H_e = E_c - E_n$, where E_c is the average values of conduction band minimum of the barrier on the left of the QW and E_n is the *n*th subband energy of the electron. We take the electron ground state $E_1(n = 1)$ in one QW. Using this method, we calculated H_e for electrons tunneling from the QW for three structures, which are 0.611 eV, 0.455 eV and 0.410 eV for polar *c*-plane, semipolar $(20\bar{2}1)$ plane, and nonpolar *m*-plane, respectively, as illustrated in Fig. 12(d). As the effective barrier height H_e decreases, the tunneling rate

increases, leading to better transport and higher collection of photogenerated carriers. The simulation results are consistent with the experiment results where nonpolar *m*-plane solar cells with lowest H_e and polarization-related effects showed the highest collection efficiency and EQE compared to semipolar $(20\bar{2}1)$ plane and polar *c*-plane devices. Polarizations in III-nitride materials will therefore have significant impact on InGaN solar cell performance.

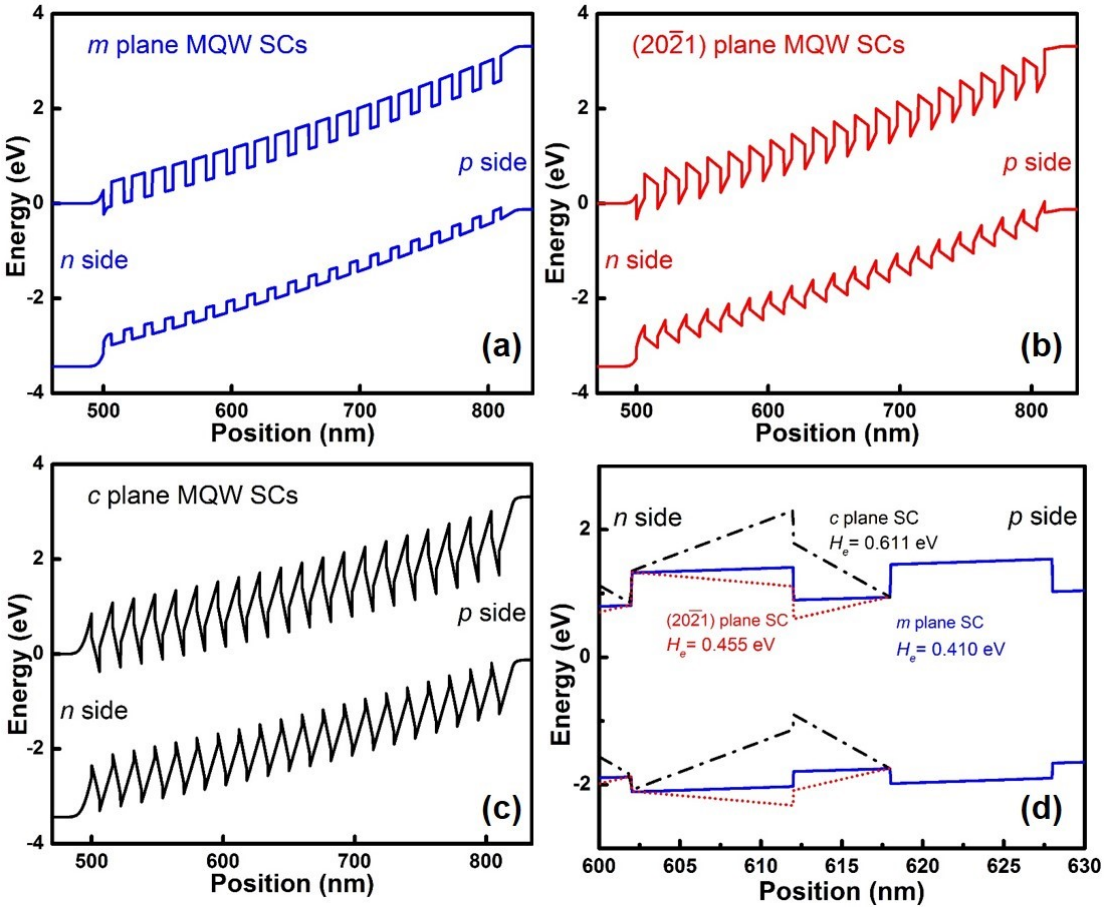

Figure. 3.4. Schematic energy band diagrams for an $In_{0.20}Ga_{0.80}N$ MQW solar cell with 20 periods of InGaN (6nm)/GaN (10nm) MQWs on (a) non-polar *m*-plane, (b) semipolar $(20\bar{2}1)$ plane, and (c) polar *c*-plane. (d) shows the comparison zoom-in results of a single QW in three structures and effective barrier height values.

3.4 Short summary

In conclusion, we demonstrate the first nonpolar and semipolar InGaN/GaN MQW solar cells based on nonpolar *m*-plane and semipolar $(20\bar{2}1)$ plane bulk GaN substrates, and their PV performance are systematically compared. Nonpolar *m*-plane InGaN/GaN MQW solar cell exhibits the best PV performance across all devices, which is attributed to the improved collection efficiency from the reduced polarization-related effect. The result is further confirmed by bias-dependent EQE measurements and energy band diagram simulations. Our results show the great potential of nonpolar and semipolar devices for future's high-efficiency III-nitride solar cells.

CHAPTER 4

GROWTH & CHARACTERIZATIONS OF C-PLANE SINGLE-JUNCTION INGAN/GAN MULTIPLE-QUANTUM-WELL SOLAR CELLS

4.1 Experimental details

We design 7 QW structures for InGaN solar cell samples. The detailed structural parameters are included in Figure 1 (a). These parameters were obtained from comparing the measured data and the simulation in HRXRD measurement using PANalytical X'Pert Pro materials research X–ray diffractometer (MRD) system with Cu Kα radiations, which were in good agreement with the design. Full structures of the InGaN/GaN MQW solar cells were as same as the last report.

a

Sample #	In%	QW periods	Well (InGaN) thickness	Barrier (GaN) thickness
431	16	15	3	6.6
432	16	30	3	6.7
433	15	15	3	8
435	11	30	3	7.1
436	11	30	3	5.1
437	14	30	3	7.7
438	14	30	3	5.5

b

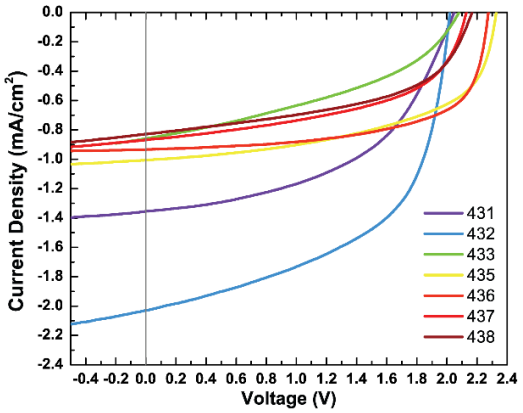

Figure. 4.1 (a) the detailed structural parameters of seven samples and (b) The representative illuminated JV measurements of the InGaN MQW solar cell for samples from 431 to 438 at room temperature.

Figure 4.1(b) presents the illuminated J–V results at RT of 7 samples. Among all, we can note that sample 431 and 432 delivered better performance, especially in terms of Jsc. This is due to relatively higher In composition (16%) and moderate barrier thickness (~6.7 nm). However, values of Voc in these 2 samples are 2.02 V and 2.05V, respectively,

which are slightly lower than the rest. This can be ascribed to the same reason (relatively higher In). In addition, high Voc were observed in sample 435 and 437, which were 2.32V and 2.27V. This is owing to better structural integrity from thick GaN barrier (>7nm). The Jsc values of other samples (433 to 438) were limited in the range of 0.8-1.0 mA/cm2. The possible reason for the poor FF observed in sample 433 are currently being researched and no HT PV measurements was performed on this sample.

4.2 Results and discussions

To investigate the HT PV performance of these samples, we first performed temperature-dependent EQE spectral of the InGaN MQW solar cell for samples from 431 to 438 at different temperatures from 25°C (RT) to 450°C at a step of 50°C. These measurements were performed using a Linkam HFS600-PB4 stage with the capability of heating samples up to 600 °C. This stage is a small silver block with embedded resistive heater and thermocouple. This model has been used by others to carry- out similar measurements on GaAs and AlGaInP solar cells, and in those scenarios has demonstrated high accuracy and precision.

First of all we can observe the redshift of the cutoff wavelength in all temperature-dependent EQE spectra as temperature elevates. This corresponded to the decreasing bandgap energy of the InGaN absorbing layers with increasing temperature. In addition, the blue response at wavelengths shorter than ~360 nm (at 25 °C) also drops significantly. This is attributed to the parasitic losses in p-GaN layers resulting from the short minority carrier lifetimes. This provides an optimization challenge of p-GaN thickness for voltage and carrier transport (thicker) versus decreased parasitic absorption (thinner).

Through comparing the EQE in sample 431 and 432 in Fig.4.2 (a, b), we can conclude that fewer periods of InGaN QWs accounts for the incomplete absorption of incident light as observed in Fig.4.2 (a). It's exciting to note that sample 432 delivers the best EQE performance among all, with 78% peak EQE at RT and >70% at 450°C. Sample 435 [Fig.4.2(c)] and 436 [Fig.4.2(c)] also exhibited very stable EQE performance under all temperatures.

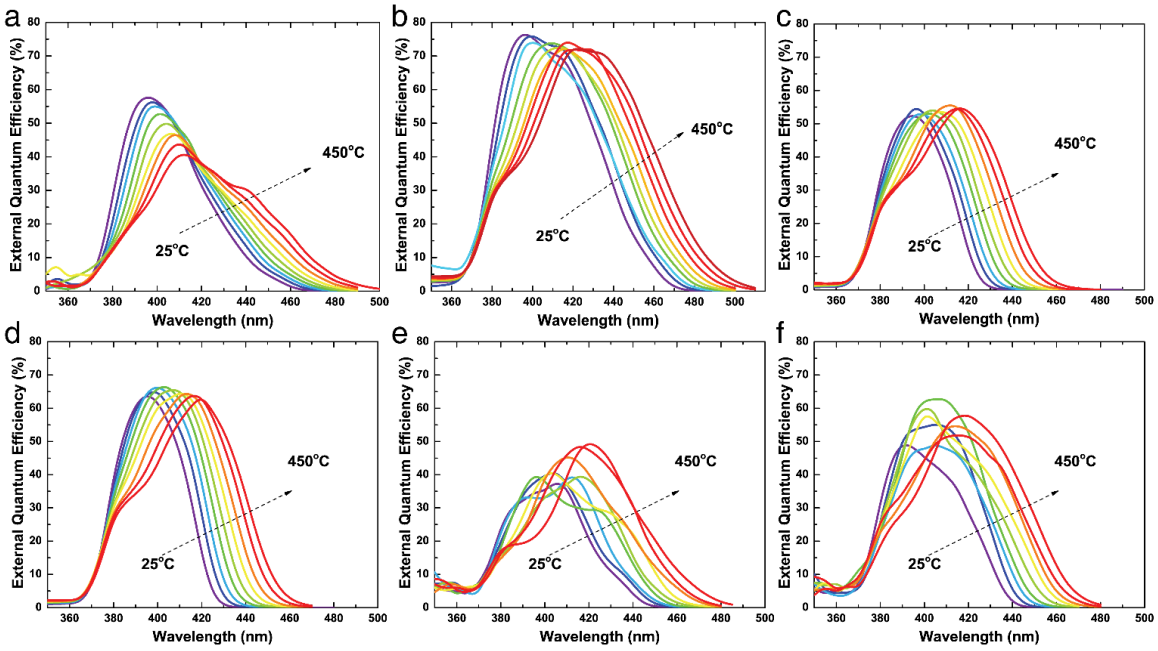

Figure. 4.2 (a-f) Temperature-dependent EQE spectral of the InGaN MQW solar cell for sample 431 (a), 432(b), 435 (c), 436 (d), 437 (e) and 438 (f) at different temperatures from 25°C to 450°C at a step of 50°C.

Figure 4.3(a) presents the temperature-dependent illuminated JV measurements of the InGaN MQW solar cell for sample 431 (a), 432 (b), 435 (c), 436 (d), 437 (e) and 438 (f) at different temperatures from 25°C to 450°C. The extracted V_{OC}, J_{SC}, FF and efficiency values as functions of temperatures are shown and compared in Fig.4 (a-f). In general, we can observe that V_{oc} values of all samples decrease with increasing temperature. However,

this decreasing rate is faster than the effects of band gap narrowing and increased dark current density (J_0) from thermally excited intrinsic carriers. This can be attributed to the thermal activation of the defects states in materials, considering all InGaN solar cell samples were grown on sapphires. In addition, J_{sc} values of all samples increase as temperature elevates, which is due to the enhanced thermal escape of carriers in the quantum wells. Moreover, it's also interesting to note that the FF values of all samples (except 432) peak between 200°C and 300°C. This effect can be attributed to the competing mechanisms between the enhanced thermal escape of carriers and recombination under elevated temperatures. This roll-over effect in FF under temperature-dependent measurements was also reported in other solar cells using double-heterojunctions like CdTe. Nevertheless, sample 432 exhibited the best PV performance among all and its efficiency is > 2.0% at RT. This suggests the optimal design of the InGaN QW in sample 432. Therefore, these results provide guidance and insights into the future design on InGaN-based solar cells. The PV parameters of all six samples under at 25°C, 250°C and 450°C is also tabulated below for clarity.

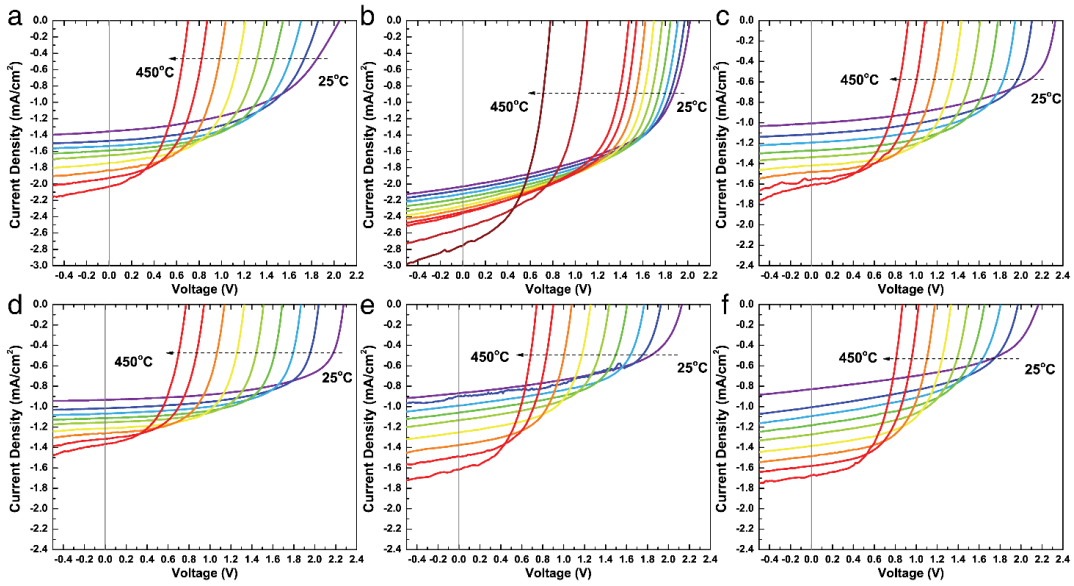

Figure. 4.3 (a-f) Temperature-dependent illuminated JV measurements of the InGaN MQW solar cell for sample 431 (a), 432 (b), 435 (c), 436 (d), 437 (e) and 438 (f) at different temperatures from 25°C to 450°C. Note that the ranges of y axis of sample 431 (a) and 432 (b) are larger than the rest.

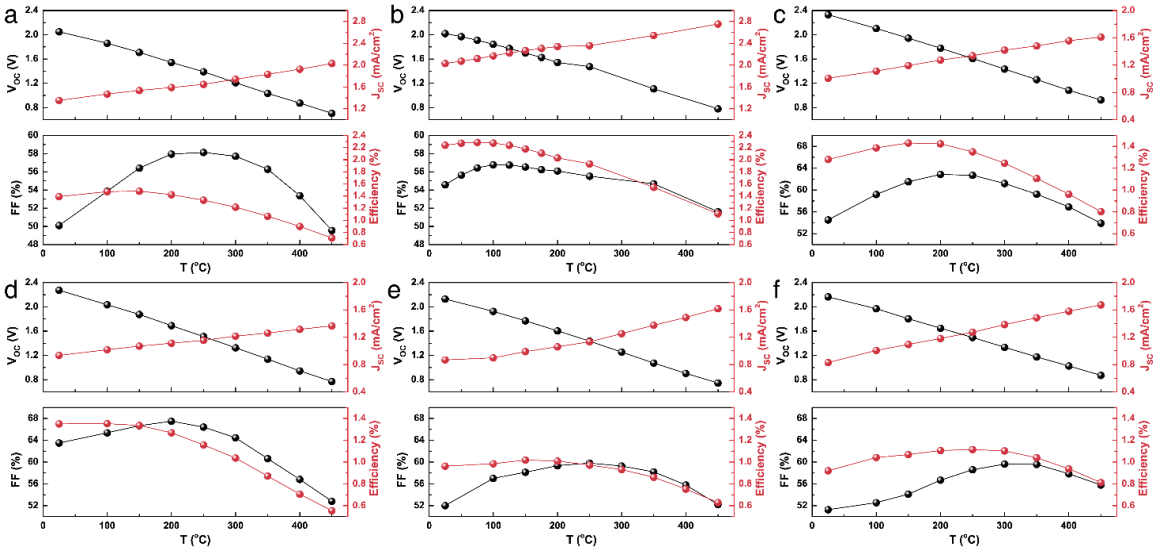

Figure. 4.4 (a-f) Extracted V_{OC}, J_{SC}, FF and efficiency values as functions of temperatures from Fig.4.3 (a-f) for 431 (a), 432(b), 435 (c), 436 (d), 437 (e) and 438 (f).

Table 2 Performance metrics for six InGaN MQW solar cell sample at 25°C, 250°C and 450°C.

4.3 Summary

We first design the structures for InGaN solar cell samples with different QWs, including different Indium composition, periods of QWs and barrier thickness. Structures of all seven InGaN solar cell samples were then characterized and calibrated by HRXRD measurement using PANalytical X'Pert Pro materials research X–ray diffractometer (MRD) system with Cu Kα radiations. The measured data were fitted to determine the critical structural parameters, such as well and barrier thickness, indium composition and layer thickness of p-GaN et al. These measurements were all performed at room temperature (RT). The PL measurement was further performed to confirm the indium composition.

CHAPTER 5

ENERGY BAND ENGINEERING OF INGAN/GAN MULTI-QUANTUM-WELL SOLAR CELLS VIA ALGAN ELECTRON- AND HOLE-BLOCKING LAYERS

5.1 Motivations and research background

III–nitride (III–N) materials have seen huge success in both electronics[103]–[108] and optoelectronics[109]–[112], [88], [91], [113]–[116], including power diodes[103]–[108], solid-state lighting[109]–[112], [88], [91], and integrated photonics[113]–[116]. Ternary InGaN alloys, in particular, have emerged in recent years as promising candidates for photovoltaic (PV) applications[117], [4], [5], [60], [44], [49], especially for high temperature PV applications, terrestrial photovoltaic thermal (PVT) hybrid solar collector systems, space applications and top cells in multi-junction (MJ) solar cells. III-N materials suitability for these device applications arises from their unique intrinsic properties, such as tunable wide bandgaps, a high absorption coefficient, high thermal stability and outstanding radiation resistance [2], [118]. To date, rapid progress has been made in the development of InGaN solar cells, with major emphasis placed on improving material quality and avoiding polarization-related effects. As a result, various approaches have been reported that focus on the growth of InGaN absorbing layers and the consequent device performance[18], [19], [35], [61], [86], [119], [120]. These include the use of strained InGaN/GaN quantum wells[18], [19], the optimization of structural parameters[35], [86], the use of native GaN substrates[61], [119], growth on different GaN crystal orientations[61], [120], *etc*. These methods reveal the relation between material quality, structural integrity and the corresponding PV properties of InGaN layers. For example, the employment of free-standing GaN substrates can substantially boost power conversion

efficiency (PCE) of InGaN solar cells by reducing their dislocation densities[19], [86], [119]. Additionally, the polarization doping[21] and the adoption of nonpolar and semipolar GaN substrates[61] are also able to mitigate polarization-induced issues and facilitate carrier transport.

Nevertheless, compared to traditional III-V materials, research on InGaN solar cells is still in its early stages and their PV performance is still far from satisfactory. The research efforts in developing high efficiency InGaN solar cells have been mainly focused on improving the material crystal quality, optimizing the optical designs, and controlling of the polarization effects. On the other hand, the engineering of energy bands of solar cells using, higher bandgap layers to act as window layers (or back surface fields), have been demonstrated as an effective approach to improve the carrier collection efficiency of solar cells. Such approach has already been successfully implemented in Si heterojunction with intrinsic thin-layer (HIT) solar cells[121], III-V solar cells[122]–[124] and II-VI solar cells like CdTe[125] and chalcogenides[126]. However, tailoring electronic energy band profiles with higher bandgap layers has not yet been thoroughly investigated in InGaN solar cells.

In this work, we demonstrate InGaN multi-quantum-well (MQW) solar cell structures with AlGaN layers as electron- and hole-blocking layers. This energy band design leads to substantially increased carrier lifetimes in InGaN MQW solar cells and improved carrier collection dynamics. The illuminated current-density (*J–V*) and external quantum efficiency (EQE) characterizations showed significant improvements for the solar cells with AlGaN layers compared to those without, mainly due to the huge enhancement in the short-circuit current density (J_{sc}). Under high temperatures up to 450°C, those cells

with the optimized AlGaN layers also surpassed the PV performance of the reference ones in terms of all key parameters. The detailed discussions are as follows.

5.2 Experimental details

The InGaN MQW solar cell structures were grown by conventional metal-organic chemical vapor deposition (MOCVD) on (0001) sapphires. The indium compositions in the MQWs were determined to be 15% by high resolution X-ray diffraction (HRXRD) and were further verified by photoluminescence (PL). The reference device structure consists of 2 μm Si-doped n-GaN ([Si]=3×10^{18} cm^{-3}), 125 nm highly Si-doped n^+-GaN ([Si]=2×10^{19} cm^{-3}), 30 periods of InGaN (3 nm)/GaN (7 nm) MQWs, 110 nm Mg-doped p-GaN, and a 10 nm highly Mg-doped p^+-GaN contact layer. In addition, five InGaN MQW solar cells (namely 1A, 1B, 1C, 2A, and 2B) with different AlGaN layers were also grown and the details of their structures are summarized in Table I. All structures have the same InGaN MQW active regions. Samples 1A and 1B have p-$Al_{0.15}Ga_{0.85}N$ layers of 5 nm and 10 nm, respectively, and no n- $Al_{0.15}Ga_{0.85}N$ layers. Sample 1C has 5 nm of both p- and n-$Al_{0.15}Ga_{0.85}N$ layers. Samples 2A and 2B have the same p-$Al_{0.15}Ga_{0.85}N$ layers as the Sample 1A but with different p-GaN layer thickness (50 nm for 2A and 150 nm for 2B).

Table. 3. Summary of five structure designs of InGaN/GaN MQW solar cells, including the reference structure.

Sample No.	p-GaN (nm)	p-$Al_{0.15}$GaN (nm)	n- $Al_{0.15}$GaN (nm)	MQW
Ref.	100	0	0	30 periods $In_{0.15}Ga_{0.85}N$ (3nm)/GaN (7nm) MQW
1A	100	5	0	
1B	100	10	0	
1C	100	5	5	
2A	50	5	0	
2B	150	5	0	

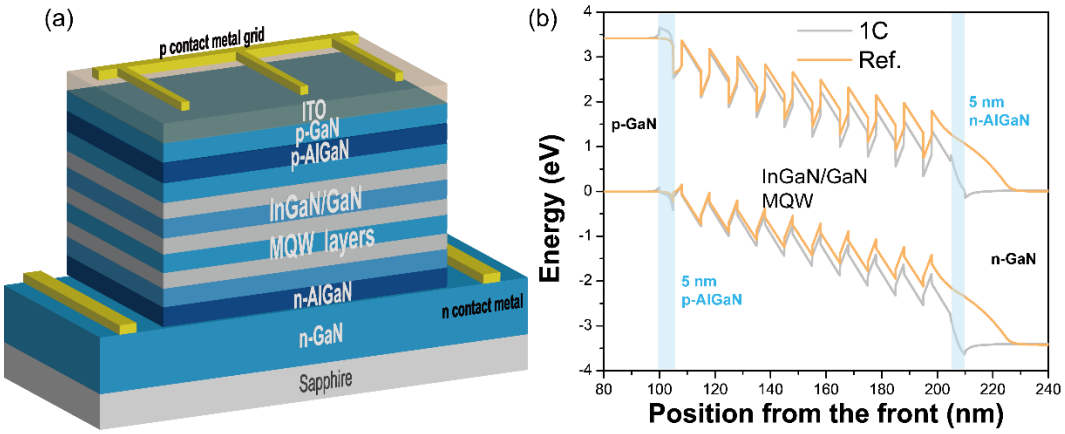

Figure. 5.1 (a) The schematic device structure of the sample 1C and (b) The comparison of band diagrams between the reference sample and 1C.

After the MOCVD growth, the crystal qualities of the InGaN MQW solar cell samples were characterized by HRXRD measurement using PANalytical X'Pert Pro materials research X–ray diffractometer system with Cu Kα radiations. The transmission and reflectance spectra of unprocessed wafers were characterized with LAMBDA 950/1050 UV/VIS/NIR Spectrophotometer from Perkin Elmer. The PL and time-resolved PL (TRPL) measurements at room temperature (RT) were performed using a homemade micro-PL system equipped with an incident 405 nm laser and a HORIBA spectrometer with a liquid nitrogen cooled CCD detector. After material and optical characterizations, these InGaN epi-structures were then processed into solar cell devices with 1 mm × 1 mm mesas using standard contact lithography and inductively coupled plasma (ICP) etching. 130 nm indium-tin-oxide (ITO) layers were deposited by dc-sputtering on top of the mesa as a current spreading layer with post-annealing in N_2/O_2 at 500 °C. Ti/Al/Ni/Au ring contacts and Ti/Pt/Au grid contacts were deposited around the perimeter and on the top of the mesa, respectively. Both metal contacts were deposited via electron beam evaporation.

The schematic device structure of the fabricated InGaN MQW solar cells of sample 1C is shown in Fig. 5.1(a). Illuminated *J–V* measurements were taken using an Oriel Class A Solar Simulator at 1 sun condition under AM1.5G spectrum. The EQE measurement data were collected using an Oriel QEPVSI quantum efficiency measurement system and calibrated with a reference Si photodetector. A Linkam HFS600-PB4 stage with the capability of heating samples up to 600 °C was used to perform the temperature-dependent measurements. More details on characterizations, fabrications and PV measurements can be found in the reference [61], [62].

5.3 Results and discussions

Figure 5.1(b) shows the comparison of energy band structures in equilibrium between the reference structure and 1C. The energy band diagrams of InGaN MQW solar cells were simulated using TCAD Silvaco software. The detailed values of the confined ground states, band edges (at 100nm) and the band offsets for electrons and holes with and without p-AlGaN layer in the first and last quantum well are presented in the supplementary material (See Table S1 and S2). The employment of the p-$Al_{0.15}Ga_{0.85}N$ layer introduces a 0.297 eV increase in the conduction band offset while maintaining the same barrier height in valence band. This enables more efficient extraction of holes to the p-GaN by blocking the overflowing electrons and reducing the recombination of electrons and holes in the p side. Likewise, the n-$Al_{0.15}Ga_{0.85}N$ layer lowers the conduction band offset by 0.634 eV and increases the valence band offset by 0.866 eV, enhancing electron transport to the n side. Therefore both p- and n- $Al_{0.15}Ga_{0.85}N$ layers improve carrier collection and reduce the surface recombination near the contacts.

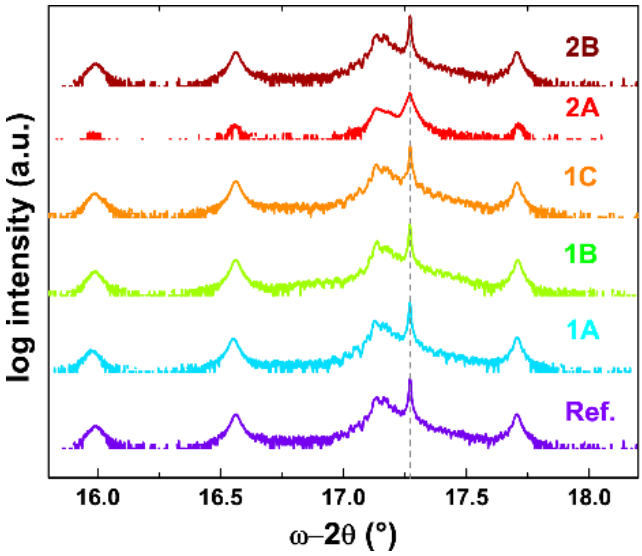

Figure. 5.2. The typical results of HRXRD ω-2θ scans taken across (002) reflection for sample ref., 1A, 1B, 1C, 2A and 2B, respectively.

The growth and doping issues of AlGaN layers are very complicated and will negatively impact the performance of InGaN MQW solar cells if the crystal quality is low. Therefore, before the device characterization, we performed HRXRD ω-2θ scans across (0002) reflection for all the InGaN solar cell samples to analyze the material quality and the results are shown in Fig. 5.2. The vertical dotted line indicates the main peak for GaN. The InGaN MQW peaks from the zeroth to the second order are well-distinguished and are located at nearly the same position. The indium compositions for all samples deduced from HRXRD results are ~ 15%. Overall, these results illustrate that all samples possess highly similar MQW structures without any negative effects caused by the addition of AlGaN layers. Additionally, the less obvious satellite peaks were found on sample 2A as shown in the XRD results. This is related to the less smooth interface between quantum wells and barriers, which leads to the slightly lower material quality in sample 2A[127]. Further investigations are being carried out to confirm this issue.

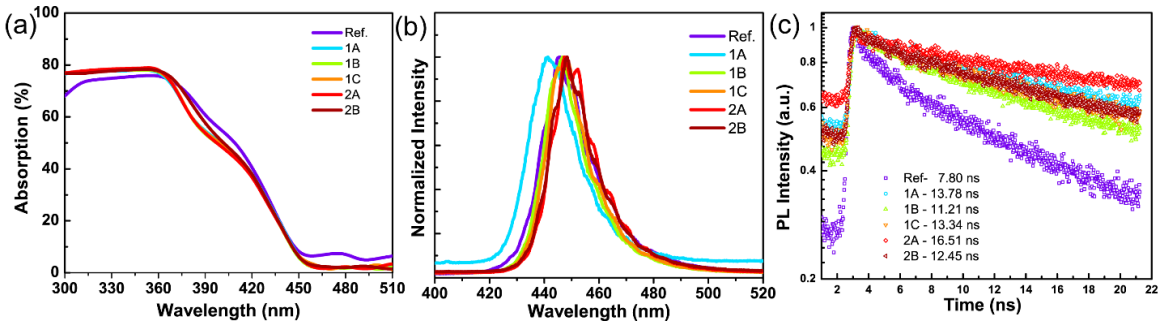

Figure. 5.3. (a) The light absorption spectra, (b) the room-temperature photoluminescence (PL) spectra and (c) room-temperature time-resolved photoluminescence (TRPL) results for sample ref., 1A, 1B, 1C, 2A and 2B, respectively.

Figure 5.3 shows (a) the light absorption spectra, (b) the RT PL spectra and (b) the RT TRPL results for all the InGaN MQW solar cell samples. The absorption spectra were determined from *Absorption (λ) = 100% − Transmission (λ) − Reflection (λ)*. The bandgap energies obtained from the absorption spectra and Tauc's plot (not shown here) were ~2.75 eV for all the 6 structures. This indicates an indium composition around 15%, which is in good agreement with the HRXRD results. Moreover, the emission peaks in PL measurements shown in Fig. 5.3 (b) are in the range of 445–450 nm, which also correspond to both the HRXRD and absorption results. The normalized TRPL results at RT are presented in Fig. 3(c) and the carrier lifetimes fitted from exponential decay functions are also shown. The lifetime in the reference structure is only ~7.8 ns while it's in the range from 11 to 16 ns for the other samples with AlGaN layers. A longer carrier lifetime indicates a higher possibility for photogenerated carriers to be collected at contacts[39], [46]. Compared to the reference structure, those with AlGaN layers all exhibited significantly improved carrier lifetimes (> 40%). This is due to the increased band bending in the quantum wells and thus reduced carrier recombination[128]. By comparing structure

1A and 1B we can see that the thin p-AlGaN layer (5 nm) is preferred in solar cell design. This can be explained by fewer defects and/or dislocations being generated during the growth process. Additionally, a moderate thickness of p-GaN layer (100 nm) leads to the longest lifetime among structures 1A, 2A and 2B. This can be related to the tradeoff between the highly resistive nature of the p-GaN layer and material quality.

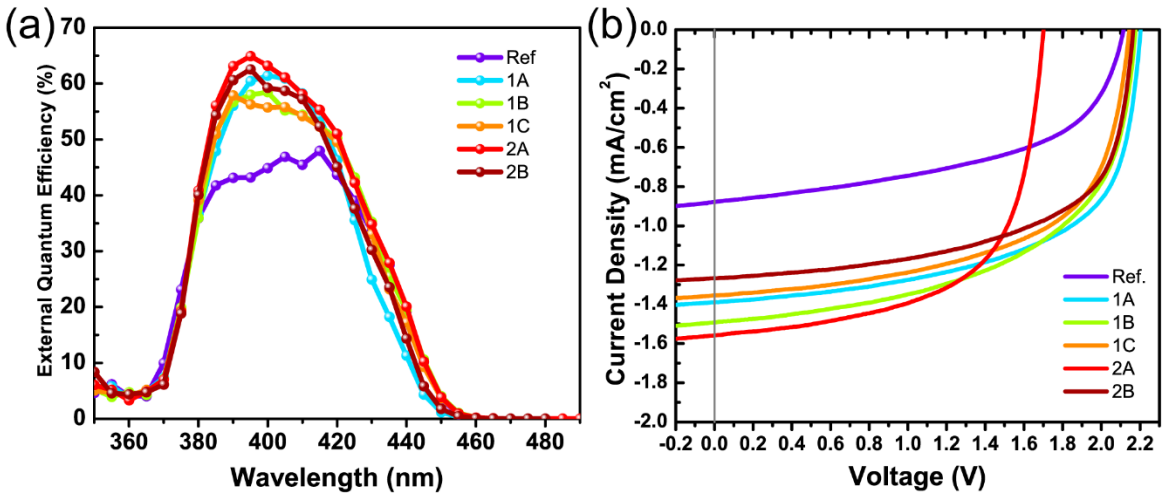

Figure. 5.4. (a) The representative EQE spectra and (b) the representative illuminated current density–voltage (*J–V*) measurements for sample ref., 1A, 1B, 1C, 2A and 2B, respectively.

Figure 5.4 presents (a) the representative EQE spectra and (b) the illuminated *J–V* measurements for the samples. The cutoff edges of the EQE for all samples are almost the same at 450 nm, which is in good agreement with the absorption and PL results. Samples 1A to 2B all exhibited better EQE performance than the reference structure. The peak EQE for the reference sample is only ~47% while it exceeded 60% for the other structures. The highest peak EQE of 65% was found in structure 2A. The large difference observed in EQE and IQE (See Fig.S1) between the reference and other structures demonstrates that band engineering with AlGaN layers in InGaN MQW solar cells significantly enhanced the

carrier collection efficiency, leading to better solar cell performance. Furthermore, for *J–V* curves all InGaN solar cell structures with AlGaN layers (1A to 2B) exhibited markedly improved J_{sc} as expected. In contrast, all structures exhibited essentially the same open-circuit voltage (V_{oc}) values except 2A. More details on the comparison of *J–V* performance are discussed in the following section.

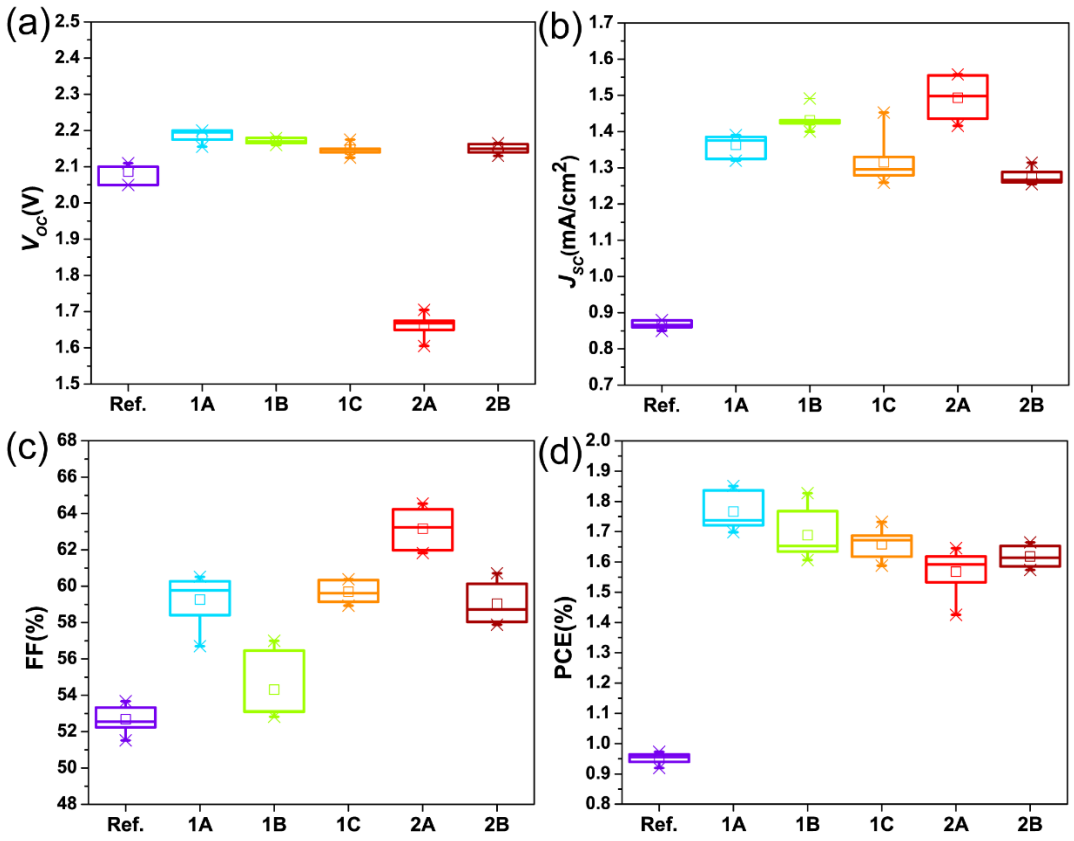

Figure. 5.5. The extracted values of (a) open-circuit voltage (V_{oc}), (b) short-circuit current (J_{sc}), (c) fill factor (FF), and (d) power conversion efficiency (PCE) from *J–V* curves for sample ref., 1A, 1B, 1C, 2A and 2B, respectively.

Figure 5.5 shows the extracted values of key PV performance parameters of (a) V_{oc}, (b) J_{sc}, (c) fill factor (FF) and (d) PCE from *J–V* curves in the form of a box chart for the reference sample (ref.), and samples 1A, 1B, 1C, 2A and 2B. These values are also included

in Table I. The measurements were performed on ~ 10 devices for each structure and ~ 60 devices in total. The V_{oc} of ref. (2.09 V) is slightly smaller than those of 1A, 1B, 1C and 2B. This is attributed to increased quasi-Fermi splitting for the solar cell samples with AlGaN layers. It's also worth noting that the voltage-band gap offsets (W_{oc}) of 1A, 1B, 1C and 2B are smaller than 0.6 V, which acts as an indicator of superior material quality in InGaN MQW solar cells[49], [129]. Sample 2A showed lower V_{oc} possibly due to the inferior material quality. Additionally, the J_{sc} value of the reference sample is only 0.87 mA/cm^2, while the values for samples with AlGaN layers are larger than 1.27 mA/cm^2, with an enhancement of more than 46%. The FF values of 1A to 2B range from 54% to 63%, while it's slightly lower in ref. (52.57%). As a result, the reference structure exhibited the lowest PCE of all (0.95%), which is largely limited by its J_{sc}. In contrast, sample 1A to 1C exhibited a significantly improved PCE of more than 1.6%, which demonstrates an increase of more than 68%. The best solar cell performance was achieved on Sample 1A which exhibited a V_{oc} of 2.20 V, a J_{sc} of 1.39 mA/cm^2, a FF of 60.52% and a corresponding PCE of 1.85% under 1 sun AM1.5G equivalent illumination. These results show the high potential of adopting AlGaN layers as an effective band engineering method to improve PV performance of InGaN solar cells.

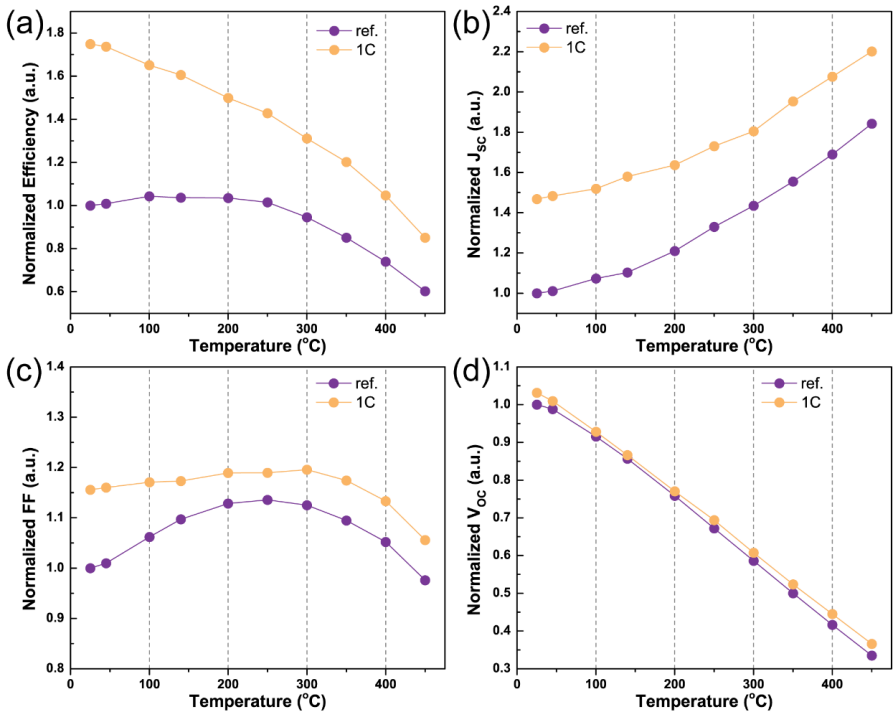

Fig. 5.6. The comparison of device parameters of normalized (a) power conversion efficiency, (b) short-circuit current (J_{sc}), (c) fill factor (FF), and (d) open-circuit voltage (V_{oc}) between sample reference and 1C from high temperature *J–V* measurements.

To further study the effects of AlGaN layers on the high temperature performance of InGaN solar cells, we performed high temperature *J–V* measurements ranging from 25°C to 450°C. Figure 5.6 presents the comparison of device parameters of normalized (a) conversion efficiency, (b) J_{sc}, (c) V_{oc}, and (d) FF between sample reference and 1C extracted from high temperature *J–V* measurements. To better compare the key device parameters under varying temperatures, we normalized each collection of parameters with the corresponding values of the reference at 25°C. Other InGaN solar cell devices with AlGaN layers that are not shown here exhibited similar trends as Sample 1C. Figure 5.6(a) shows that the efficiencies of 1C are much higher than that of the reference sample across the entire temperature range. It's worth noting that the difference in efficiencies between

the two samples reduces as temperature increases. With an increase in temperature, the bandgap energies of AlGaN layers decrease and the thermionic emission rate of photogenerated carriers rises. Those two effects together result in the less pronounced enhancement effect originated from AlGaN layers. A similar trend was observed for J_{sc} values of the two samples as shown in Fig. 5.6(b). Furthermore, an increase of FF up to 300°C was observed on both samples which is shown in Fig. 5.6 (c). This rollover phenomena in FF can be ascribed to the trade-off between carrier escape and recombination at high temperatures, which has also been identified in previous reports on InGaN/GaN MQW solar cells[37], [44]. Finally, both devices showed the similar values and trends for V_{oc} as shown in Fig. 5.6(d). This similarity originated from the temperature-dependent behaviors of the intrinsic carrier concentration and essentially the bandgaps of III-nitrides[130]. Consequently, the reference InGaN solar cell samples shared many similarities in PV performance with previous reports[37], [44], [49]. Nevertheless, InGaN solar cells with AlGaN layers completely outperformed the reference solar cell samples in almost every aspect of PV performance across the entire temperature range in measurements.

5.4 Summary

In summary, we have performed the comprehensive study on energy band engineering of InGaN MQW solar cells using AlGaN electron- and hole-blocking layers and demonstrated that such approach can effectively improve the PV performance of InGaN MQW solar cells. Energy band simulation and TRPL results showed that the carrier collection and carrier lifetime were improved significantly with the incorporation of AlGaN layers in the InGaN solar cells. The illuminated *J–V* measurements further

confirmed that J_{sc} benefited most from this design and increased more than 46%. The PCE of the solar cell device with AlGaN layers almost doubled over the reference structure. Under elevated temperatures, those with AlGaN layers also achieved better performance than the reference sample. These results demonstrate the feasibility and practicality of the adoption of AlGaN layers in the InGaN MQW solar cell structures for further improving the carrier collection process. This engineering of energy band therefore has the full potential to enable high efficiency InGaN solar cells for both room temperature and high temperature applications.

CHAPTER 6

RELIABILITY ANALYSIS OF INGAN/GAN MULTI-QUANTUM-WELL SOLAR CELLS UNDER THERMAL STRESS

6.1 Motivations and research background

III–nitride (III–N) material system has attracted extensive research interests in both electronics and optoelectronics, including high-electron-mobility transistors [131], power diodes [103], [104], [132], solid-state lighting [91], [110], [133], photovoltaic (PV) [3], [4], [60], [61], photodetectors [95], [134], [135] and visible light communication[112]. Due to their unique properties, such as tunable wide bandgaps [118], high absorption coefficient, high thermal stability, and outstanding radiation resistance [2], InGaN materials have also been proposed as ideal candidates for PV applications especially for high temperature operation or under harsh environment. For example, InGaN solar cells have been proposed for applications in thermal (PVT) hybrid solar collector systems [136], terrestrial concentrated PV systems, [17] and those for space explorations [4]. For next generation concentrated PVT hybrid systems, a higher operation temperature (> 400°C) due to higher concentrations are required when comparing to conventional concentrated PV systems. For space missions near the Sun, the operating temperature of the PV systems can range from 450°C for the Mercury mission [137], to 1400°C for the Solar Probe mission [138]. Therefore, efficient and reliable operation of solar cells under high temperatures is critical for these applications, where III-N materials and devices hold great promise [138], [139].

By virtue of their large bandgaps and high atomic displacement energies [140], III–N materials and devices are promising for high temperature applications. To date, high temperature operation of III–N devices has been theoretically predicted and experimentally

demonstrated up to 600°C in air and 1000°C in vacuum [141]–[145]. For III-N InGaN solar cells, high efficiency operation at 300°C temperature have been demonstrated [37], [40], [57], [146], which is superior to traditional Si or III-V solar cells. Despite the promising results, very few studies on the thermal reliability of InGaN solar cells exist, and their degradation mechanisms under high temperature are still unclear. In addition to crystal qualities, other device parameters such as metal contacts, passivation layers, and surface properties of the solar cell will also play significant roles in determining the thermal reliability of devices under high temperature. For example, recent study has shown that the semiconductor/metal interface of p–GaN/Ni/Au contacts is particularly vulnerable with Ni diffusion in GaN layers at high temperature and eventually crack after 700°C thermal treatment[143]. This will lead to degraded contact performance in InGaN solar cells under high temperatures. In contrast, n–GaN/metal contacts, typically formed in Ti/Al bilayers, were found to be thermally stable, possibly due to intermetallic compounds and high annealing temperatures [142], [147], [148].

In this study, we perform comprehensive study on the thermal stability of InGaN multi-quantum-well (MQW) solar cells under thermal stress at 400°C, 450°C and 500°C. Both *ex situ* electrical measurements and materials characterizations were performed to analyze the possible degradation mechanisms of InGaN solar cells under high temperature conditions. After thermal stress testing, the external quantum efficiency (EQE) spectra of the devices showed small degree of degradation, while the short-circuit current (J_{sc}) remained nearly constant for all samples. The reduction of energy conversion efficiency was mainly attributed to the drop of open-circuit voltage (V_{oc}), possibly due to the degraded contact performance under thermal stress. Furthermore, by fitting the Arrhenius equation,

the failure lifetime of the InGaN solar cells under different temperatures were also obtained. These results suggest that while InGaN solar cells have high thermal stability, the degradation in metal contact could be the major limiting factor for these devices under high temperature operation.

6.2 Experimental details

The InGaN MQW solar cell epi-structures were grown by conventional metal-organic chemical vapor deposition (MOCVD) on (0001) sapphire. The indium incorporation was determined to be 16% using photoluminescence measurements and was further verified using HRXRD measurements. The device structure consists of 2 μm Si-doped n–GaN ([Si]=3×10^{18} cm^{-3}), 125 nm highly Si–doped n^+–GaN ([Si]=2×10^{19} cm^{-3}), 15 periods of InGaN (3 nm)/GaN (6.6 nm) MQWs, 110 nm Mg–doped p–GaN and 10 nm highly Mg-doped p^+–GaN contact layer. The InGaN epi-structures were processed into solar cell devices with 1 mm × 1 mm mesas using standard contact lithography and inductively coupled plasma (ICP) etching. Ti/Al/Ni/Au ring contacts and Pd/Ni/Au grid contacts were deposited around the perimeter and on the top of the mesas, respectively. Both contacts were deposited via electron beam evaporation and then annealed at 500°C in N_2 atmosphere for 5 minutes using a rapid-thermal annealing process. None of the solar cell devices were coated with ITO or current spreading layers. The schematic structure of the InGaN MQW solar cells is shown in Fig. 6.1.

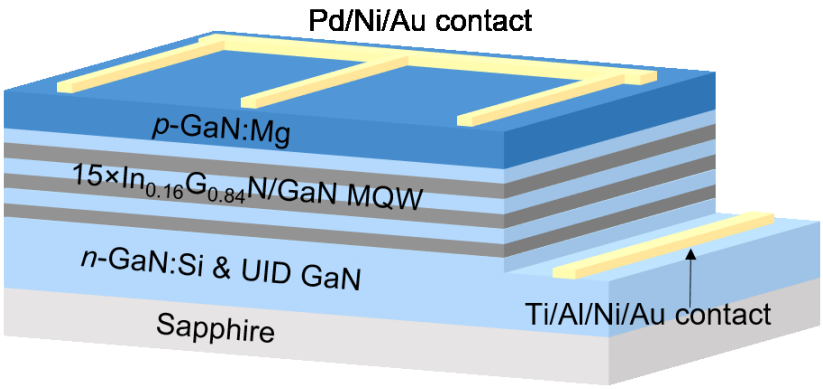

Figure. 6.1. The schematic structure of InGaN MQW solar cell samples investigated in the thermal stress testing.

The crystal qualities of the InGaN MQW solar cell samples before and after the thermal stress treatment were characterized by High Resolution X-Ray Diffraction (HRXRD) measurement using PANalytical X'Pert Pro materials research X–ray diffractometer (MRD) system with Cu Kα radiations. A hybrid monochromator and a triple axis module were used for the incident and diffracted beam optics, respectively. Illuminated *J–V* measurements were taken using an Oriel Class A Solar Simulator at 1 sun condition under AM1.5D spectrum. EQE measurement data were collected using an Oriel QEPVSI quantum efficiency measurement system and calibrated with a reference Si photodetector. More details on *J–V* and EQE measurements can be found on reference [61], [125]. For thermal stress testing, the InGaN solar cell devices were subject to 400°C, 450°C and 500°C in N_2 atmosphere using the Minibrute furnace. The time duration for each thermal stress period was set to be 2 hours. The devices were taken out from the furnace, and cool down to room temperature for *ex situ* electrical and materials characterizations. After all measurements, the devices were placed back in the furnace for another 2-hour period of thermal stress. The total time for the thermal treatment is 8 hours.

6.3 Results and discussions

Before device characterizations, HRXRD measurement was performed to analyze the material quality of the samples. (002) symmetric and (102) asymmetric plane rocking curves (RCs) were measured before and after each period of thermal stress. The extracted full-width-half-maximum (FWHM) values from (002) and (102) plane RCs are shown in Figs. 6.2 (a) and 6.2(b). The screw and edge dislocation densities were also calculated based on the following equation [149]:

$$\rho = \frac{\beta^2}{4.35\vec{b}^2} \tag{6.1}$$

where ρ is the dislocation density; β is the FWHM value and $\vec{b}$ is the Burgers vector. For samples under 400 °C and 450 °C stress, considering the variation from instrumental and measurement factors, FWHM values of (002) and (102) RCs are nearly constant with variations within 5%. The largest and smallest FWHM value of (002) RCs are 247 arcsec and 235 arcsec under 400 °C, and 240 arcsec and 231 arcsec under 450 °C, respectively. For (102) RCs, those values range from 272 arcsec to 265 arcsec under 400 °C and from 267 arcsec to 251 arcsec under 450 °C, respectively. These results indicate that material quality remains nearly unchanged throughout the thermal stress testing. Furthermore, for samples under 500 °C stress testing, is was observed that the WFHM decrease considerably [-13% for (002) and -9% for (102) RCs]. These reduced FWHM values suggest that the dislocation density in the samples reduced as thermal stress testing proceeded. This improvement of material quality can be attributed to the quenching effect on the epitaxial layers. This effect has also been observed in another studies, where InGaN solar cell samples had been annealed at 450°C or higher temperatures and QW re-homogenization

was observed in transmission-electron-microscopy study [150], [151]. These results show that moderate thermal stress (e.g., 400 – 500°C will have minimum negative impact to the material quality of InGaN solar cells. This is also consistent with the fact that III-N materials are typically epitaxially grown under extremely high temperature (e.g., ~ 1000°C), and therefore should be robust under high temperature stress.

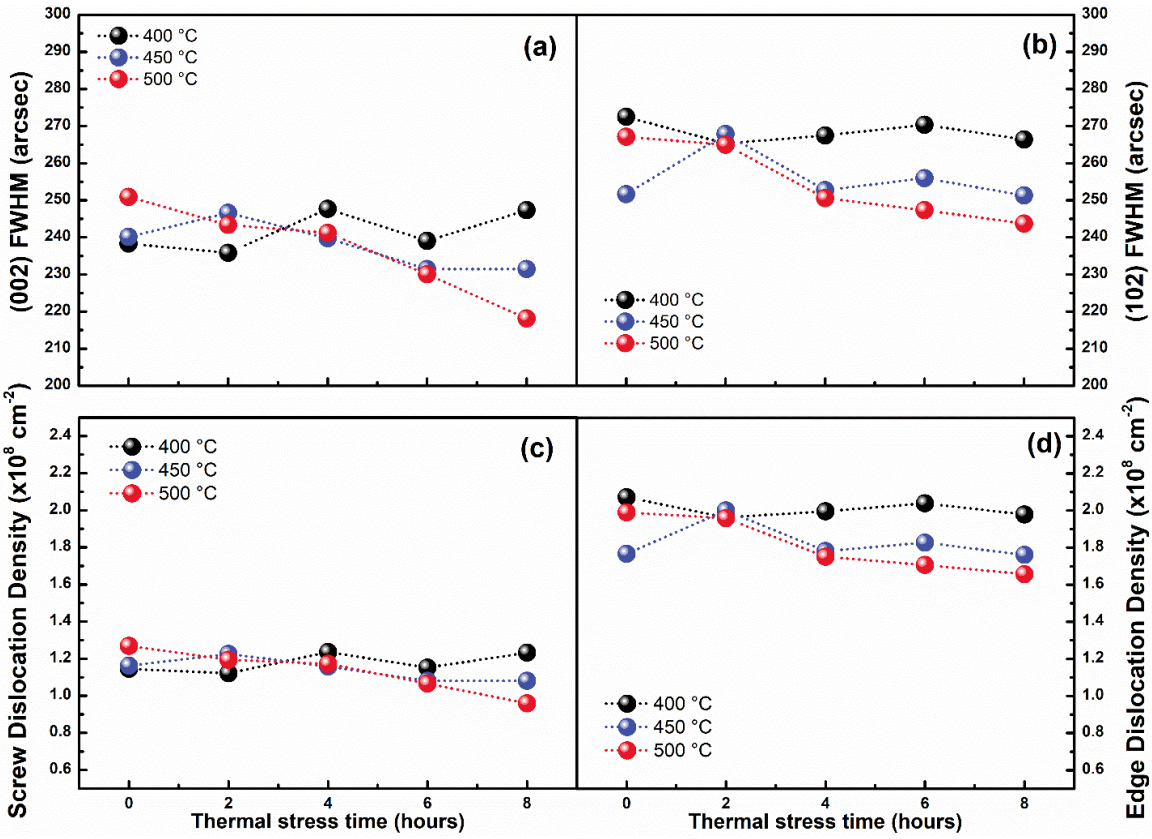

Figure. 6.2. The extracted full-width-half-maximum (FWHM) values from (a) (002) and (b) (102) planes RCs for InGaN solar cell samples. The calculated screw and edge dislocation densities are shown in (c) and (d), respectively.

Figure 6.3 shows the time evolution of the representative EQE spectra of InGaN samples under (a) 400 °C, (b) 450 °C and (c) 500 °C thermal stress testing, respectively. Overall, all the samples exhibit robust thermal reliability in terms of EQE performance.

With increasing stress time, EQEs in the short and long wavelength regime are almost constant at all temperatures, while small variations around the peak EQE regions were observed possibly due to the variation of measurements from the setup. The robust EQE performance stems from the robust material nature of III-N materials. This also corresponds to the nearly steady values of J_{sc}, which will be discussed in detail later.

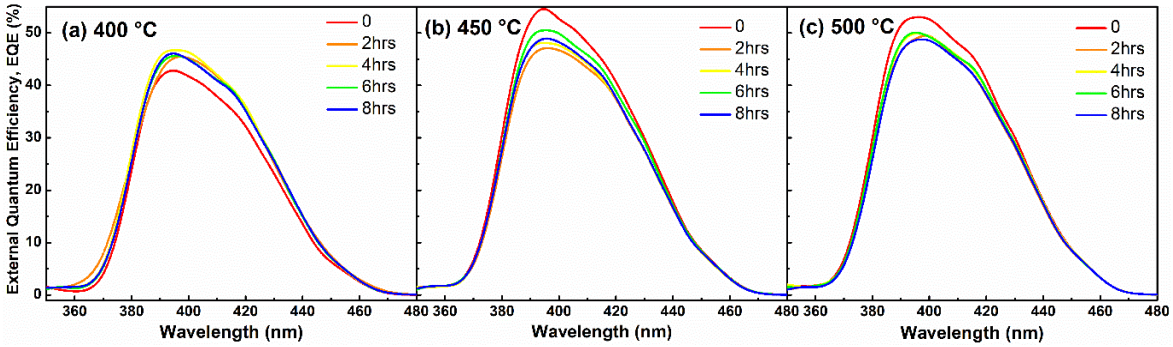

Figure. 6.3. The time evolution of the representative EQE spectra of the InGaN solar cell samples under (a) 400 °C, (b) 450 °C and (c) 500 °C thermal stress testing, respectively.

Figure 6.4 presents the illuminated current density–voltage (*J–V*) measurements of devices as a function of stress time for InGaN solar cells under (a) 400 °C, (b) 450 °C and (c) 500 °C thermal stress, respectively. Figure 5 shows the extracted values of (a) V_{oc}, (b) J_{sc}, (c) fill factor (FF) and (d) energy conversion efficiency from the *J–V* curves in Figs. 6.4(a)–4(c). Both J_{sc} and FF showed minimal variation with increasing stress time at all temperatures. The trends of J_{sc} values are also in good agreement with the EQE spectra, which shows strong resistance to thermal stress. At 400°C stress, minimum degradation is observed in V_{oc} and the efficiency remains almost constant around 1.4%. While at 450 °C stress, V_{oc} reduces gradually as stress time increases, from 2.05 V (0 hr.) to 1.99 V (4 hrs.) and then 1.38V (8 hrs.). The conversion efficiency of the solar cell is the product of V_{oc}, J_{sc} and FF. Since J_{sc} and FF are almost constant in this study, the conversion efficiency is

predominately determined by the V_{oc} of the InGaN solar cells. Therefore, the efficiency reduces from 1.52% (0 hr.) to 1.42% (4 hrs.) and then to 1.10 % (8 hrs.). At 500 °C, V_{oc} degrades more severely, which ranges from 2.03 V (0 hr.) to 1.22 V (4 hrs.) and then 1.15V (8 hrs.). Accordingly, the efficiency of the solar cells drops from 1.42% (0 hr.) to 0.84% (4 hrs.) and then to 0.76 % (8 hrs.). In addition, the leakage current at negative bias for the InGaN solar cells increases dramatically, as shown in Fig. 5(c), which indicates a strong degradation in junction behavior. From above results, the reduction in V_{oc} appears to be the major degradation mechanism in InGaN solar cells under the thermal stress. Since the thermal stress had minimum impacts on the material quality of the InGaN solar cell samples (as indicated from previous HRXRD studies), we performed comprehensive electrical characterizations on the metal contacts of the InGaN solar cells under thermal stress. Electrical property of N-type metal contacts was also measured and minimum degradation was observed (data not shown here).

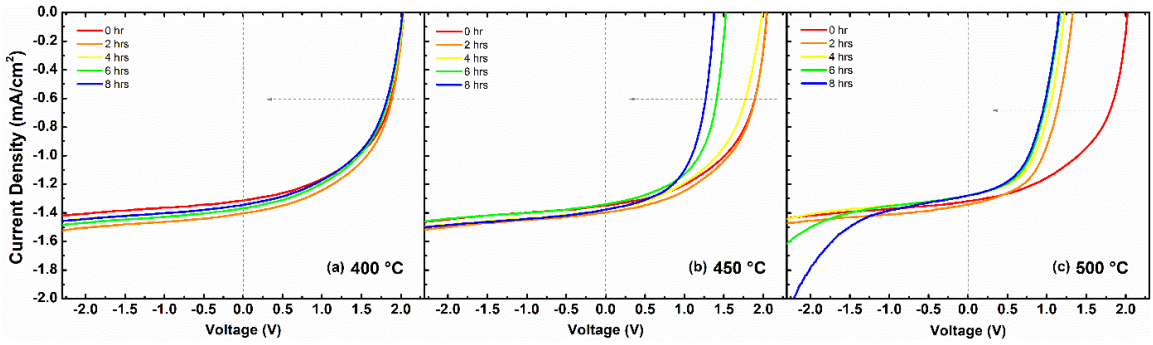

Figure. 6.4. The illuminated current density–voltage (*J–V*) curves as functions of stress time for 3 InGaN solar cell devices under (a) 400 °C, (b) 450 °C and (c) 500 °C thermal stress testing, respectively.

The electrical behavior of p-GaN/metal contact was investigated by transmission line method (TLM) at room temperature (RT) after samples were taken out of the furnace.

Figure 6.6 presents the time evolution of I–V characteristics of the p-GaN/Pd/Ni/Au contacts (20 μm TLM) of the InGaN solar cell devices under (a) 400°C, (b) 450°C and (c) 500°C thermal stress testing. For samples at 400°C stress testing, the contact was affected to a certain extent but still maintained a "semi-ohmic" behavior. At 0.5V bias, the current drops from 2.76×10^{-5} A (0 hr.) to 2.10×10^{-5} A (4 hrs.) and then to 1.86×10^{-5} A (8 hrs.). However, for those solar cells at 450°C and 500°C stress testing, the contact behavior changes dramatically, from ideal ohmic to the rectifying Schottky behavior. Moreover, the sample under 500°C stress experienced much more severe degradation than the one under 450°C stress. Theoretically, the V_{oc} of a solar cell can be determined from a diode equation as [152]:

$$V_{OC} = \frac{nkT}{q} \ln\left(\frac{J_{SC}}{J_0} + 1\right) \tag{6.2}$$

$$J_0 = J_{0,bulk} + J_{0,contact} = J_{0,bulk} + qS_{eff}(\Delta p + \Delta n) \tag{6.3}$$

where n is the ideality factor; T is the temperature; k is Boltzmann's constant; q is the electron charge; J_0 is the dark saturation current density; S_{eff} is the effective surface recombination velocity, and Δp and Δn are excess minority carrier concentrations near the contact interface. As contact properties are compromised, a large amount of defect states near the contact/p-GaN interface after thermal stress were generated. These defects or trap states result in the increasing of the surface recombination current, which leads to the rising $J_{0,contact}$ and thus the reduced V_{oc}. The schematic band diagram of metal/p-GaN contact of InGaN MQW solar cell samples after the thermal stress testing is shown in Fig.S1 in supplementary information. Furthermore, Fig. S2 shows the scanning electron microscopy (SEM) images of p-type metal contacts before and after thermal stress. It can be observed

that the surface morphologies of the metal contacts became rougher after the thermal stress. Bubbles and cracks on metal contacts were observed for sample after 500°C thermal stress. This contact morphology degradation after thermal stress is also consistent with previous studies[147], [153]. The compromised contact behavior is therefore likely to contribute to the reduction of V_{oc} and efficiency of the solar cell devices.

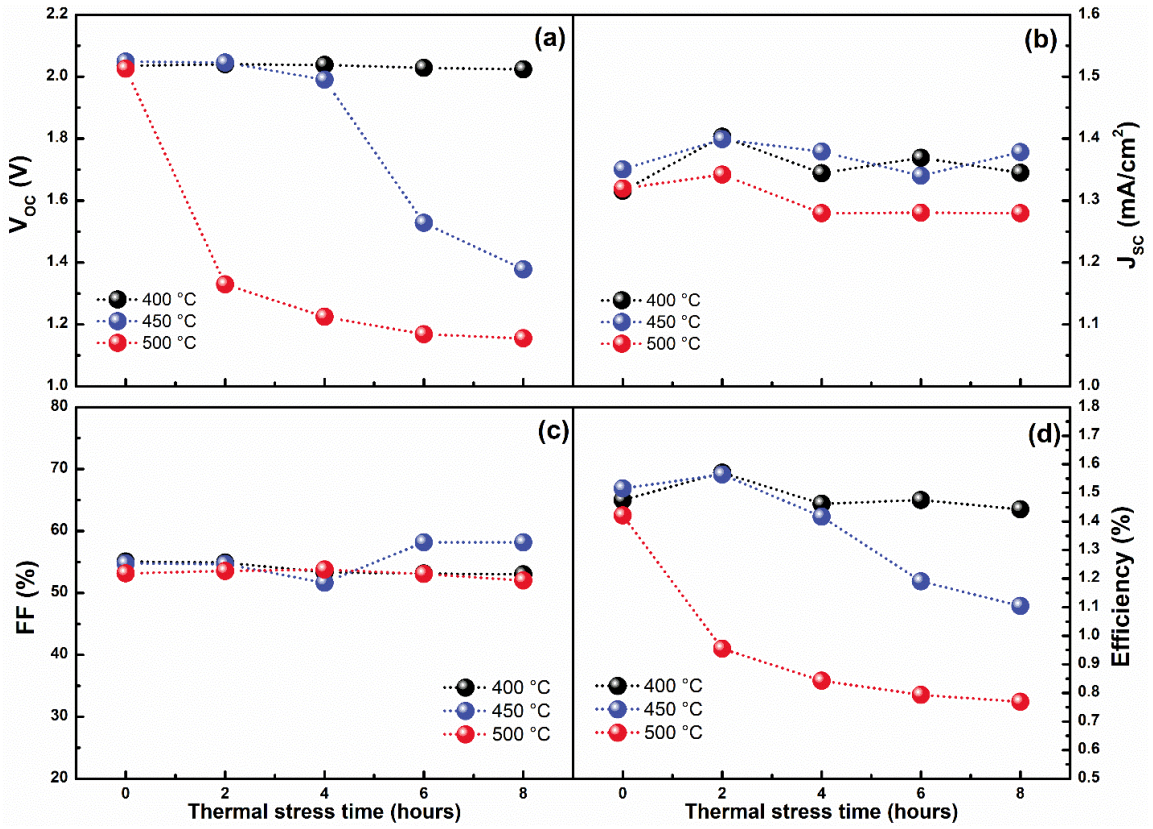

Figure. 6.5. The extracted values of (a) open-circuit voltage (V_{oc}), (b) short-circuit current (J_{sc}), (c) fill factor (FF), and (d) energy conversion efficiency for the InGaN solar cells from *J–V* curves in Figs. 6.4(a)–4(c).

Dark *J–V* measurements were further performed to analyze the electrical properties of InGaN solar cell samples after thermal stress testing. Based on the equation [152]

$$\frac{dV}{dJ} = R_S + \frac{nkT}{q}(J + J_{SC})^{-1} \quad , \tag{6.4}$$

the series resistances (R_s) and ideality factor n of the devices were extracted from the intercepts of the linear fitting results for plots of dV/dJ vs $1/(J+J_{SC})$, which are presented in Fig. 6.7. The inset tables show the extracted values of R_s and n. The large ideality factor n over 2 can be caused by several mechanisms such as tunneling effects, leakage currents, and defect-related generation and recombination at the contacts and/or in the bulk of devices [154], [155]. All devices exhibited increased n after thermal stress. One possible reason may be more leakage paths generated during the process of thermal stress. Another reason can be related to the degraded contact behaviors after thermal stress as shown in Fig.5. Furthermore, the InGaN solar cell under 500°C stress showed the largest increase of n values. This is consistent with the large leakage current observed in Fig. 6.4(c).

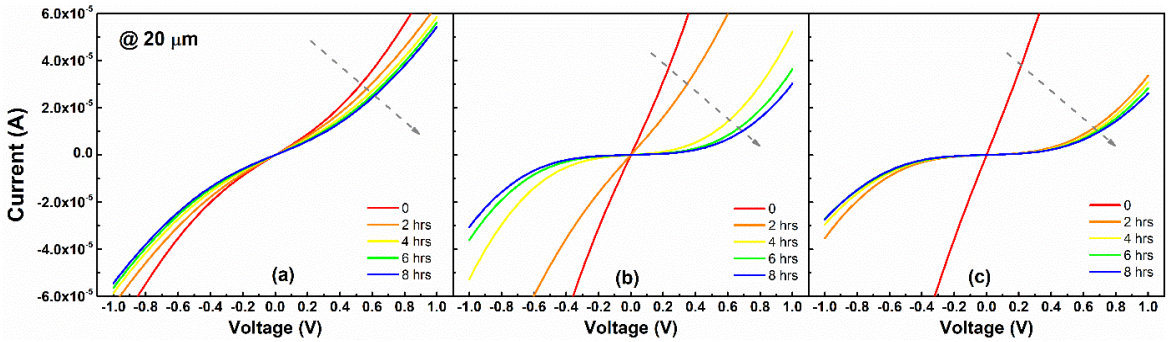

Figure. 6.6. The time evolution of I–V characteristics of the p-GaN/Pd/Ni/Au contacts (20 μm TLM) for 3 InGaN solar cell samples under (a) 400 °C, (b) 450 °C and (c) 500 °C thermal stress testing.

Another possible mechanism that is responsible for the degradation of *Voc* in InGaN solar cell is the formation of Schottky diodes between p metals and p-GaN after

thermal stress, as evidenced by Fig.6.6. The Schottky barrier height will reduce the forward voltage across the solar cell when the device is illuminated, thus decreasing the *Voc*.

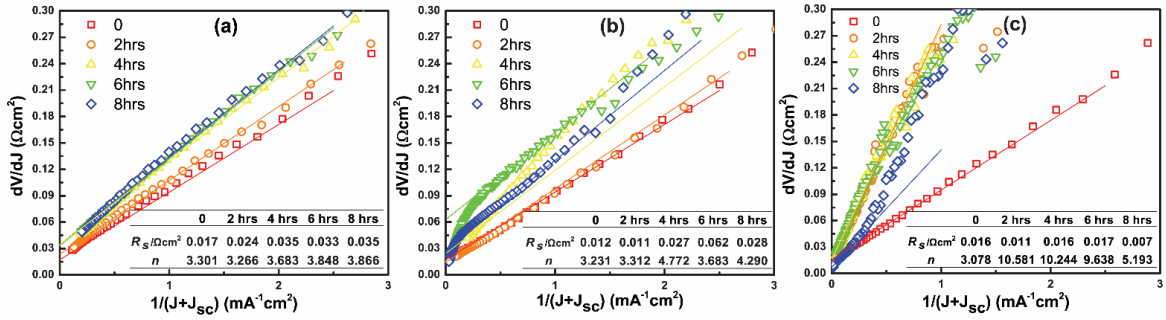

Figure. 6.7. Plots of *dV/dJ* vs *1/(J+J_{SC})* and the linear fit curves for the InGaN solar cell devices. The inset tables show the extracted series resistance (R_s) and ideality factor *n*.

The Arrhenius model was employed to predict the failure lifetime (t_f) of InGaN solar cell samples, which is a standard approach for microelectronic reliability study [156], [157]. It is often presented as the following equation: $t_f = Ae^{\frac{E_a}{kT}}$, where A is a scaling factor and E_a is the activation energy (eV) for the specific failure mechanism at temperature T. It can be further derived as: $\ln t_f = E_a \cdot \frac{1}{kT} + \ln A$. The assumption here is that the degradation mechanisms are the same in the range of 400 °C and 500 °C. By linearly fitting the plots of efficiency vs. stress time, and defining t_f as the value when efficiency drops to 1/3 of its initial value, we can obtain t_f for the solar cells samples, which are 133.8, 19.1 and 11.2 hours, respectively. And the activation energy, E_a = 1.124 *eV*, and the scaling factor, A= 4.244× 10^{-7} *h*, can be extracted via fitting the Arrhenius plot in Fig. 8(b). Therefore, the estimated lifetime for InGaN solar cells is 3244 hours at 300°C, 523 hours at 350°C, and 55 hours at 425°C. Note that passivation layers were not coated in ours

devices. The estimated lifetime will thus be expected to be greatly improved if they are included.

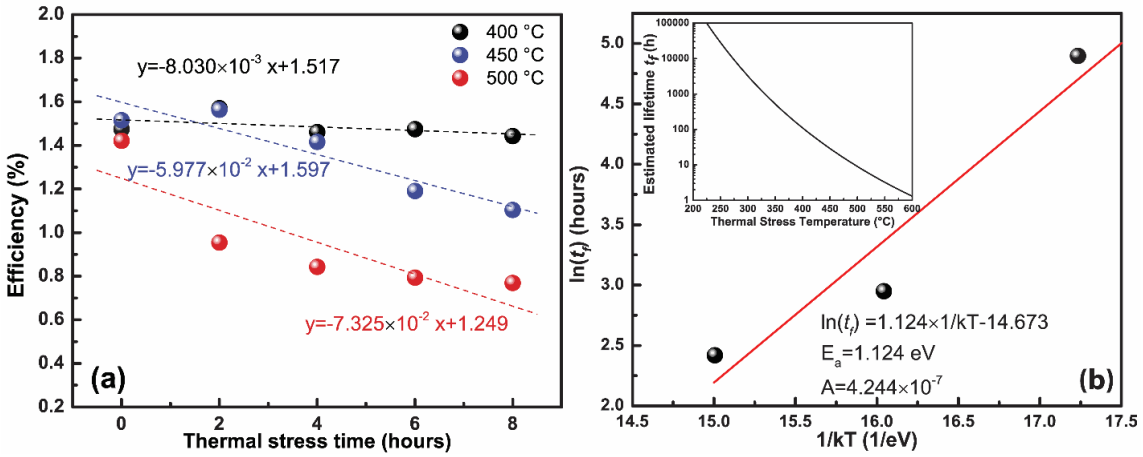

Figure. 6.8. (a) Energy conversion efficiency as a function of stress time for the InGaN solar cell devices under 400 °C, 450 °C and 500 °C thermal stress testing and their corresponding linear fittings. (b) Arrhenius plot of ln(t_f) vs 1/kT for the InGaN solar cells. The inset shows the estimated failure lifetime under different temperatures.

6.4 Summary

In conclusion, we studied the thermal stability of InGaN solar cells by employing thermal stress testing in N_2 under 3 different temperatures: 400°C, 450°C and 500°C. The stable EQE characteristics reveal the thermally robust nature of InGaN solar cells. Analysis of J–V curves shows that the reduction of V_{oc} is mainly responsible for the degradation of efficiency after thermal stress, where J_{sc} and FF are almost constant. Furthermore, results from TLM and HRXRD measurement suggest that the deteriorated contacts under thermal stress may be the major degradation mechanisms for InGaN solar cells, while the crystal quality of InGaN had minimum negative impacts from the thermal stress. Additionally, we also estimated the failure lifetime of InGaN solar cells under different temperatures by

fitting the Arrhenius model. Our results show that InGaN solar cells are capable of maintaining PV performance under high temperature, and special attention has to be paid towards the design and fabrication of metal contact of InGaN solar cells for high temperature operations.

CHAPTER 7

HIGH-TEMPERATURE POLARIZATION-FREE III-NITRIDE SOLAR CELLS WITH SELF-COOLING EFFECTS

7.1 Motivations and research background

High performance solar cells operating at high temperatures (e.g., > 300°C) are highly desired for high temperature photovoltaic (PV) applications, such as space missions near the Sun[137], [158]–[160], terrestrial photovoltaic thermal (PVT) hybrid solar collector systems[136] and concentrating solar power (CSP)/PV hybrid systems[161]. For example, the perihelion distance of Mercury is 0.307 astronomical units (AU) from the Sun. This resulted in an extremely high temperature of ~400°C at the Mercury planet surface[137], presenting a significant challenge for the efficient generation of solar power for spacecraft in NASA missions. Similarly, high operation temperature (> 300°C) is also a critical requirement for the next-generation terrestrial PVT hybrid system due to the concentrated solar power[162]. For CSP/PV hybrid systems, InGaN PV cells have been proposed to integrate with the current CSP systems as the photovoltaic topping cells[162]. This simultaneously allows for the generation of electricity through sunlight and the storage of dispatchable heat that can theoretically improve the efficiency by 46% compared to the CSP system alone. The current high temperature electronic technologies typically utilize active cooling process, which is however undesirable in these applications as it consumes a large amount of power and reduce the total efficiency of the system. Therefore, there is an urgent need for developing solar cells based on new PV materials that enables efficient operation at high temperatures.

Solar cells based on conventional III-V semiconductors, e.g., GaAs[163], [164], GaP/AlGaP[158], [165], AlGaInP[166] and even SiC[160], have been researched for high temperature applications with limited success. The intrinsic PV conversion efficiency of these devices typically showed a sharp decrease with increasing temperatures, i.e., these cells exhibit a negative temperature coefficient[164], [167]. For example, GaAs solar cells were reported with an absolute efficiency drop of 0.4% per 10-degree temperature increase at one-sun and failed shortly after exposure to high temperature[137], [163]. The escalating short-circuit current (J_{sc}) and dropping open-circuit voltage (V_{oc}) at high temperatures of these cells are also detrimental to the PV module operation. Furthermore, other extrinsic effects such as degradation in metal contacts further exacerbate the device performance at high temperature[62], [141], [168].

Wide bandgap III-nitride InGaN materials have emerged as a promising candidate for high temperature solar cells. $In_xGa_{1-x}N$ alloys have a tunable direct bandgap from ultraviolet (GaN ~ 3.4 eV) to near infrared (InN ~ 0.7 eV) spectral regions derived by changing the In compositions that provide a perfect match to the solar spectrum[2], [60], [118], [169]. Due to the relatively wider bandgap compare to Si or III-V, InGaN solar cells are also expected to have higher operation temperatures and superior radiation tolerance[2], [62]. These properties therefore make them particularly suitable for aforementioned space missions and terrestrial PVT hybrid systems. Despite these advantageous properties, InGaN solar cells are still a nascent field in PV due to well-known challenges in III-nitrides such as high defect density due to lack of native substrates[4]. The first demonstration of III-nitride solar cell emerged around 2007 with InGaN/GaN *p-i-n* double heterostructure (DH) grown on *c*-plane sapphire substrates[3]. Later, it was realized that the performance

of InGaN solar cells can be further improved by utilizing strained InGaN quantum wells (QWs) or superlattice active layer structures, similar to the commercial III-nitride light-emitting diodes (LEDs) [15], [18], [170]. It was argued that these thin QW layers could mitigate defect formations that occur in thick InGaN layers and thus lead to improved device performance. With such an approach, single-junction InGaN QW solar cells with relatively high external quantum efficiency of ~ 50%, and decent J_{sc} and V_{oc} were demonstrated[17]–[19]. Several groups also reported that the PV performance of InGaN QW solar cells can be reasonably sustained at high temperatures (e.g., 300°C)[37], [40], [49], [63]. Despite these encouraging progresses, these conventional InGaN solar cells unavoidably suffer from the polarization-related effects from the adoption of *c*-plane sapphire substrates, which have profound impacts on the efficiency of InGaN solar cells at both the room temperature (RT) and high temperatures. At RT, the large polarization-induced electric field inside the InGaN/GaN QWs will lead to a large quantum barrier that hinders the carrier collection in solar cells[21], [171]. At high temperatures, the polarization-related effects are convoluted with thermal escaping, making it even more challenging to probe, analyze and engineer the carrier dynamics of InGaN solar cells. Recently, our group has demonstrated novel polarization-free InGaN QW solar cells with significantly improved carrier collection efficiency using nonpolar *m*-plane bulk GaN substrates[61]. The new devices offer exciting opportunities for III-nitride solar cells to break the current performance limit particularly at high temperatures.

In this study, we demonstrate the outstanding high temperature performance of III-nitride solar cells using polarization-free (i.e., nonpolar) InGaN/GaN multiple-quantum-wells (MQW). The InGaN solar cells showed a large working temperature range from room

temperature (RT) to 450°C, with positive temperature coefficients up to 350°C. The peak value of external quantum efficiencies (EQEs) of the devices showed a 2.5-fold enhancement from RT (~32%) to 450°C (~81%), which is distinct from all other solar cells ever reported. Time-resolved photoluminescence (TRPL) results reveal that an increase of over 70% in carrier lifetime in nonpolar InGaN MQW is partly responsible for the enhanced EQE. In addition, a thermal radiation analysis was performed on Si, GaAs, and III-nitride materials, which revealed a unique self-cooling nature of III-nitrides. These results offer new insights and strategies for the design and fabrication of high efficiency high temperature PV solar cells using III-nitrides, which will open up not just exciting possibilities but also breakthrough potential for transformative outcomes in solar cell efficiency and deployment.

7.2 Experimental details

Growth and structure parameters of nonpolar InGaN and GaAs solar cells.

InGaN MQW solar cells on nonpolar *m*-plane substrates were grown by conventional metal-organic chemical vapor deposition (MOCVD). The growth condition was designed to achieve the Indium incorporation around 15% in samples. The designed device consists of 1 μm Si-doped n-GaN ([Si]=5×10^{18} cm^{-3}), 10 nm highly Si-doped n^+-GaN ([Si]=1×10^{19} cm^{-3}), 20 periods of InGaN (6 nm)/GaN (10 nm) MQWs, 30 nm Mg-doped smooth p^+-GaN ([Mg]=1×10^{19} cm^{-3}), 120 nm Mg-doped p-GaN ([Mg]=3×10^{19} cm^{-3}), and 10 nm highly Mg-doped p^+-GaN contact layer ([Mg]=1×10^{20} cm^{-3}). None of these devices is coated with traditional ITO or current spreading layers.

The GaAs cell was grown on p-type Zn-doped 5° off-cut (001) GaAs substrates using a Veeco K475 As/P MOCVD system. The structural details can be found on ref [122] .

Solar cell fabrication and characterization.

Then InGaN solar cell samples were processed into 1 mm x1 mm mesas by standard contact lithography and inductively coupled plasma (ICP) etching. Ti/Al/Ni/Au and Ni/Au grid contacts deposited via electron beam evaporation were employed as n and p metal contacts, respectively. More structural and fabrication details on InGaN solar cells can be found in ref [61], [62].

HRXRD measurement.

The nonpolar InGaN solar cell sample was characterized by high-resolution X-ray diffraction measurement using PANalytical X'Pert Pro materials research X-ray diffractometer (MRD) system with Cu Kα radiations. Hybrid monochromator and triple axis module are used for the incident and diffracted beam optics, respectively.

FIB and STEM imaging.

The nonpolar InGaN solar cell specimens for STEM imaging were prepared with an FEI Nova 200 Dual-Beam FIB system with a Ga ion source. A JEOL-ARM200F scanning transmission electron microscopy (STEM) operated at 200 KV and equipped with double aberration-correctors for both probe-forming and imaging lenses was used to perform high-angle annular-dark field (HAADF) imaging. The compositional distribution of In element in MQW layers was accomplished by acquiring the energy-dispersive X- ray (EDX) spectroscopic spectra of In element.

Illuminated current density–voltage (*JV*) and EQE measurement.

Solar cell parameters such as the open-circuit voltage, fill factor and power conversion efficiency were extracted from LIV measurements taken using an Oriel Class A Solar Simulator. The Newport Class A solar simulator generates a 4-inch-diameter

collimated beam using a xenon arc lamp and a series of filters designed to provide 0.1Wcm 2 at the surface of the testing stage. All *JV* curves of InGaN and GaAs cells were taken at 1 sun condition AM1.5G spectrum.

EQE measurement data were collected using under short-circuit conditions using an Oriel QEPVSI quantum efficiency measurement system and calibrated with a reference Si photodetector. This system is composed of a 150W Xenon arc lamp coupled with a Cornerstone 260 1/4m monochromator.

The nonpolar InGaN solar cell sample is around 0.55 cm × 0.55 cm, which is slightly larger than the mesa area of one GaAs cell (0.5 cm × 0.5 cm). In the future cell design we will aim for the same size of top and bottom cells.

A Linkam HFS600-PB4 stage capable of heating the samples up to 600 °C was used to perform the temperature-dependent measurements. For both the external quantum efficiency (EQE) and current- voltage (I-V) measurements, the temperature of the stage was increased from room temperature to 450 °C in steps of 25 – 50 °C with a ramp rate of 10-20 °C/min. Once the desired temperature was reached, the sample was kept at the specified temperature for another 3 min. The experimental setup did not allow for the simultaneous acquisition of the temperature- dependent EQE and I-V. Therefore, these measurements were performed on the same InGaN cell while separately on different cells on the same GaAs wafer. For the EQE and I-V measurements for filtered GaAs cell, InGaN solar cell sample was carefully placed on top of GaAs cell when the desired temperature was reached and it was at the open-circuit state.

Photoluminescence and time-resolved photoluminescence measurements

PL and TRPL measurements were done using a home-built system, where a picosecond 405nm pulsed laser diode (PDL 800-B) was used as excitation source. PL spectrum was collected by a Si array detector coupled with Horiba monochromator (TRIAX 320). TRPL was measured by a time-correlated single-photon counting system (TCSPC). A Si photomultiplier tube (PMT) detector is attached at the other output port of monochromator and its signal is then recorded by TCSPC board (SPC130 module).

Transmission and reflection spectra measurement

The transmission and reflectance spectra of fabricated nonpolar InGaN solar cell sample were characterized with LAMBDA 950/1050 UV/VIS/NIR Spectrophotometer from Perkin Elmer.

Emissivity measurement

The thermal radiation power density is obtained from experimentally characterized thermal emissivity of the solar cells by using a Fourier transform infrared spectrometer (Thermo Scientific Nicolet 6700). The absorptivity/emissivity spectra were obtained by subtracting the reflectance and transmittance from unity. The GaN, GaAs and Si substrates are all around 300 μm while the thickness of GaN grown on the sapphire is around 3 μm.

Simulation of band diagrams

The energy band diagrams of CdTe/MgCdTe, AlGaInP and InGaN/GaN double heterostructures were simulated using Silvaco ATLAS software. They all contain 6-nm absorbing layer and 10-nm barrier. The band structure parameters, the conduction and valence band offsets of CdTe/MgCdTe, AlGaInP and InGaN/GaN DHs were obtained from DiNezza *et al*[172], Meney *et al*[173] and Huang *et al*[61], respectively. Silvaco ATLAS

is a commercial device simulation tool based on the drift-diffusion model. MQW simulation is based on a parabolic quantum well model implemented within Silvaco ATLAS. The bound state energies are calculated solving the Schrödinger equation along discrete slices in the quantization direction.

7.3 Results and discussions

High-Temperature Characterizations of the Nonpolar InGaN/GaN MQW Solar Cells.

Figure 7.1(a) presents the schematic crystal planes of the polar c-plane (top) and the nonpolar m-plane GaN (bottom). Figure 1(b) shows the schematic zoom-in energy band diagrams of the active InGaN/GaN MQW regions of the two crystal planes. It can be seen that due to the large polarization-related effects, the energy band diagram of the MQWs on the conventional polar c-plane GaN is tilted. In contrast, the energy band diagram of the MQWs on the polarization-free nonpolar m-plane is flat. The distinct energy band profiles between two cases will have significant impacts on the carrier transport, leading to very different solar cell device performance under high temperatures. This will be discussed in detail in the following section. The complete energy band diagrams are shown in Figure S1. Figure 1(c) shows the schematic device structure for the fabricated nonpolar InGaN solar cell, while Fig. 1(d-f) show the cross-section high-angle annular dark-field (HAADF) scanning transmission electron microscopy (STEM) images of the nonpolar m-plane InGaN/GaN MQW solar cell structure with 20 periods of nominal 6-nm InGaN and 10-nm GaN MQW. The average thickness of one period of InGaN QW and GaN barrier is around 17.5 nm. The hexagonal wurtzite structure of GaN can be clearly identified from Figure 1 (e) and (f). Very high quality InGaN/GaN MQW structures were obtained as evidenced in the STEM images and high resolution X-ray diffraction (HRXRD) results in Fig.7.S2. The

EDX element mapping of In (displayed in blue false color) and the corresponding EDX spectrum profile along the growth direction are shown in the supplementary Fig.7.S3. The details of the epitaxial growth and fabrication processes for the solar cells can be found in Method section.

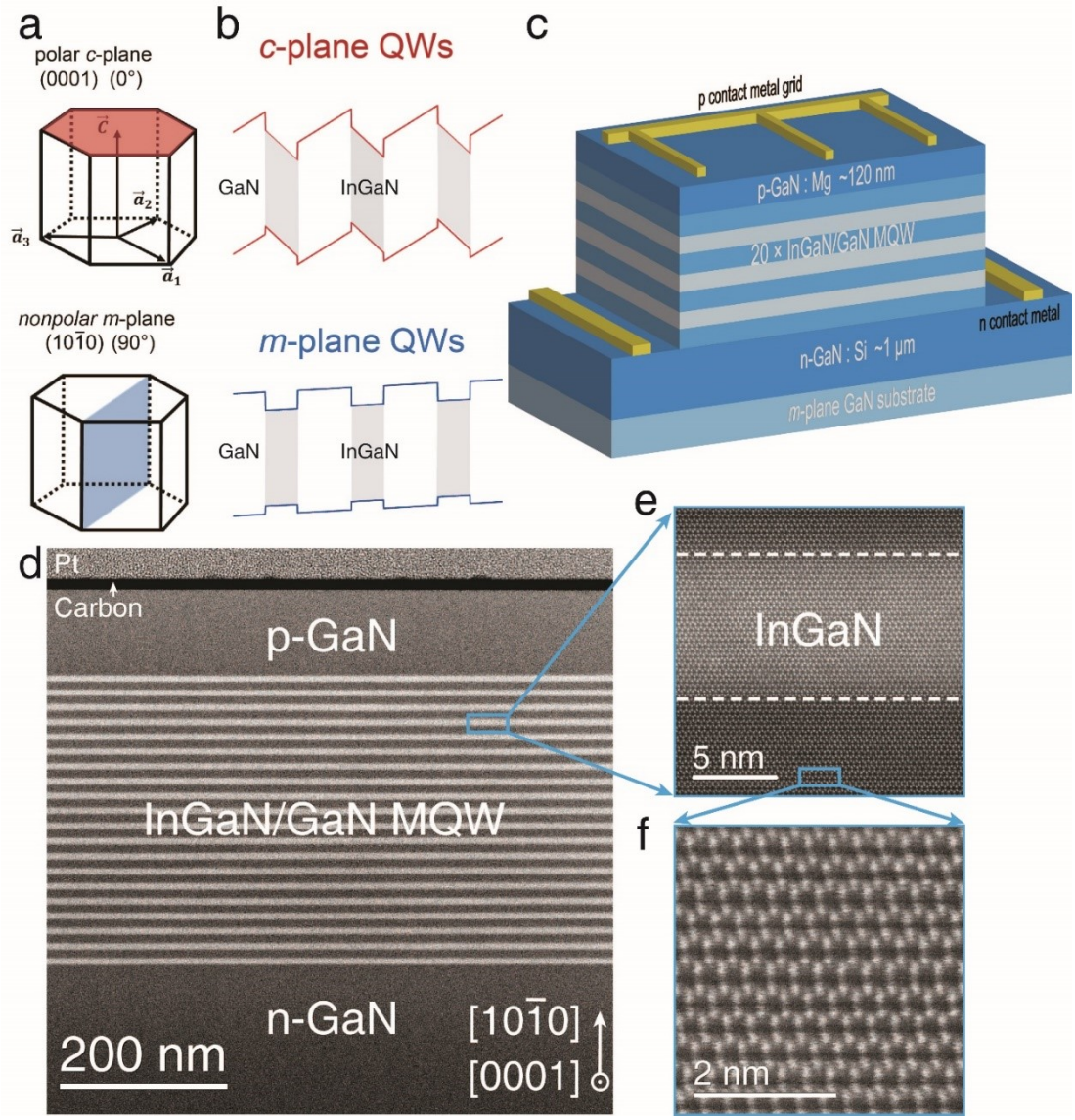

Figure 7.1**: a.** The crystal planes of the polar *c*-plane (top) and the nonpolar *m*-plane GaN (bottom). **b.** The schematic zoom-in energy band diagrams of the active InGaN/GaN MQW regions of the two crystal planes. **c.** The schematic device structure for the fabricated

nonpolar InGaN solar cell. **d-f.** The cross-section HAADF-STEM images of the nonpolar *m*-plane InGaN/GaN MQW solar cell structure with 20 periods of InGaN(6 nm)/GaN(10 nm) MQW. **d.** The HAADF-STEM image of the entire solar cell structure. **e.** The HAADF-STEM image of one InGaN/GaN QW on the atomic scale. The white dash lines are estimated interfaces between InGaN QW and GaN barrier layers and also serve as a guide to eyes. **f.** The zoom-in HAADF-STEM image of the GaN epilayer from Figure **1e**. The hexagonal wurtzite structure of GaN can be clearly identified. Upward is the growth direction.

The EQE performance of the fabricated nonpolar InGaN/GaN solar cell was characterized under various temperatures from 25°C to 450°C, and the results are shown in Fig. 2(a). As the temperature increases, the peak EQEs of the nonpolar InGaN solar cell continuously increase from ~32% at 25°C to ~81% at 450°C. This is distinct from previous reports[57], [71], as most solar cells show a large degradation in EQEs with increasing temperatures. Previous reports on polar InGaN solar cells have also shown that EQE performance degraded as temperature rose[40], [49]. Furthermore, the cutoff wavelengths in the EQE spectral of the nonpolar InGaN solar cells increases dramatically as the temperature increases (i.e., from ~435 nm at 25°C to ~480 nm at 450°C), due to the bandgap narrowing at high temperatures. In comparison, the onset wavelengths in the EQE spectral shows minimal changes with increasing temperatures. As a result, a broaden EQE spectral with enhanced peak EQE values were obtained from the nonpolar InGaN solar cells at high temperatures. This huge enhancement in EQE can also be attributed to 3 main physical mechanisms: (1) the thermally narrowing bandgap of InGaN along with the enlarged absorbing solar spectrum, leading to significant absorption boost of incident

photons; (2) the increased effective carrier lifetime at elevated temperatures. This indicates that longer lifetime enables more carriers to be collected at contacts, which can further facilitate more complete absorption of incident light in the active layers. As shown in Fig.3(c) and Fig.S4(c), higher effective lifetime in polar *c*-plane device contributed to higher power conversion efficiency and EQE at temperature below 150°C in Fig.S5. More details on carrier lifetime will be discussed in the following section. (3) The increased diffusion length at elevated temperature which contributed to the enhanced carrier collection and thus EQE. From the Einstein relation: $= \mu_{MQW} k_b T/q$, diffusion length can be calculated using $L^2 = D \cdot \tau = \mu_{MQW} k_b T/q \cdot \tau$, where μ_{MQW}, k_b, T, q, τ stand for carrier mobility in MQW, Boltzmann's constant, temperature, electrical charge and carrier lifetime, respectively. It's worth noting that μ_{MQW} here is not in bulk material and thus it's not dominated by phonon scattering [174]. Previous work on carrier transport across MQW demonstrates that effective mobility of both electrons and holes tend to increase through thermal-related carrier processes[175]. We can then safely conclude that diffusion length (L) of carriers improves at elevated temperatures by considering the increasing carrier lifetime (τ).

Figure 7.2(b) shows the temperature-dependent illuminated current density–voltage (*JV*) measurements of the nonpolar InGaN solar cell, while the extracted V_{oc}, J_{sc}, fill factor (FF) and power conversion efficiency (eff.) as a function of temperatures are plotted in Fig. 2(c). The V_{oc} of the nonpolar InGaN solar cell decreases monotonously at a rate of ~2.85 mV/°C in the range of 25°C – 450 °C. This is due to the increased carrier recombination (and thus the increased dark saturation current J_0) as temperature increases, which is consistent in other solar cell reports[40], [49], [176]. However, it is noteworthy that the J_{sc}

increases monotonously from 0.52 mA/cm^2 at 25°C to 1.91 mA/cm^2 at 450°C, which suggests a 3.7-fold enhancement and is closer to the ideal J_{sc} of Shockley–Queisser limit at corresponding bandgap (~2.31 mA/cm^2 at 2.85eV to ~4.67 mA/cm^2 at 2.58 eV for AM1.5G spectrum). This huge increase in J_{sc} also corresponds to the enhanced EQE spectra at elevated temperatures. The FF of the device shows a peak at 200°C due to the trade-off between V_{oc} and J_{sc}. This rollover phenomena in FF can be ascribed to the trade-off between carrier escape and recombination at high temperatures, which is also reported in other solar cells using double heterostructures[177]. As a result, the power conversion efficiency of the nonpolar InGaN solar cell increases monotonously from 0.55 % at 25°C to 0.94 % at 350°C, and then falls off to 0.812 % at 450°C. This large enhancement in solar cell efficiency up to 350°C has never been reported in other solar cell devices. This enhancement of conversion efficiency under elevated temperatures demonstrates the potential and feasibility of III-nitride-based solar cells for high temperature applications. Based on Shockley–Queisser analysis, the optimal bandgap of the solar cell changes from 1.4 eV at RT to ~2.0 eV at 500 °C [178]. Though Si and GaAs have the nearly optimal bandgaps at RT, they deviate from the optimal values as temperature rises, resulting in a reduced efficiency. In contrast, with the tunable bandgap property, III-nitrides can be further engineered to match the optimal value of bandgap for the corresponding temperature (above 450 °C), indicating the huge potential and feasibility of wide-bandgap III-nitrides for high temperature PV applications.

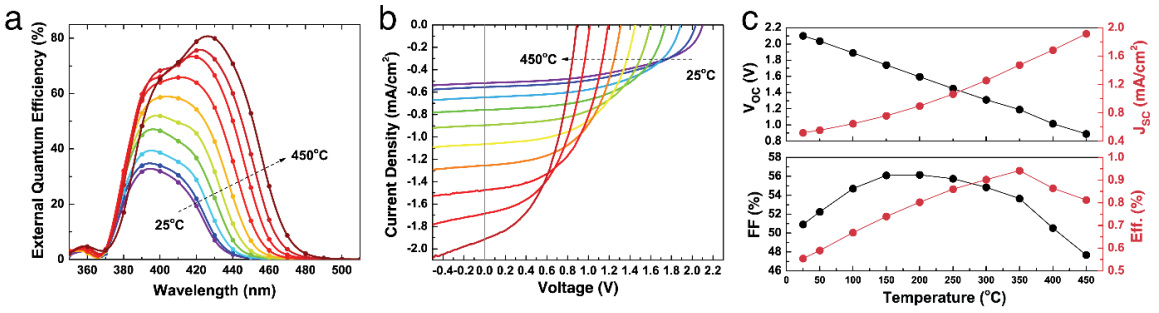

Figure 7.2**: a.** Temperature-dependent EQE spectral of the nonpolar InGaN MQW solar cell at different temperatures from 25°C to 450°C. **b.** Temperature-dependent illuminated *JV* measurements of the nonpolar InGaN MQW solar cell. **c.** Extracted V_{OC}, J_{SC}, FF and efficiency values as functions of temperatures.

Polarization-Effects in QW Carrier Escape at High Temperatures.

To explore the fundamental understanding on the high temperature performance of nonpolar InGaN solar cells, we studied the temperature-dependent optical properties and carrier dynamics for nonpolar and polar InGaN MQW samples using photoluminescence (PL) and time-resolved photoluminescence (TRPL) measurements. The power of the pulsed excitation source was chosen to approximate the actual light intensity of solar cells under operation. PL and TRPL spectra from RT to 400 °C of *m*-plane device are plotted in Figure 7.3 (a) and (b), respectively. Those of *c*-plane sample are plotted in Figure 7.S4. In Fig.7. 3(a), it's worth noting that strong PL peak intensity was observed for *m*-plane device even at high temperatures compared to its *c*-plane counterpart. This can be attributed to the strong radiative capability in *m*-plane III-nitride QW. On the other hand due to the strong yellow emission from III-nitrides, the PL peaks of MQW of *c*-plane sample are interfered and difficult to discern from 300°C. Therefore, TRPL spectra of *c*-plane sample in 300 °C

has very low signal/noise ratio and thus can be considered inaccurate to extract carrier lifetime.

The extracted temperature-dependent carrier lifetime for nonpolar InGaN/GaN MQW devices are plotted in Figure 7.3 (c). Same measurements were also performed on polar c-plane device and results are shown in Figure 7.S4 (a)-(c) for comparison. It's worthy to note that the lifetime of *m*-plane device rises as temperature increases and increases by over 70% at 400 °C compared to itself at RT. We attributed this surprising phenomenon to the strong radiative recombination ability of *m*-plane InGaN MQWs. This also corresponds to the relative strong PL emission at elevated temperatures for *m*-plane device shown in Fig.7.3(a). It has been observed and confirmed by previous literatures that *m*-plane InGaN QWs has large radiative recombination rate compared to *c*-plane counterparts[179]–[181] . On the other hand, *c*-plane device has shown an opposite trend compared to the nonpolar device.

The temperature-dependent carrier lifetime for nonpolar and polar InGaN/GaN MQW devices are also fitted to a carrier recombination model to determine the main recombination mechanism(s) under different temperatures. 3 major carrier mechanisms are considered in this analysis: radiative recombination (lifetime τ_{rad}), Shockley-Read-Hall recombination (lifetime τ_{SRH}), and thermionic emission (lifetime τ_{th}). For the QW structure we used in the experiment (6 nm InGaN QW and 10nm GaN barrier layer), the thermionic escape was found to be the dominant carrier transport mechanism[182], where the tunneling escape of carriers was treated as minor concerns. The analytical expressions of different temperature-dependent τ_{rad}, τ_{SRH} and τ_{th} are described in previous literature[183]. For simplicity, the aforementioned temperature-dependent lifetimes can be expressed as :

$$\tau_{rad} \propto C_{rad} \cdot T^{1.5} \quad (7.1)$$

$$\tau_{SRH} \propto C_{SRH} \cdot T^{-0.5} \quad (7.2)$$

$$\tau_{th} \propto C_{th} \cdot T^{-0.5} \cdot e^{\Delta E/kT} \quad (7.3)$$

Where ΔE is the barrier height for carriers, C_{rad} , C_{SRH} and C_{th} were temperature-independent coefficients for radiative recombination, Shockley-Read-Hall recombination and thermionic emission processes[181], [183]. Then effective lifetime τ_{eff} contains all three recombination processes:

$$\frac{1}{\tau_{eff}} = \frac{1}{\tau_{rad}} + \frac{1}{\tau_{SRH}} + \frac{1}{\tau_{th}} \quad (7.4)$$

Solid markers in Fig.3 (c) and Fig.S4(c) represent the effective lifetime obtained from TRPL measurements, while dash lines indicate the fitting curves to equations (7.1)-(7.4). It's worth noting that τ_{rad} is the only recombination process that positively correlates with temperature[183], [184]. For *m*-plane device, τ_{eff} increases from 0.72 ns at 25 °C to 1.29 ns at 400 °C, which is over 70% larger. TRPL Results suggests that *m*-plane device is mostly dominated by radiative recombination at all measured temperature range. In addition, this excitonic nature of the radiative recombination in *m*-plane sample can be directly attributed to the polarization-free quantum well structure. The larger overlap of wavefunctions and higher exciton binding-energy due to the nonpolar QWs have been reported to contribute to the enhanced radiative ability[181]. The radiative recombination lifetime will then increase due to this temperature-dependent excitonic nature of radiative recombination. In addition, thermionic emission process is not applicable in analyzing effective lifetime in nonpolar device and SRH recombination also plays a role at high temperatures since extracted PL lifetime of *m*-plane device are not completely proportional to $T^{1.5}$. This prolonged carrier lifetime also accounts for the enhanced J_{sc} at high temperatures.

On the other hand, *c*-plane device has shown the opposite trend compared to the nonpolar device. This indicates that SRH recombination and thermionic emission processes play a critical role at high temperatures. In addition, the radiative recombination lifetime of *c*-plane device is also about one order of magnitude larger than that of *m*-plane device. This also corresponds to strong polarization effect in *c*-plane QWs, leading to lower radiative probability.

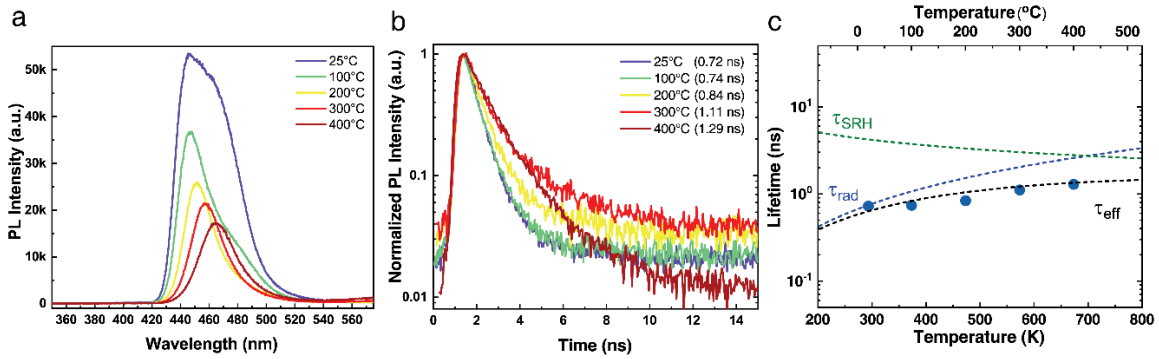

Figure 7.3. (**a).** Temperature-dependent photoluminescence (PL) and (**b).** time-resolved PL measurements of nonpolar InGaN/GaN MQW solar cell devices. (**c).** Extracted temperature-dependent carrier lifetime for this nonpolar devices (blue solid markers). The dashed lines indicate fitting results for τ_{eff} (black), τ_{rad} (blue) and τ_{SRH} (green).

Self-Cooling Effects in GaN Using Thermal Radiation Analysis.

To further investigate the physical nature of high temperature performance of III-nitrides, the emissivity measurement was taken and the thermal radiation power analysis was carried out where Si and GaAs were used as references. The calculations are performed by a finite-difference based thermal simulator, taking into account the solar cell absorbed power under AM 1.5G illumination, the heat dissipation by thermal radiation of the cell, as well as the non-radiative heat dissipation to the environment by conduction and

convection[185]. Figure 7.4a shows the calculated temperature difference between the InGaN solar cell and the heating stage at various heating stage temperatures. As a comparison, the temperature differences for GaAs and Si are also plotted. As shown in Fig. 4a, the temperature difference (absolute value) for III-nitride is significantly larger than the others and increases as the stage temperature increases. This is mainly due to the increased heat dissipation through thermal radiation of GaN cell at elevated temperatures (Fig. 7.4b). Similar trends are also observed for GaAs and Si cells. However, the temperature differences of those two cells are much smaller than GaN cell, due to the weaker heat dissipation through thermal radiation.

This outstanding heat dissipation capability through thermal radiation of III-nitride can also contribute to the low temperature coefficient of V_{oc} of InGaN-based solar cell compared to Si and GaAs. From the one-diode model, the expression for V_{oc} is $V_{OC} = \frac{nkT}{q}\ln(\frac{J_{SC}}{J_0}+1)$, where n is the ideality factor; q is the electron charge; J_0 is the dark saturation current density. Then the temperature coefficient of V_{oc} is defined as

$$C_{V_{OC}} = \frac{1}{V_{OC}^{300K}}\frac{\partial V_{OC}}{\partial T} = \frac{1}{T} + \frac{1}{V_{OC}^{300K}}\frac{nkT}{q}(\frac{1}{J_{SC}}\frac{\partial J_{SC}}{\partial T} - \frac{1}{J_0}\frac{\partial J_0}{\partial T}) \tag{7.5}$$

Moreover, J_0 is extremely sensitive to the temperature[186], as defined as $J_0 = CT^3\exp(-\frac{E_g}{kT})$, where C is the material parameter and E_g is the bandgap energy. Therefore, under the same stage/ambient temperature, the higher temperature difference (in absolute value) suggests less dark current density J_0 and less thermal bandgap narrowing. Thus for III-nitrides, the decreasing in V_{oc} will be suppressed and C_{Voc} is

smaller. For the nonpolar InGaN solar cell, it is -0.136 %/K for V_{oc} and is also in consistent with previous reports[40], [71] and far better than those of GaAs (-0.238 %/K) and Si cells (-0.329 %/K)[40], [130]. The lower thermal radiation power density of Si compared to GaAs also corresponds to the lower temperature coefficient of V_{oc} (higher in absolute value). Consequently, this self-cooling effect of III-nitrides can also potentially be beneficial for InGaN/III-V tandem or multijunction cells. The employment of an InGaN top cell is capable of reducing the operating temperature of the underlying III-V cells at elevated temperatures, as evidenced in Fig.7.4(c).

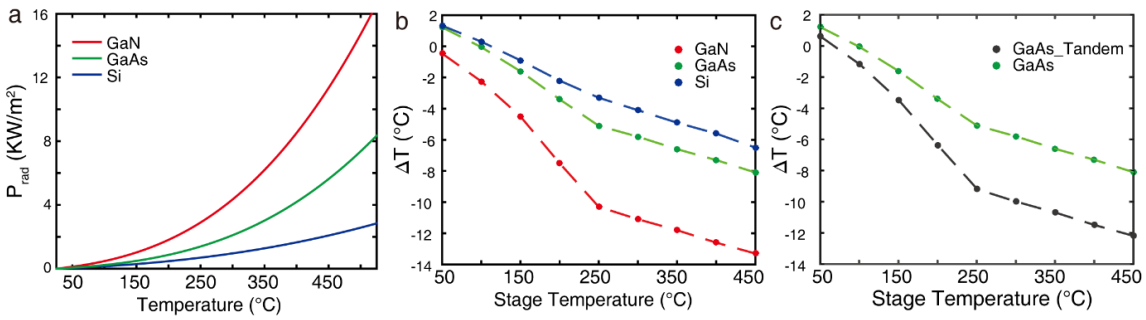

Figure 7.4**. a.** Net thermal radiation power density P_{rad} for GaN, GaAs, Si calculated from experimentally measured thermal emissivity. **b.** Calculated temperature difference between InGaN solar cell sample and heating stage temperature at different heating stage temperatures. The temperature difference of GaAs and Si are also plotted for reference. **c.** Calculated temperature difference between GaN-GaAs tandem cell sample and heating stage temperature at different heating stage temperatures. The temperature difference of GaAs is also plotted for reference. It clearly shows that with III-nitride as the top cell, the operating temperature of the underlying GaAs cell reduces effectively.

High-Temperature Performance of the 4T Mechanically Stacked InGaN-GaAs Tandem Cells.

To evaluate the possibility of III-nitride/III-V tandem solar cells, we investigated the PV performance of a mechanically-stacked four-terminal (4T) InGaN/GaAs tandem cell. Compared with the conventional two-terminal solar cell design, 4T tandem cells are able to avoid the current-matching constraint by comprising electrically independent subcells[187]. The 4T scheme has been demonstrated on multiple scenarios, including III–V-on-silicon[188], III–V-on-III–V[189], and perovskite-on-silicon devices[190], [191], which have exhibited promising efficiencies. Nevertheless, very few reports on 4T InGaN-GaAs tandem cell exist.

To investigate the potential of InGaN as the top cell for other III-V cells, we explored PV performance on the 4T scheme with the aforementioned nonpolar InGaN cell and high efficiency GaAs cells. As shown in Fig. 7.5(a), the InGaN cell was utilized as the UV filter and the GaAs cell was the rear subcell. At short wavelengths (i.e., < 500 nm), the majority of the incoming light is absorbed by the top InGaN cell. Figure 7.5(b) shows the EQE spectra of the InGaN and the filtered GaAs solar cells. While at long wavelengths (i.e., > 500 nm), about 60–65% of the incoming light is transmitted to the GaAs rear cell [shown in Fig.S10 (d)]. Most of the light loss is due to the reflection from the InGaN subcell, which offers a pathway to optimize the 4T device performance. In addition, we employ the recently proposed empirical construct of spectral efficiency to access the potential impact of the InGaN cell. It is defined as the power conversion efficiency of a solar cell resolved by wavelength and more details can be found in reference[192]. The external spectral efficiency of the InGaN and the filtered GaAs cells under various temperatures (25°C,

100°C, 200°C, 300°C and 400°C) were plotted in Fig. 7.5(b). As temperature increases, the shunt resistance becomes more dominant that negatively impacts the GaAs cell. Thus the external spectral efficiency of the GaAs cells dropped dramatically. This severe shunting effect is also similar to the previous report[163], which can be attributed to the oxidation of the material and degradation of metal contacts[166]. We assume that the degradation of PV performance of rear cells due to elevated temperature could be mitigated through the systematic design of InGaN top cells that arises from the self-cooling nature of III-nitrides. It's worth noting that the external spectral efficiency of the InGaN cell improved up to 350°C and outperformed itself at 25°C.

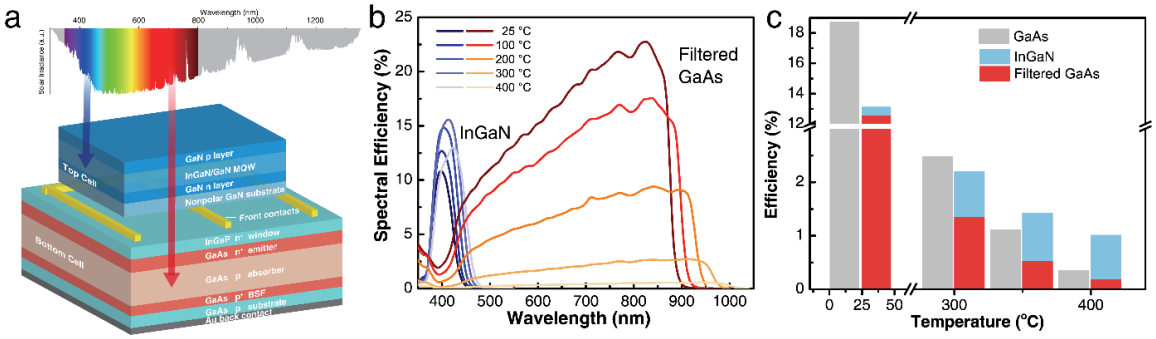

Figure 7.5**:** **(a)** The 4-terminal tandem schematic of the InGaN/GaAs cell, **(b)** the external spectral efficiency of the InGaN and the filtered GaAs cells under various temperatures, respectively and **(c)** column plots of the energy conversion efficiency under AM 1.5G of pristine GaAs cell (in grey), nonpolar InGaN top cell (in blue) and filtered GaAs cell (in red). The column combined with red and blue colors indicate the total efficiency of the 4T InGaN-GaAs cell.

Figure 7.5 (c) summarizes the conversion efficiency under AM 1.5G for the single GaAs cell, single nonpolar InGaN top cell, single GaAs cell with the filtering InGaN solar cell and 4T InGaN-GaAs tandem cell. At 300°C, the efficiency of the 4T InGaN-GaAs

tandem cell is approaching that of the single GaAs cell. Above 300°C, the 4T InGaN-GaAs tandem cell completely outperforms the single GaAs cell. At 400°C, the efficiency of the 4T tandem cell is about three times of that for the single GaAs cell. It's also noteworthy that InGaN cell could work efficiently even at 450°C while GaAs cell showed no PV performance after 400°C. This results show the great potential of InGaN top cell for tandem or MJ solar cell configurations for high temperature applications. Future device engineering, such as employing broadband anti-reflection coatings on InGaN top cell to reduce the light reflection, optimizing the luminescence coupling between the two junctions, and aligning electrodes of both cell to reduce reflection, could further enhance the device performance.

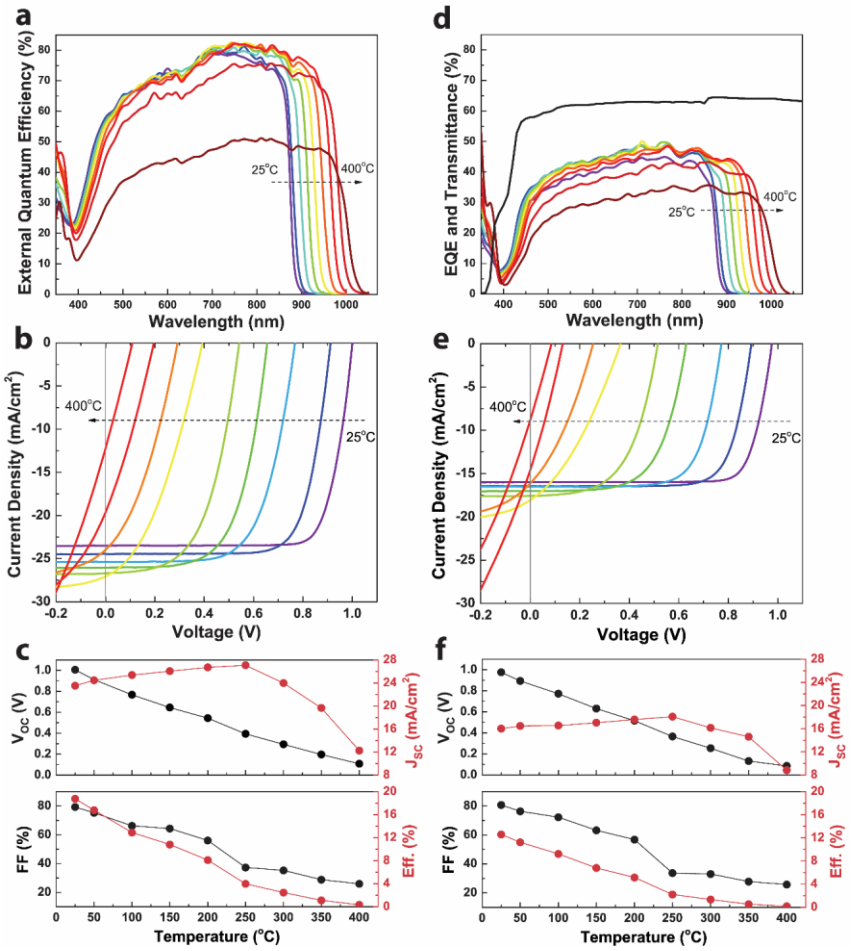

Figure 7.6**.** (a) The temperature-dependent EQE spectra, (b) LIV measurements and (c) the extracted V_{oc}, J_{sc}, FF and conversion efficiency values of the GaAs solar cell before the filtration and (d-f) show those results after the filtration of InGaN solar cell sample, respectively. The transmission spectra at room-temperature of the nonpolar InGaN MQW solar cell is also displayed in Fig.7.6 (d).

High-Temperature Performance of the 4T Mechanically Stacked InGaN-GaAs Tandem Cells.

The temperature-dependent EQE spectra, LJV measurements and the extracted V_{oc}, J_{sc}, FF and conversion efficiency values of the GaAs solar cell are shown in the Fig. 7.6 (**a-c)** before the filtration and in the Fig. 7.6 **(d-f)** after the filtration of InGaN solar cell sample, respectively. The transmission spectra at room-temperature of the nonpolar InGaN MQW solar cell is also presented in Fig. 7.6(b). At short wavelengths (i.e., < 500 nm), the majority of the incoming light is absorbed by the top InGaN subcell. At long wavelengths (i.e., > 500 nm), about 60–65% of the incoming light is transmitted to the bottom GaAs subcell. The rest of the incoming light is reflected from the top InGaN subcell, which can be further engineer to optimize the device performance. Moreover, as shown in the Fig. 7.6 (c) and 7.6 (f), both EQE spectra increase slightly up to 300°C and then drop dramatically. The peak EQE values also increase from ~79% to ~82% between 25°C and 300°C for pristine GaAs cell while ~45% to ~48% for filtered cell. This can be attributed to the decreasing bandgap energy of GaAs cell. After 350°C, the shunt resistance becomes the dominant factor that negatively impacts the GaAs cell and thus EQE drops quickly. This severe shunting effect is also similar to the previous report[163]. It can be attributed to the oxidation of the material and degradation of metal contacts[166]. Besides, Figure 7.6 (b)

and (e) show the temperature-dependent illuminated *JV* measurements of GaAs solar cell without and with the InGaN top cell, respectively. The extracted V_{oc}, J_{sc}, FF and efficiency as functions of temperature for InGaN cell before and after filtration are presented in Fig. 7.6 (c) and S10 (f), respectively. For both circumstances, the V_{oc} is found to drop at a rate of ~2.38 mV/°C in the range of 25°C - 400°C at 1 sun intensity, which is consistent with previous reports[163], [166]. This V_{oc} degradation at elevated temperatures is believed to be the major factor affecting the PV performance of GaAs cells[166]. As for pristine GaAs cell, J_{sc} rises from 23.5 mA/cm^2 (25 °C) up to 27.1 mA/cm^2 (250 °C). This is slightly different from the trend observed in EQE and this discrepancy between J_{sc} and EQE may be attributed to the different tested cells, and/or degradation of metal contacts and/or the thermal stress effect on cells. The shunt resistance starts to reduce from 250 °C and leads to the complete shunting of the cell at 350 °C.

7.4 Summary

In conclusion, we demonstrated a high performance nonpolar InGaN MQW solar cell with great potential for high temperature PV applications (e.g., > 350°C). The single-junction nonpolar *m*-plane InGaN solar cell exhibited a large positive temperature coefficient for EQE and PV efficiency from RT to 350°C, which is distinct from any solar cells ever reported. A 70% efficiency enhancement was observed from RT to 350°C in this nonpolar InGaN cell. This superior thermal performance is also attributed to several factors: (i) improved material quality through the homo-epitaxial growth enabled by single-crystal substrates; (ii) enhanced radiative capability due to nonpolar crystal orientation, thus improved effective lifetime of the photogenerated carriers in the QWs; and (iii)

narrowed large energy bandgap at high temperatures, offering better matching with solar spectrum. Furthermore, thermal radiation heat dissipation analysis revealed a unique self-cooling effect of III-nitrides. Near-unity emissivity of GaN resulted in a significant reduction of the device temperature, which leads to the reduced V_{oc} loss in InGaN solar cells. The self-cooling III-nitride top cell could serve as a heat shield for the underlying subcell(s) by reducing their device temperatures in the tandem design. These results offer new insights and strategies for the design and fabrication of high efficiency high temperature PV solar cells using III-nitrides, which will open up exciting new applications such as in space applications, and potentially lead to transformative outcomes in solar cell efficiency and deployment.

CHAPTER 8

ANOMALOUS CARRIER LOCALIZATION AND CARRIER DYNAMICS IN NONPOLAR M-PLANE INGAN/GAN QUANTUM WELLS AT HIGH TEMPERATURES

8.1 Motivations and research background

Recent advances in III-nitrides are poised to radically alter the design and implementation of optoelectronics[95], [193]–[199] and electronics[200]–[202]. In recent years, there has been tremendous progress in realizing nonpolar III-nitrides light-emitting-diodes (LEDs)[203], [204] and laser diodes (LDs)[205], [206]. In addition, novel devices and applications based on nonpolar III-nitrides are now emerging. Nonpolar InGaN solar cells exhibit improved carrier collection efficiency compared to *c*-plane counterparts[61] and deliver increased carrier lifetime and enhanced performance at elevated temperatures[58]. Another notable recent example is the vertical *m*-plane GaN *p*-*n* diodes that potentially leads to advanced vertical selective-area-doped power devices[207], [208].

This ongoing interest in nonpolar III-nitrides structures has been driven by their favorable properties, such as elimination of detrimental polarization-related effects, enhanced radiative recombination and high degree of polarized luminescence [209], [210]. Conventional polar *c*-plane III-nitride quantum wells (QWs) based emitters are currently constrained by the strong polarization-induced electric fields, inducing the tilted energy band profile and compromised radiative efficiency. To address this challenge, nonpolar crystal orientation of III-nitrides has been intensively researched for light-emitting applications. Several studies proposed that thick QWs and large active region in nonpolar structures can be employed to further exploit the advantage of high overlap of electron and

hole wavefunction in nonpolar QWs[180], [194], [211]. Others pointed out that excitonic recombination is dominant in nonpolar InGaN QW at room temperature while radiative lifetime in polar QW depends on the injected carrier density[180], [212], [213]. Theoretical studies also revealed that in nonpolar InGaN QWs, localization of holes originates from indium alloy fluctuation while electrons are tightly bound to holes via coulomb interaction[214], [215]. Furthermore, strong localization effects in hole wavefunction, rather than the electron wavefunction, explicitly accounts for the inhomogeneous broadening of emission energy of QWs. This difference is attributed to the small localization length of holes compared to electrons[215], [216].

Despite the rapid progress in the field, there are significant challenges that remain before the realization of full potential of nonpolar III-nitrides. Therefore, it's imperative to investigate carrier dynamics inside nonpolar QWs at both cryogenic and elevated temperatures. Numerous studies of carrier localization effect at cryogenic temperatures have been reported[212], [213], [215], [217]–[219], but very few reports exist on the analysis of carrier dynamics above room temperatures. In this study, we have experimentally and theoretically investigated the carrier localization and its impact on carrier dynamics on nonpolar *m*-plane InGaN/GaN QWs at elevated temperatures. Photophysical characterizations combined with high-resolution scanning transmission electron microscopy (STEM) and theoretical modeling suggest that the lack of integrity and uniformity in QWs significantly impact carrier confinement and localization, thus making carriers more prone to nonradiative recombination. In addition, analysis on exciton-phonon scattering mechanisms reveals that both acoustic and optical phonon scatterings dominate in the temperature range of 300-600 K. These detailed results and

analysis provide substantial understanding toward improving the optoelectronic performance of III-nitrides.

8.2 Experimental details

Growth and structure parameters of nonpolar InGaN/GaN MQWs.

Two InGaN/GaN MQW on nonpolar *m*-plane substrates were grown by conventional metal-organic chemical vapor deposition (MOCVD). The freestanding nominally on-axis bulk *m*- plane GaN substrates with low defect density (~$10^6$$cm^{-2}$) were provided from commercial vendors. The growth condition was designed to achieve the Indium incorporation around 12-14% in samples. The designed device consists of 1 μm Si-doped n-GaN ([Si]=5×10^{18} cm^{-3}), 10 nm highly Si-doped n^+-GaN ([Si]=1×10^{19} cm^{-3}), 20 periods of InGaN (nominal 3 or 6 nm)/GaN (10 nm) MQWs, 30 nm Mg-doped smooth p^+-GaN ([Mg]=1×10^{19} cm^{-3}), 120 nm Mg-doped p-GaN ([Mg]=3×10^{19} cm^{-3}), and 10 nm highly Mg-doped p^+-GaN contact layer ([Mg]=1×10^{20} cm^{-3}).

FIB and STEM imaging.

The nonpolar InGaN/GaN specimens for STEM imaging were prepared with an FEI Nova 200 Dual-Beam FIB system with a Ga ion source. A JEOL-ARM200F scanning transmission electron microscopy (STEM) operated at 200 KV and equipped with double aberration-correctors for both probe-forming and imaging lenses was used to perform high-angle annular-dark field (HAADF) imaging.

Temperature-dependent photoluminescence and time-resolved photoluminescence measurements

PL and TRPL measurements were done using a home-built system, where a picosecond 405nm pulsed laser diode (PDL 800-B) was used as excitation source. PL spectrum was

collected by a Si array detector coupled with Horiba monochromator (TRIAX 320). TRPL was measured by a time-correlated single-photon counting system (TCSPC). A Si photomultiplier tube (PMT) detector is attached at the other output port of monochromator and its signal is then recorded by TCSPC board (SPC130 module).

A Linkam HFS600-PB4 stage capable of heating the samples up to 600 °C was used to perform the temperature-dependent measurements. For both PL and TRPL measurements, the temperature of the stage was increased from room temperature to 400 °C in steps of 25 – 50 °C with a ramp rate of 10-20 °C/min. Once the desired temperature was reached, the sample was kept at the specified temperature for another 5 min.

Streak camera spectroscopy measurement

The Picosecond–microsecond time-resolved fluorescence Spectrometer, Streak Camera System consists of a femtosecond Titanium:Sapphire laser system operated at both MHz and KHz repetition rates (Coherent). The MHz system is a broadband Ti:S oscillator coupled with a pulse selector and a second harmonic generator, covers a wavelength region from 700 – 1000 nm and 350 – 500 nm and a repetition rate from single shot (1 Hz) to 76 MHz. The KHz system uses the MHz oscillator as a seed laser to pump a regenerative amplifier and an OPA operated between 100 – 250 KHz. The output wavelength covers from 250 – 750 nm. The detecting system consists of a spectrograph, a streak camera with fast and a slow time sweep unit. The system is designed to record fluorescence signal as a function of time and wavelength with a time resolution of 5 ps and wavelength region from 320 – 950 nm.

Simulation of band diagrams

The energy band diagrams of InGaN/GaN double heterostructures were simulated using Silvaco ATLAS software. They contain 3- or 6-nm absorbing layer and 10-nm barrier. The band structure parameters, the conduction and valence band offsets of InGaN/GaN DHs were obtained from Huang *et al*[61], respectively. Silvaco ATLAS is a commercial device simulation tool based on the drift-diffusion model. MQW simulation is based on a parabolic quantum well model implemented within Silvaco ATLAS. The bound state energies are calculated solving the Schrödinger equation along discrete slices in the quantization direction.

8.3 Results and discussions

Figure 8.1 present the cross-sectional high-angle annular dark-field (HAADF) images of two nonpolar *m*-plane InGaN/GaN MQW samples taken along $[11\bar{2}0]$ zone axis, which are denoted as *m*6 and *m*3, respectively. The sharper and better-defined interfaces of QWs of sample *m*6 can be observed in Fig. 8.1(a) and (b) compared to those of *m*3 in Fig. 8.1(c) and (d). The QW interfaces are also spatially resolved for *m*6 in the intensity profile mapping in the supplementary Fig. 8.S1(c) due to the Z-contrast nature of STEM-HAADF images. On the contrary in Fig. 8.S1 (f) and (g), long Indium distribution tail in GaN barrier layers (upper interfaces) can be observed, which resembles the graded InGaN/GaN QWs. From Fig. 8.S1(a) and (e), the average thicknesses of one period of InGaN QW and GaN barrier are approximately 18 nm for *m*6 and 15 nm for *m*3, respectively. We can therefore conclude that structural uniformity is better preserved in sample *m*6 rather than *m*3. Consequently, the potential fluctuation in *m*6 are most likely to be induced from QW

thickness fluctuation as evidenced in Figure 8.S1(a-d), while the indium compositional fluctuation mainly accounts for potential fluctuation in *m*3, assuming similar random alloy disorder and strain in both samples. In addition, it's also worth noting that the interface of InGaN/GaN layers [upper interfaces, see Fig. 8.1(b) and (d)] is generally sharper than that of GaN/InGaN layers [lower interfaces, see Fig. 8.1(a) and (c)]. This phenomenon has also been observed in previous reports on InGaN/GaN QWs[215], [220], [221], and is typically known as compositional pulling effect[222].

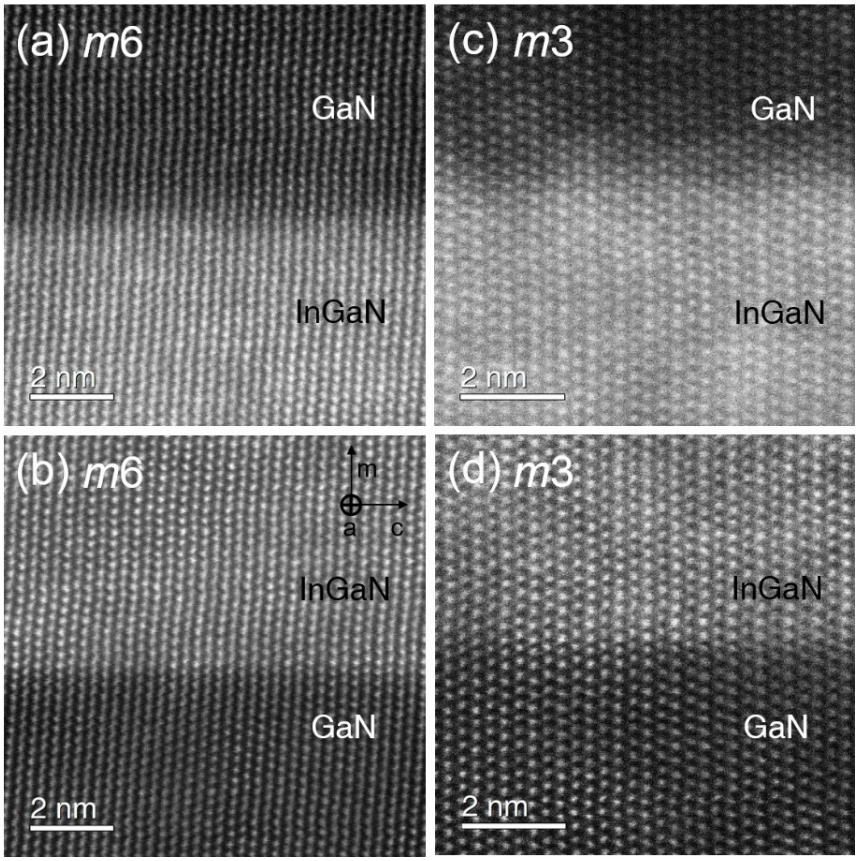

Figure 8.1: STEM-HAADF images of interfaces of InGaN/GaN QWs in the atomic-scale for (a-b) sample *m*6 and (c-d) *m*3, respectively. (a) and (c) explicitly display the upper GaN/InGaN interfaces while (b) and (d) for lower InGaN/GaN interfaces. Both upper and lower interfaces of InGaN/GaN QWs of *m*6 are much sharper than those of *m*3.

The excitation power-dependent PL and TRPL measurements have been widely adopted to investigate the underlying recombination process and the corresponding carrier dynamics in III-nitride emitters[223], [224], [212]. Figure 8.2 illustrate the (a) integrated PL intensity and (b) effective carrier lifetime extracted from TRPL at room temperature as a function of excitation laser power for sample *m*6 (blue) and *m*3 (purple), respectively. The decay curves of power-dependent time-resolved photoluminescence (TRPL) are shown in Figure 8.S3. Generally, the integrated PL intensity (I) is proportional to the excitation power (P) , i.e., optically injected carrier density, and can be given by $I \propto P^n$, where *n* is an indicator of radiative or nonradiative recombination mechanism. In Fig. 8.3 (a), the values of *n* for both *m*6 and *m*3 are approaching 1.18 which is larger than 1, suggesting the co-existing radiative and Shockley–Read–Hall recombination in both samples in the range of excitation power employed in our study. Nonetheless, 2 samples exhibit distinct carrier dynamics under laser excitation, even though they share similar effective lifetime at weak excitation. In Fig. 8.2 (b), the effective lifetime in *m*6 keeps reducing until excitation power around 10 μW and remains almost constant afterwards. This tendency of unchanged carrier lifetime has been reported previously on both nonpolar *m*-plane[220] and polar *c*-plane[223] InGaN/GaN QWs. We attribute this decreasing lifetime of *m*6 to band filling effect of localized centers and higher energy levels rather than the Coulomb screening of the internal electric field in QWs, due to the elimination of internal intrinsic electric filed in *m*-plane QWs. Regarding the saturation of the effective lifetime after ~10 μW, it can be ascribed to the fully occupied higher energy levels and a wholly excitonic recombination mechanism, which has been previously reported[180]. In comparison, the effective lifetime in *m*3 tends to increase up to excitation power around 10

μW and then the rising rate slows down. This can be accounted by the gradual quenching of nonradiative recombination centers with more optically injected carriers. Overall, 2 samples exhibit drastically different behavior of carrier lifetime even though sharing similar lifetime under low excitation condition.

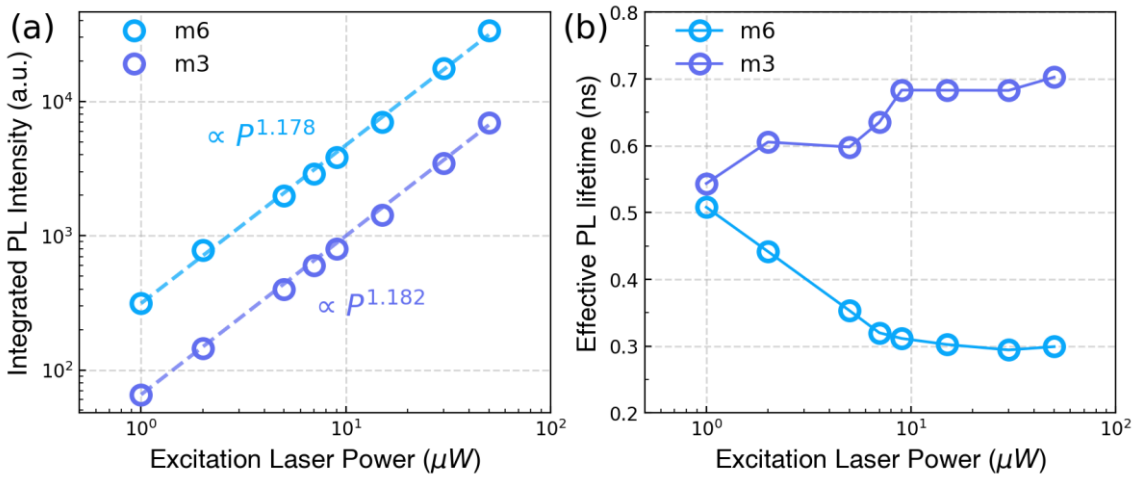

Figure 8.2: (a) Integrated PL intensity and (b) effective carrier lifetime extracted from TRPL measured at room temperature as a function of excitation laser power for *m*6 (blue) and *m*3 (purple), respectively.

To gain more insights into the impact of structural uniformity and carrier localization on carrier dynamics, we have carried out temperature-dependent time-resolved photoluminescence (TRPL) measurements. They are measured at 3 different excitation powers of 1 μW, 5 μW and 50 μW, which correspond to an estimated excited carrier density of 3×10^{12}cm^{-3}, 1×10^{13}cm^{-3} and 1×10^{14}cm^{-3}, respectively. The PL effective lifetime τ_{eff} under each temperature and excitation power was extracted from each PL decay curve with the fast decay in a biexponential decay function, which is also shown in Figure 8.S4. The temperature-dependent time-resolved TRPL measurements of sample m6 and m3 in range of 20–400 °C and at three different excitation power (1, 5 and 50 μW) are shown in the

supplementary Figure 8.S3. In Fig. 8.3 (a), τ_{eff} in sample *m*3 tends to increase and then reduce after 150 °C(~420K). In contrast, τ_{eff} in sample *m*6 in Fig. 8.3 (b) remains almost constant till 200 °C (~470K) and then rises.

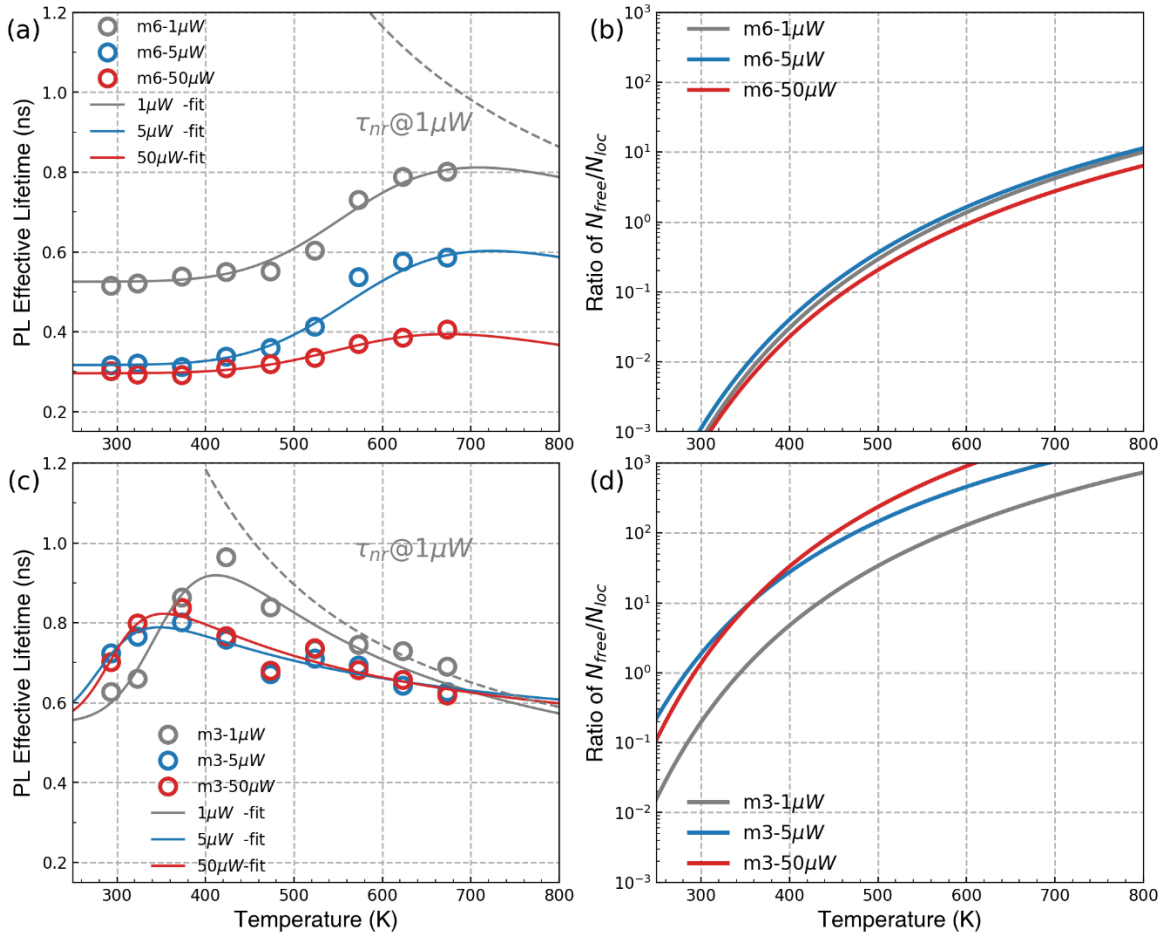

Figure 8.3. Comparison of carrier dynamics of two *m*-plane InGaN/GaN QW samples. Measured QW effective lifetime (circles) for (a) m6 and (c) m3 at three different excitation powers. Solid lines represent the simulated effective lifetime and the grey dash lines indicate theoretical simulated nonradiative lifetime (τ_{nr}) at 1 μW of laser power. Figure 3(b) and (d) show the ratio of density of free exciton versus localized exciton (n_{free}/n_{loc}) deduced from the model for (b) m6 and (d) m3, respectively. In all figures three different

excitation powers are plotted with 3 individual colors: grey for 1 μW, blue for 5 μW and red for 50 μW.

The temperature-dependent τ_{eff} of each sample was simulated with a theoretical lifetime model that accounts for carrier localization effect[220], [225]. This model assumes that the densities of both free and localized excitons keep in thermal equilibrium. Thus, the effective decay lifetime (τ_{eff}) of excitons in the QW is given by

$$\frac{1}{\tau_{eff}} = \left(\frac{n_{loc}}{\tau_{loc}} + \frac{n_{free}}{\tau_{free}}\right)/(\tau_{loc} + \tau_{free}), \tag{8.1}$$

where n_{loc} and n_{free} are localized and free exciton densities, respectively while τ_{free} and τ_{loc} represent characteristic decay time for localized and free excitons. The ratio between n_{loc} and n_{free} is then give via Saha's law[225] by

$$\frac{n_{free}}{n_{loc}} = \frac{2M_X k_B T}{\pi\hbar^2 N_D} \cdot e^{-E_{loc}/k_B T}, \tag{8.2}$$

where M_X is the exciton mass, E_{loc} is the localization energy, and N_D is the localization center density in QWs. The τ_{loc} is considered as temperature-independent due to the fact that it only depends on the coherence volume of localized excitons[226]. In addition, the effective decay lifetime of free exciton (τ_{free}) constitutes of both radiative (τ_r) and nonradiative lifetimes (τ_{nr}):

$$\frac{1}{\tau_{free}} = \frac{1}{\tau_r} + \frac{1}{\tau_{nr}}, \tag{8.3}$$

The radiative lifetime of free exciton (τ_r) increases linearly with temperature[227] and is given by

$$\tau_r = \frac{6M_X k_B T}{\hbar^2 k_\parallel^2}\tau_0, \tag{8.4}$$

where τ_0 represents radiative lifetime of free excitons at $k_\parallel = 0$, $k_\parallel$ is the in-plane wave vector of free excitons within the light cone. The value of τ_0 was taken as 10 ps in the

simulation[220]. On the other hand, a nonradiative recombination process with a characteristic activation energy E_A is also taken into account:

$$\tau_{nr} = \tau_{nr0} \cdot e^{-E_A/k_B T}, \tag{8.5}$$

where τ_{nr0} is the indication of interaction between excitons and nonradiative recombination centers. Therefore, there are five main parameters for fitting: τ_{loc}, E_{loc}, N_D, τ_{nr0} and E_A. During the fitting procedure, τ_{loc} has been set to match the lifetime around room temperature (~300 K). E_{loc} and N_D have been optimized to fit the increasing range of effective lifetime. τ_{nr0} and E_A have been tuned to account for the reduction of the effective lifetime (> 650 K for m6 and > 400 K for m3).

The solid lines in Fig.8.3(a) and (c) exhibit the fitting results for 2 samples under 3 excitation power. All fitting parameters are tabulated in Table I. The grey dashed lines in Fig. 8.3(a) and (c) represent the nonradiative recombination lifetime at the excitation power of 1 μW, which are plotted for better illustrative purpose. The localization center density N_D is around 2×10^{10}cm^{-2} for *m*6 while approximately 1×10^{8}cm^{-2} for *m*3. This parameter obtained from previous reports under cryogenic temperatures is in the range of 10^{10} and 10^{11}cm^{-2} cm in AlGaAs/GaAs QW where exciton localization is induced from monolayer variation of well width[228]. Moreover, it's approximately 1×10^{12}cm^{-2} in *m*-plane InGaN/GaN MQW[220], which is within the scale of Indium fluctuation observed from atom probe tomography study[229]. In comparison, localization center density N_D obtained in our study is at least 2 orders of magnitude lower than the previous reports, which can be treated as deep localization centers in MQWs. This significant difference can be accounted for by the measurement temperature range, thus providing substantial insights into

approaches to evaluate emission properties of III-nitride MQW above ambient temperatures in addition to cryogenic studies.

Furthermore, we can also obtain the E_{loc} of ~0.34eV for *m*6 and ~0.30 eV for *m*3. It's worth noting that they are roughly close to the value of conduction band offsets in each sample, as shown in Figure 8.S2. We therefore posit that under high temperatures, the major transport mechanism for electron is delocalization via thermal escape from QWs to barriers and then recombine nonradiatively. This is possibly related to the large localization radius of electrons compared to holes[216].

Table 4. Parameters from fitting lifetime model for *m*6 and *m*3 at 3 excitation powers.

	τ_{nr0} (ns)	E_A (meV)	$N_D(\times 10^8 cm^{-2})$	E_{loc} (meV)	τ_{loc} (ns)
$m6-1\ \mu W$	0.351	62.0	2.73×10^2	352	0.525*
$m6-5\ \mu W$	0.218	75.6	2.80×10^2	342	0.316*
$m6-50\ \mu W$	0.126	77.5	5.04×10^2	341	0.296*
$m3-1\ \mu W$	0.293	48.2	7.90	300*	0.55*
$m3-5\ \mu W$	0.439	23.6	1.10	300*	0.55*
$m3-50\ \mu W$	0.433	24.2	1.13	300*	0.55*

*The numbers with asterisks (*) mean that they are fixed in the fitting.

Moreover, the ratio of free and localized carrier densities can be also estimated from this model and plotted in Fig. 8.3(b) and (d). For *m*6, n_{loc} and n_{free} become equal in the range of 550 to 600K, which corresponds to the temperature where FWHM of PL peaks increases significantly as shown in Fig. 8.6. In contrast for *m*3, free excitons become

dominant at around 300K, especially under high excitation conditions. By taking into account of the STEM studies in Fig.1 and results of excitation-dependent carrier lifetime as shown in Fig. 8.2(b), we can then propose that the fundamental difference in carrier dynamics of both samples lies in disparate potential confinement of carriers. For *m*3, the significant Indium fluctuation across barrier layers contributes to obscure interface between QWs and barriers, diminishing carrier confinement in QWs. This effect further populates carriers more spatially in both QW and barrier regions and more energetically into higher energy levels, which in turn make carriers susceptible to nonradiative centers. Therefore, this accounts for larger n_{free}/n_{loc} ratio and the decreasing lifetime after 400K observed in *m*3. In comparison, *m*6 acquires explicit and uniform QW/barrier interface and hence better carrier confinement. Therefore carriers stay at localization centers and are able to maintain strong radiative capability, especially considering exciton radius is much smaller than the QW width[230].

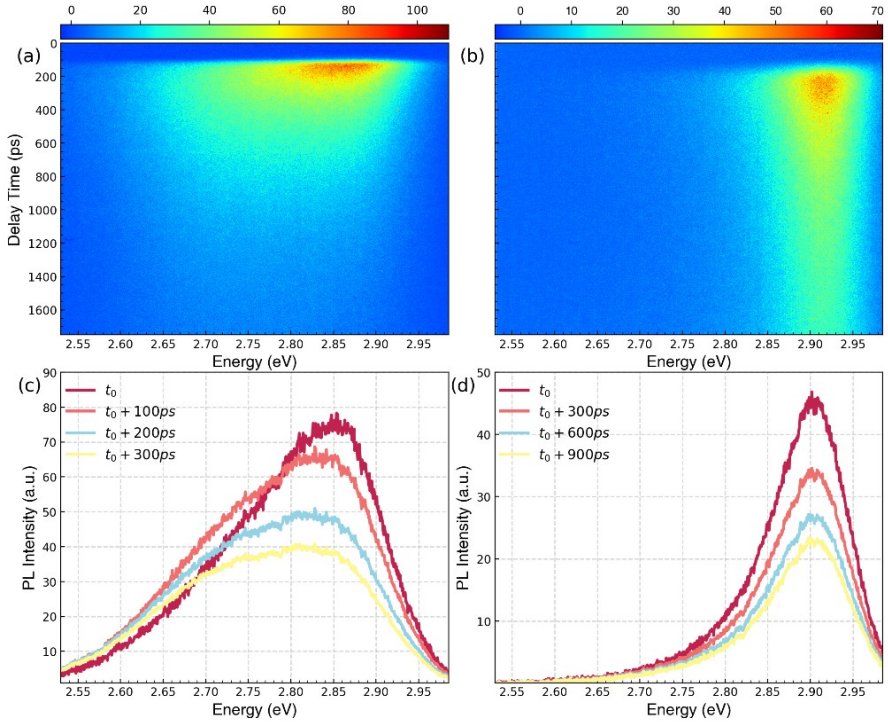

Figure 8.4: Streak camera spectroscopy images of sample (a) *m*6 and (b) *m*3 recorded at room temperature. The resonant laser excitation of 400 nm was used. Transient PL spectra after laser excitation of the sample (c) *m*6 and (d) *m*3, with an interval of 0.1 ns and 0.3 ns for each curve, are displayed for *m*6 and *m*3, respectively.

Figure 8.4(a) and 8.4(b) present the streak camera spectroscopy images for two *m*-plane samples recorded at RT under identical high excitation power. We observe a much broader emission spectrum of MQW of *m*6 in Fig. 8.4(a) compared to that of *m*3 in Fig. 8.4(b) at early delays. Then the emission spectra of MQW progressively diminish with increasing time delays in the vicinity of 2.85 eV for m6 and 2.90 eV for *m*3.

To further elucidate the evolution of carrier dynamics of both samples, Figure 8.4(c) and 8.4(d) show the time-resolved spectra extracted from streak images at 4 different time delays. A time interval of 100 ps is chosen for *m*6 and 300 ps for *m*3. The broad and asymmetric emission from MQW at early delays of both samples can be attributed to the phase space filling effect. In addition, a progressive carrier cooling process of exciton is evidenced by the gradual declining slope of the high-energy tail. Moreover, the slight redshift of the peak energy of *m*6 is observed in Fig. 8.4(c) while it remains almost constant for *m*3. This suggests that only partial localization centers have been saturated under such excitation, which is also consistent with higher localization carrier density estimated from Figure 8.3 and the larger FWHM value of m6 at RT in Figure 8.5. It's also worth noting that there exists a carrier redistribution process in the range of 2.70 to 2.90 eV for *m*6 [see Fig. 8.4(a) and (c)], which is not observed in *m*3. For *m*6 in the early decay, emission from lower energy centers first rises rapidly (from t_0 to t_0+100ps) and then reduces which resembles the evolution of the emission from the extended states. This result serves as a

strong indicator of carrier localization effect in *m*6 and also reinforces our previous arguments for the temperature-dependent carrier dynamics in Fig. 8.3(a-b). This carrier redistribution has also been observed in other nonpolar InGaN QW[217].On the other hand for *m*3, no sign of carrier redistribution indicates that photoexcited carriers populate into higher energy states and tend to follow a global Fermi distribution and carrier localization is smaller than in *m*6.

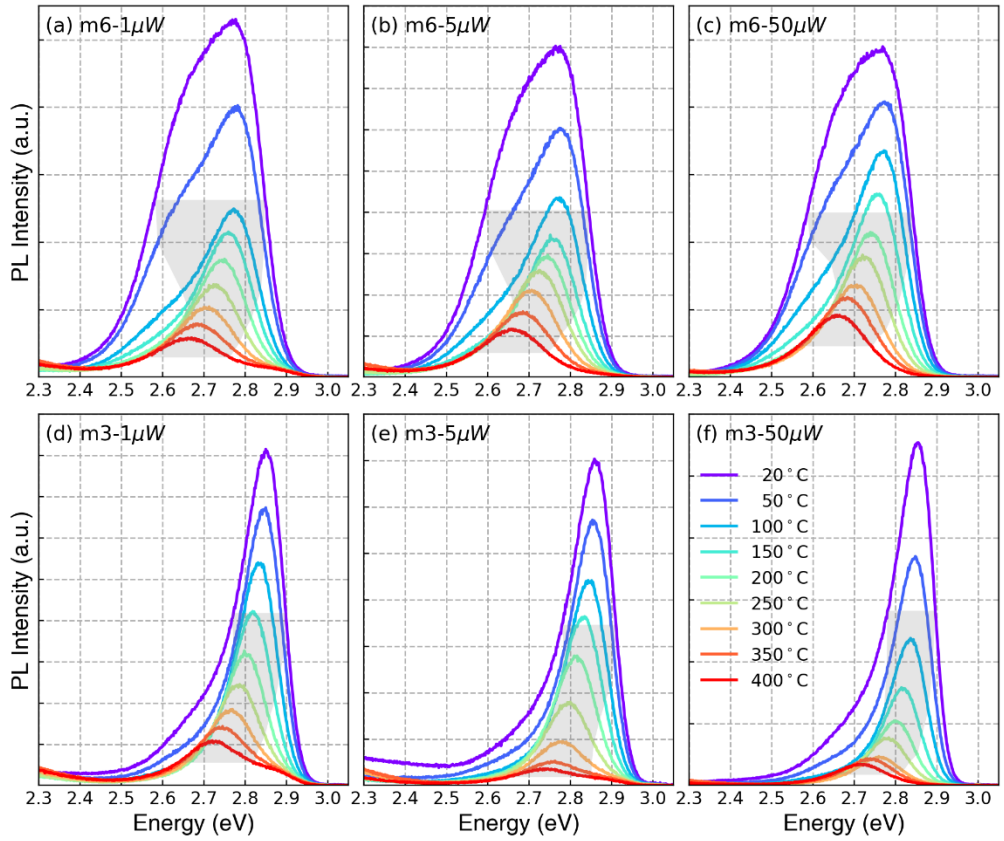

Figure 8.5: Temperature-dependent PL emission spectra of the sample (a-c) *m*6 and (d-f) *m*3 in range of 20–400°C and under three different excitation power (1, 5 and 50 μW). All data are not normalized. The shaded area indicates the evolution of FWHM of both samples.

Figure 8.5 shows the temperature-dependent PL emission spectra of the sample (a-c) m6 and (d-f) m3 in a range of 20–400 °C and under three different excitation power (1,

5 and 50 μW). The common feature of both samples is the redshifting of peak energy with rising temperature which is attributed to thermal narrowing of bandgap energy. We can also observe strong emission from lower energy centers which is comparable to that from the band-to-band recombination from the extended states. This can possibly be attributed to the localization centers induced from thickness fluctuation of QW which is also evidenced in Figure 1 and S1. Previous reports also discovered that this broad emission is related to the surface morphology with pyramidal hillocks in on-axis *m*-plane QW[211], [231]. In addition, the shaded grey areas in each subplot represent the evolution of FWHM values. For *m*6, it first reduces gradually with temperature up to 150°C and then starts to increase. In contrast, the FWHM of *m*3 tends to rise from 50°C. It's worth noting that the narrowing FWHM of PL indicates the exciton/carrier delocalization with enhanced thermal energy. This also corresponds to the carrier redistribution dynamic observed in *m*6 in Fig. 8.4(c).

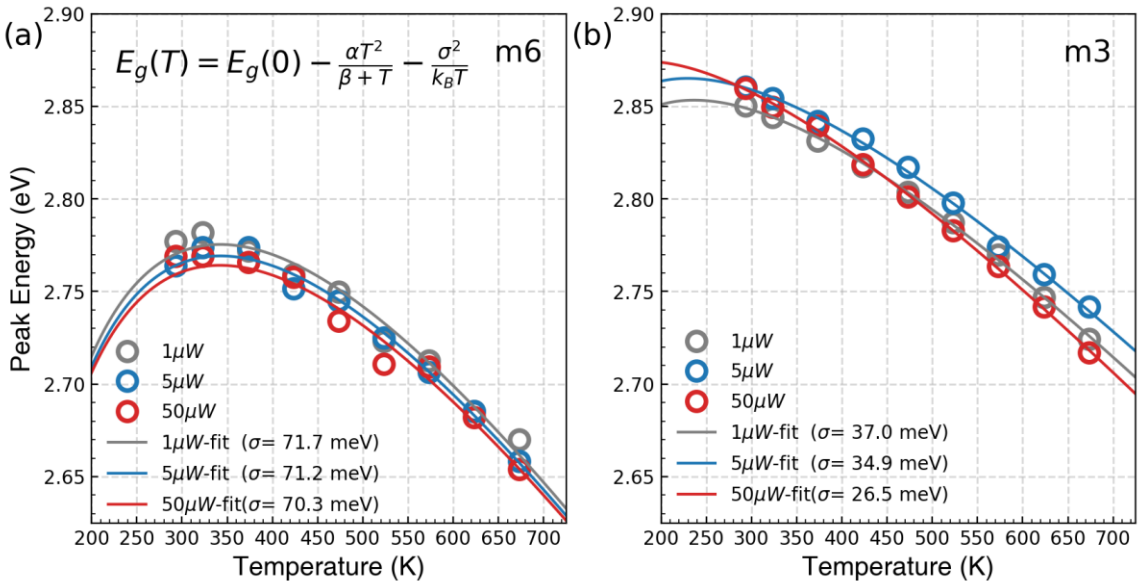

Figure 8.6: PL emission peak energy as a function of temperature for (a) m6 and (b) m3 at three different excitation powers (1 μW for grey, 5 μW for blue and 50 μW for red).

To further investigate the underlying physical mechanisms in the temperature-dependent PL emission, we have also extracted both the peak energy and PL FWHM values and fitted them with related models. Figure 6 present the temperature dependence of PL peak energy for two samples at three different excitation powers which are shown as hollowed circles. The fitted data from the model are displayed with lines. To further elucidate the degree of exciton/carrier localization, we have applied a modified Varshni empirical model [232]–[234] to fit the data:

$$E_g(T) = E_g(0) - \frac{\alpha T^2}{\beta + T} - \frac{\sigma^2}{k_B T}, \quad (6)$$

where $E_g(0)$ the bandgap energy of InGaN at 0K, T is temperature in Kelvin, k_B is the Boltzmann constant, α and β are the Varshni fitting parameters and σ is a parameter indicative of the degree of exciton localization. A unified Debye temperature β = 630 K is used in the fitting procedure. All σ parameters are also summarized in Figure 8.6. We can observe that the degree of exciton localization (σ) in *m*6 is almost twice as large as the ones in *m*3, which is in good agreement with the experimental results from Figure 3 to 5. The difference in σ suggests that the exciton localization existed in both samples arise from different physical origins, which is also evidenced in STEM analysis in Figure 8.1. In addition compared with the fitted σ values from previous reports, σ values of *m*3 are comparable to those from green polar InGaN MQW of ~ 30 meV[235], while *m*6 obtains a much higher σ, which also are close to those reported in green semipolar InGaN MQW[233].

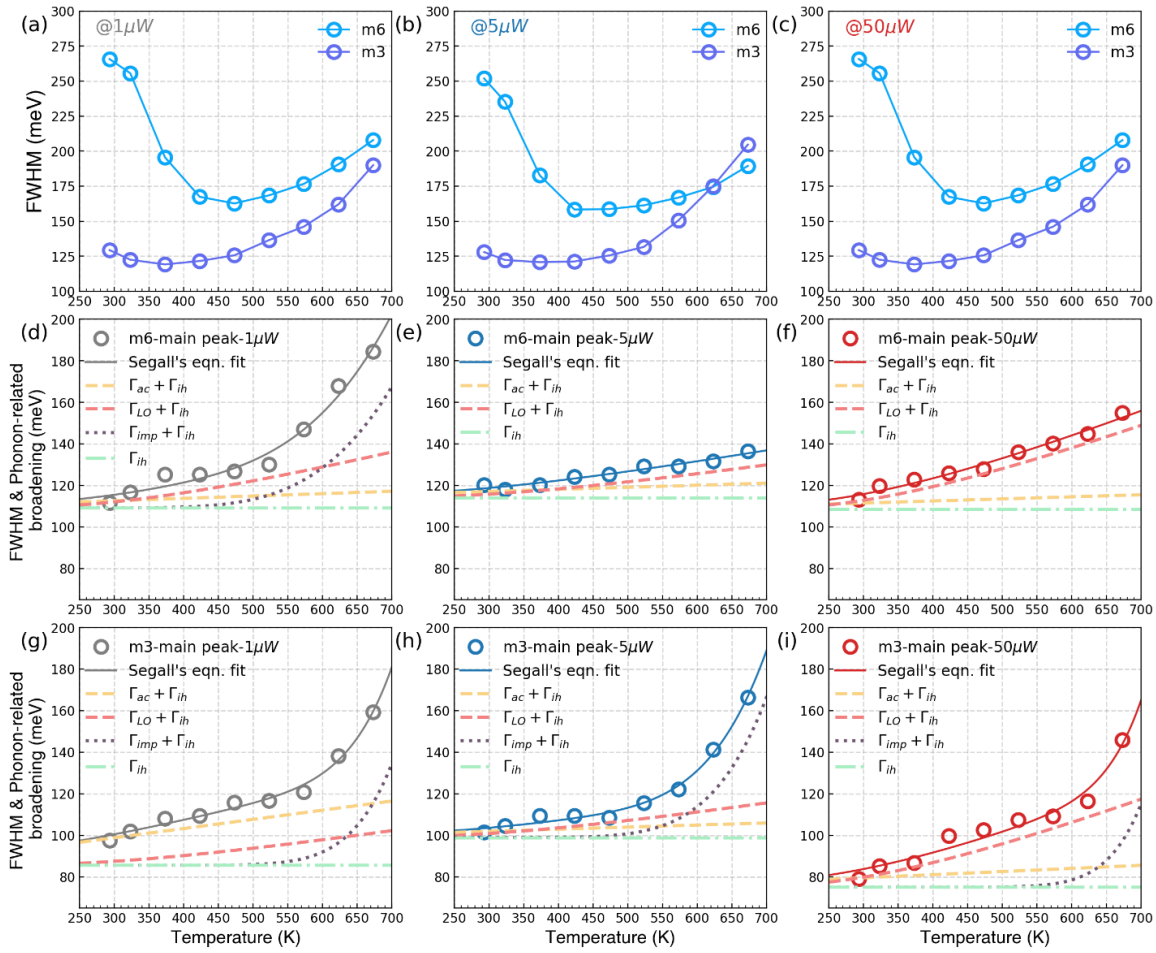

Figure 8.7. Temperature dependence of PL FWHM of 2 samples. FWHM of the steady-state PL spectra as a function of temperature for (a-c) *m*6 (in blue) and *m*3 (purple). In Fig.7(d-i), the hollow circles are the FWHM values of the main peaks in sample *m*6 and *m*3 by fitting with multiple Gaussian peaks. Grey, blue and red circles correspond to 1 μW, 5 μW and 50 μW. The solid lines in Fig. 8.7(d-i) are fitted using Segall's expression of $\Gamma(T) = \Gamma_{ih} + \Gamma_{LO} + \Gamma_{ac} + \Gamma_{impurity}$, which account for contributions from inhomogeneous broadening, Fröhlich coupling with LO and AC phonons and impurities. The broadening of PL linewidth with temperature arises from inhomogeneous broadening (Γ_{ih}, horizontal green dash-dot line), Fröhlich coupling between charge carriers and LO

phonons (Γ_{LO}, red dash line) and acoustic phonons (Γ_{ac}, orange dash line), and scattering from ionized impurities ($\Gamma_{impurity}$, brown dotted line).

To further elucidate exciton-phonon scattering mechanisms at elevated temperatures, we have extracted the full width at half maximum (FWHM) of temperature-dependent PL spectra of both samples and plotted them in Figure 8.7 (a-c). For *m*6, FWHM first reduces with temperature up to 150°C (~420K), which can be attributed to a more homogeneous redistribution of carriers with enhanced thermal energy from surrounding potential minima. Afterwards FWHM tends to rise and the increase is related to both phonon- and impurity-induced broadening mechanisms. In comparison, *m3* exhibits similar rising tendency with temperature above 100°C except the slight decrease near the room temperature.

Considering that the PL spectrum is convoluted with the emission from both radiative band-to-band recombination and localization sites, we have applied multiple Gaussian functions to fit each spectrum and obtained FWHM from the main peak (extended states) with the strongest PL emission. The results are shown in Figure 8.7 (d-f) for *m*6 and Figure 8.7 (g-i) for *m*3, respectively. All extracted FWHM values have been fitted with Segall's equation. The overall broadening of FWHM with temperature can be described as the sum of three types of phonon-induced linewidth broadening mechanisms[236], [237] as well as the scattering from ionized impurities[238]–[240]:

$$\Gamma(T) = \Gamma_{ih} + \Gamma_{ac} + \Gamma_{LO} + \Gamma_{impurity}$$

$$\Gamma(T) = \Gamma_{ih} + \gamma_{ac}T + \frac{\gamma_{LO}}{\exp\left(E_{LO}/k_BT\right)-1} + \gamma_{im}\exp\left(\frac{-E_{imp}}{k_BT}\right), \quad (8.7)$$

where Γ_{ih} is the temperature-independent inhomogeneous broadening constant which stems from scattering due to exciton–exciton interactions, crystal disorder and imperfections[236]. In the second and third terms (Γ_{ac} and Γ_{LO}), γ_{ac} and γ_{LO} are the acoustic and longitudinal optical (LO) phonon coupling constants, respectively[237]. E_{LO} represents the characteristic energy of LO phonon which is set as 91 meV in the fitting procedure. The last term ($\Gamma_{impurity}$) accounts for the scattering from ionized impurities with an average activation energy E_{imp}. Generally, two major homogeneous broadening mechanisms (Γ_{ac} and Γ_{LO}) are scattering of deformation potential[241]. The interaction between exciton and acoustic phonon involves only intraband scattering of excitons[237] and is linearly dependent on temperature. In contrast, the interaction between exciton and LO phonon is typically described as Fröhlich interaction, which originates from Coulomb interaction between electrons and electric field induced by the out-of-phase displacements of oppositely charged atoms due to LO phonon. For polar semiconductors such as GaN, LO phonon dominates the scattering mechanism[232], [236].

Table 5. Parameters determined from fitting for the PL emission from the extended states for *m*6 and *m*3.

	Γ_0 (meV)	γ_{ac} $(\mu eV/k)$	γ_{LO} (meV)	E_{LO} (meV)	γ_{im} (eV)	E_{imp} (eV)
$m6-1\ \mu W$	109.2	11.4	95.0	91.3^{*}	44.4	0.400
$m6-5\ \mu W$	114.1	10.0	55.9	91.3^{*}	-	-
$m6-50\ \mu W$	108.5	10.0	143.2	91.3^{*}	-	-
$m3-1\ \mu W$	90.6	24.4	90.0	91.3^{*}	10000	0.739
$m3-5\ \mu W$	98.9	10.0	55.0	91.3^{*}	599.5	0.548
$m3-50\ \mu W$	75.0	15.0	139.8	91.3^{*}	10000	0.888

*The numbers with asterisks (*) mean that they are fixed in the fitting.

For $m6$, the contribution of impurity broadening ($\Gamma_{impurity}$) can only be observed under 1 μW excitation. Acoustic phonon broadening (Γ_{ac}) dominates under 5 μW while LO phonon broadening is the main broadening mechanism under 50 μW. From Figure 8.7(g) to 8.7(i), the broadening of FWHM of $m3$ is dominated mostly by both acoustic and LO phonon scattering prior to 600K. Under low excitation conditions including 1 μW and 5 μW, the crossover temperature where these two homogeneous broadening mechanisms contribute equally is approximately 400K. After 600K, impurity scattering ($\Gamma_{impurity}$) becomes dominant. Previous paper suggested that this activation energy could also provide an estimated localization depth of excited carriers dephasing into surrounding InGaN materials[239].

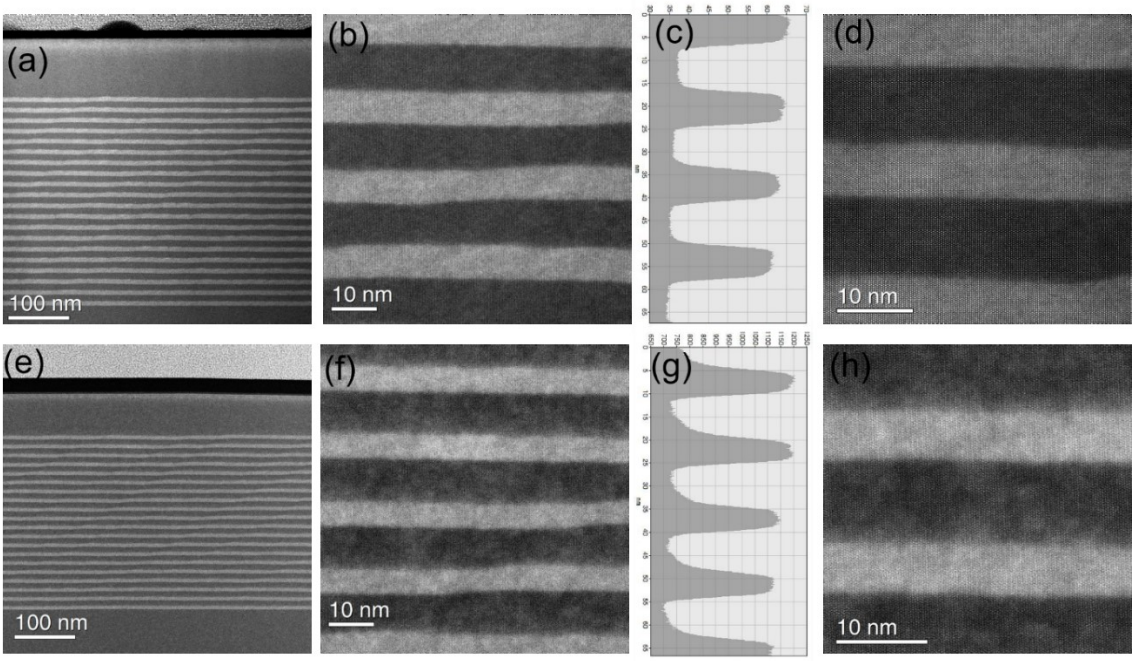

Figure 8.S1. The HAADF-STEM images of (a & e) the entire m-plane InGaN/GaN MQW structure, (b & f) the representative 5 periods of QW and barrier layers and (c & g) corresponding intensity profiles, and (d & h) the magnified images of 2 periods of QW and

barrier layers. Figures (a-d, the top row) were taken from *m*6 while (e-h, the bottom row) from *m*3.

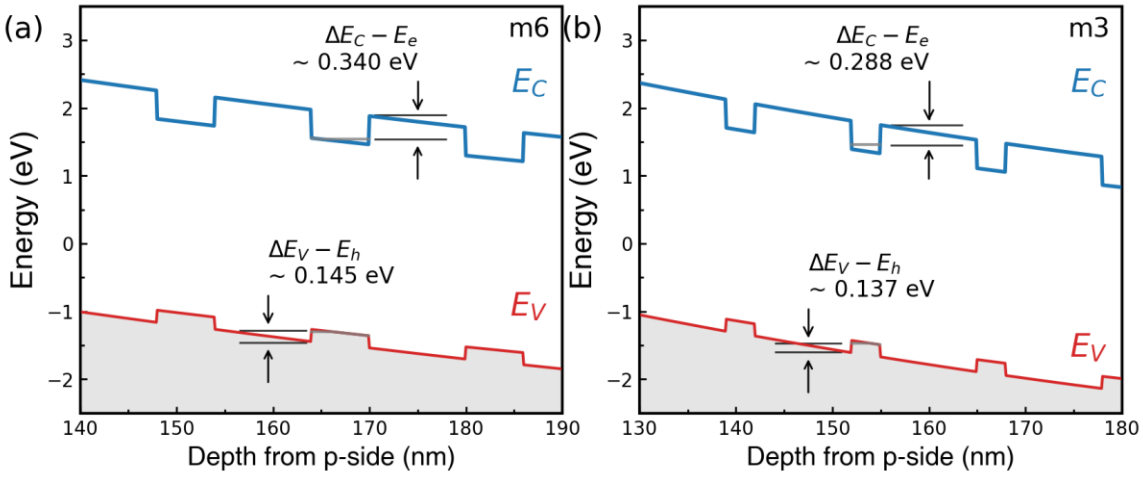

Figure 8.S2: Schematic zoom-in energy band diagrams of (a) *m*6 and (b) *m*3, respectively. The grey lines indicate the ground states of the fifth QW for electron and hole in conduction band and valence band, respectively.

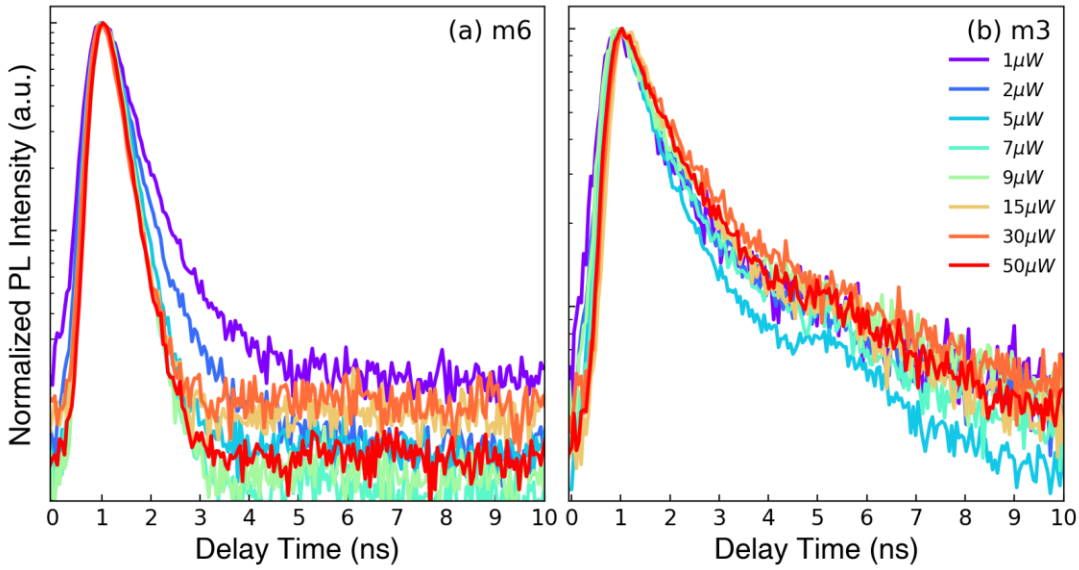

Figure 8.S3. Power-dependent time-resolved photoluminescence (TRPL) for (a) *m*6 and (b) *m*3, respectively, from 1μW to 50 μW.

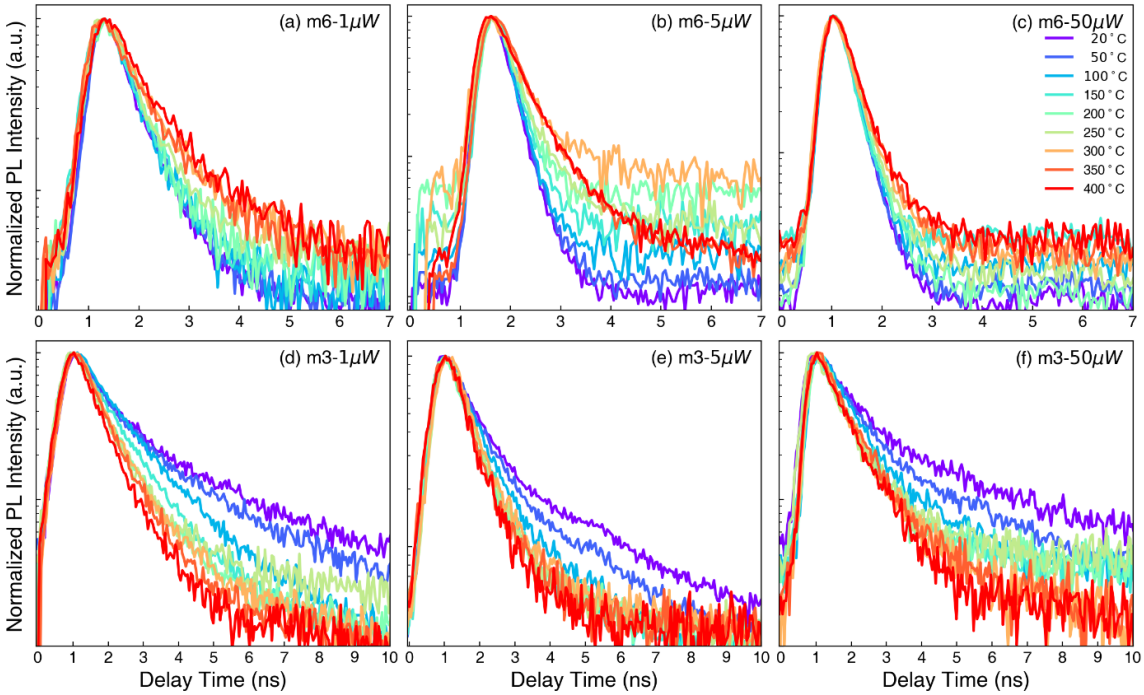

Figure 8.S4. Temperature-dependent time-resolved photoluminescence (TRPL) studies of sample (a-c) *m*6 and (d-f) *m*3 in range of 20–400 °C and at three different excitation power (1, 5 and 50 μW).

8.4 Summary

In conclusion, experimental investigations on two *m*-plane InGaN/GaN QWs demonstrate that in relatively thin QW structure, the obscure interfaces between QW and barriers and the lack of structural uniformity induced from Indium compositional fluctuation tend to delocalize carriers and make them more prone to the nonradiative Shockley-Reed-Hall recombination. Nonetheless in the case of thick QW design, carrier localization is more likely to originate from thickness fluctuation of QW and/or barrier which enables InGaN QWs maintain strong radiative capability even at elevated temperatures. It's therefore vital for device designers to carefully manage QW integrity and uniformity in pursuit of a

thicker *m*-plane InGaN active region. From the analysis of temperature-dependent carrier lifetime, the major carrier delocalization mechanism at elevated temperatures is possibly thermal escape of electron from QW. In addition, detailed analysis on exciton-phonon scattering mechanisms reveals that both acoustic and optical phonon scatterings play the dominant roles in the range of 300-600 K and afterwards impurity scattering is the main mechanism responsible for FWHM broadening. These results offer new insights and strategies for further development of InGaN-based optoelectronics toward the theoretical limit of their efficiency.

CHAPTER 9

CONCLUSIONS AND OUTLOOK

9.1 Conclusions

Wide bandgap InGaN materials have emerged as a promising candidate for high efficiency solar cells due to their unique intrinsic properties. This work has devoted great efforts to improve the PV performance of InGaN-based MQW solar cells both theoretically and experimentally. This dissertation first analyzed loss mechanisms and studied the theoretical limit of PV performance of InGaN solar cells (Chapter 2). Then three device design techniques have been proposed and demonstrated: band polarization engineering using nonpolar and semipolar native GaN substrates (Chapter 3), device structure design (Chapter 4) and band engineering via AlGaN elelctron- and hole-blocking layers (Chapter 5). Afterwards, the dissertation has revealed and investigated three physical mechanisms related to high temperature performance of InGaN solar cells: thermal reliability issue from 400°C to 500°C (Chapter 6), enhanced EQE and conversion efficiency with rising temperatures (Chapter 7) and carrier dynamics and localization effects inside nonpolar *m*-plane InGaN QWs at high temperatures (Chapter 8).

Chapter 2 studies the photovoltaic performance of single-junction and two-junction InGaN solar cells using a semi-analytical model. We analyze the major loss mechanisms in InGaN solar cell including transmission loss, thermalization loss, spatial relaxation loss, and recombination loss. We find that transmission loss plays a major role for InGaN solar cells due to the large bandgaps of III-nitride materials. Among the recombination losses, Shockley-Read-Hall recombination loss is the dominant process. Compared to other III-V photovoltaic materials, we discovered that the emittance of InGaN solar cells is strongly

impacted by Urbach tail energy. For two- and multi-junction InGaN solar cells, we discover that the current matching condition results in a limited range of top-junction bandgaps. This theoretical work provides detailed guidance for the design of high-performance InGaN solar cells.

In Chapter 3, we demonstrate the nonpolar and semipolar InGaN/GaN MQW solar cells grown on nonpolar *m*-plane and semipolar $(20\bar{2}1)$ plane bulk GaN substrates. The optical properties and PV performance of the nonpolar and semipolar InGaN solar cells were systematically studied, and the results were compared to the conventional polar *c*-plane devices. The absorption spectra, current density–voltage (J–V) characteristics, external quantum efficiency (EQE), and internal quantum efficiency (IQE) were measured for nonpolar *m*-plane, semipolar $(20\bar{2}1)$ plane, and polar *c*-plane InGaN/GaN MQW solar cells, respectively. Nonpolar *m*-plane InGaN/GaN MQW solar cells showed the best performance across all devices, with a high open-circuit voltage of 2.32V, low bandgap-voltage offset of 0.59V, and the highest EQE and IQE. In contrast, the polar *c*-plane device showed the lowest EQE despite the highest absorption spectra. This huge difference is attributed to the better carrier transport and collection on nonpolar *m*-plane devices due to the reduced polarization effects, which were further confirmed by bias-dependent EQE measurements and energy band diagram simulations. This study demonstrates the high potential of nonpolar and semipolar InGaN solar cells and can serve as guidance for the future design and fabrication of high efficiency III-nitride solar cells.

Chapter 4 presents a detailed study on the MOCVD growth, characterizations and optimization of InGaN/GaN MQW solar cell devices. Both PV performance at RT and elevated temperatures are characterized for comparison for future study.

Chapter 5 performs a comprehensive study on energy band engineering of InGaN MQW solar cells using AlGaN electron- and hole-blocking layers. InGaN MQW solar cells with AlGaN layers were grown by MOCVD, and high crystal quality was confirmed by high resolution X-ray diffraction (HRXRD) measurement. Time-resolved photoluminescence (TRPL) results showed that the carrier lifetime on the solar cells with AlGaN layers increased by more than 40% compared to that on the reference samples, indicating greatly improved carrier collections. The illuminated *J–V* measurements further confirmed that the short-circuit current density (*Jsc*) of the solar cells also benefited from the AlGaN layer design and increased 46%. At room temperature, the InGaN solar cells with AlGaN layers showed much higher power conversion efficiency (PCE), by up to two-fold, compared to reference devices. At high temperatures, these solar cells with AlGaN layers also delivered superior PV performance such as PCE, Jsc and FF than the reference devices. These results indicate band engineering with AlGaN layers in the InGaN MQW solar cell structures can effectively enhance the carrier collection process and is a promising design for high efficiency InGaN solar cells for both room temperature and high temperature PV applications.

Chapter 6 explored the thermal stability of InGaN solar cells under thermal stress at elevated temperatures from 400°C to 500°C. HRXRD analysis reveals that material quality of InGaN/GaN did not degrade after thermal stress. The EQE characteristics of solar cells were well-maintained at all temperatures, which demonstrates thermally robust nature of InGaN materials. Analysis of *J–V* curves indicates that the degradation of conversion efficiency of the solar cell is mainly caused by the decrease in V_{oc}, while J_{sc} and FF remain almost constant. The decrease of V_{oc} after thermal stress is attributed to the

compromised metal contacts. Transmission line method (TLM) results further confirmed that p-type contacts became Schottky-like after thermal stress. The Arrhenius model was employed to estimate the failure lifetime of InGaN solar cells under different temperatures. These results suggest that while InGaN solar cells have high thermal stability, the degradation in metal contact could be the major limiting factor for these devices under high temperature operation.

Chapter 7 shows a demonstration of III-nitride solar cells using polarization-free (i.e., nonpolar) InGaN/GaN MQW which showed a large working temperature range from room temperature to 450°C, with positive temperature coefficients up to 350°C. The peak EQEs of the devices showed a 2.5-fold enhancement from RT (~32%) to 450°C (~81%), which is distinct from all other solar cells ever reported. This can be partially attributed to an increase of over 70% in carrier lifetime in nonpolar InGaN MQW obtained from TRPL. Furthermore, a thermal radiation analysis revealed a unique self-cooling effect for III-nitride materials, which also helps enhance device performance at high temperature. These results offer new insights and strategies for the design and fabrication of high efficiency high temperature PV cells.

Chapter 8 investigates different carrier dynamics of two nonpolar *m*-plane InGaN/GaN QWs at high temperatures by combining scanning transmission electron microscopy (STEM) and photophysical characterization. Both experimental and theoretical results suggest that carrier lifetime in both samples increases with temperature in a certain range of temperature. In addition, the reduced integrity and uniformity of QWs make carriers more prone to the nonradiative Shockley-Reed-Hall recombination. Moreover, both acoustic and optical phonon scatterings dominate from 300 to 600 K

through the analysis on the evolution of photoluminescence spectra. Overall, these detailed studies provide insights into approaches to evaluate carrier dynamics at elevated temperatures and improve emitting performance to further push the practical efficiency limit.

9.2 Outlooks

To further harness and exploit the full potential of InGaN solar cells, the hybrid integration of InGaN with other high-E_g III-V is highly desired and currently under investigation. Two integration schemes have been proposed and explored previously[242], [243], as shown in Figure 9.1. The first method is oxide-oxide bonding, which has been heavily explored for III-V/Si laser integration[124]. In such scheme, the two wafer surfaces are coated with PECVD-deposited nitride, rigorously cleaned and then subjected to O_2 plasma activation. Bonding can then be initiated by using wafer-bonding equipment. Such bonds are durable at elevated temperatures, and typically strengthen as temperature is increased beyond 300°C[244]. Issues with thermal stress-induced de-bonding are a less concern, since the coefficient of thermal expansion for GaAs and GaN are remarkably similar. While this approach has the advantage that the III-N and III-V devices do not need to be current- or polarity-matched, the disadvantage is the additional interconnect processing and, ultimately, the need for circuitry to combine the mismatched power being supplied.

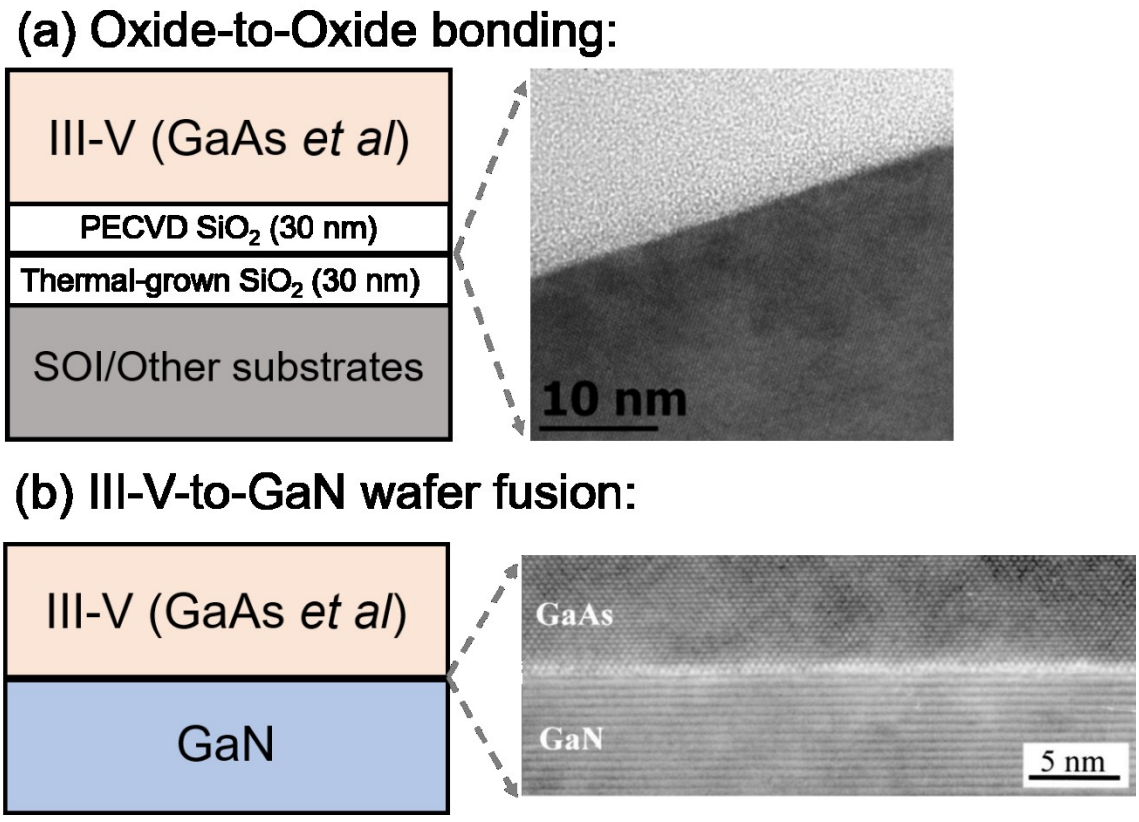

Figure 9.1: Schematic of (a) oxide-oxide bonding scheme, (b) GaAs-GaN wafer fusion. TEM images are adapted from ref [242], [243].

The second scheme is to create semiconductor-to-semiconductor bonded, electrically conductive interfaces between the bottom of the III-N top cell and the III-V bottom cells, as depicted in Fig.9.1(b). Previous research works have shown the feasibility and practicality of wafer-fused GaAs/GaN transistors. Atomic-scale smooth and clean interface was achieved and outstanding electrical performance was also demonstrated[242], [245]. In such wafer fusion, GaN and GaAs wafers were first rinsed with solvents and joined together in methanol, and annealed at 450 °C -750 °C for different time (0.5-1 h) in N_2 under 2-5 MPa of uniaxial pressure. Afterwards, mechanical polishing and wet etching were carried out to thin down and totally remove the GaAs substrate. With this approach,

III-V and GaN samples can be well bonding and the crystal structures of GaAs and GaN are maintained with the atomic arrangements clearly seen beyond the bonded interface without threading dislocations. Other successful work of GaAs to InP for integrated monolithic four-junction solar cells has proven that the photovoltaic performance was not affected by the bonded interface[246]. However, there is still no work on directly bonded GaAs-to –GaN solar cells and research effort is needed to investigate the effect of bonding interface on photovoltaic performance of such bonded tandem cells. Moreover, the bandgaps of InGaN and the underlying III-V materials require careful design to satisfy the current-matching of these tandem or multijunction cells. In addition, to realize a fully functional 2T device, an additional tunnel junction will need to be grown above the III-V cell such as $Ga_{1-y}In_yP$.

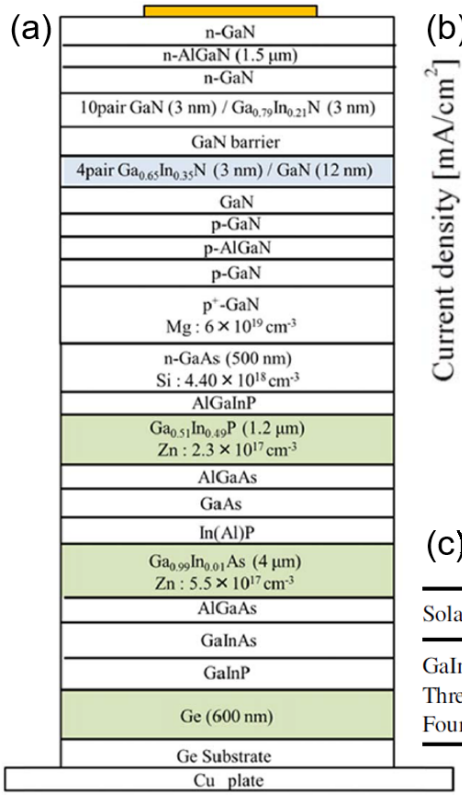

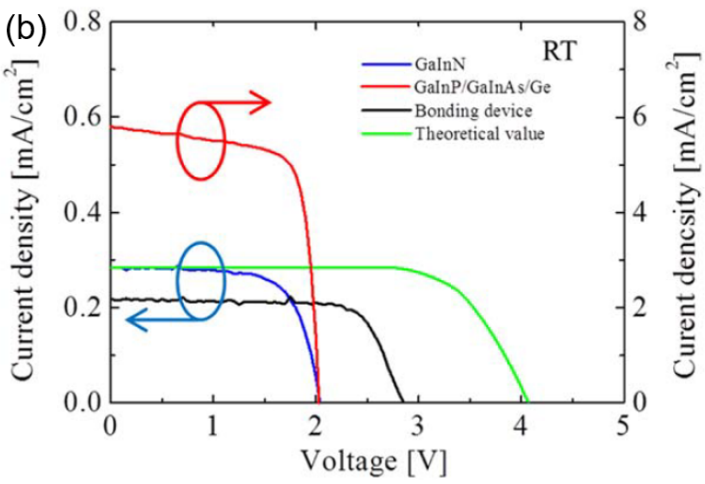

(c)

Table I. Characteristics of each device.

Solar cell	V_{OC} [V]	J_{SC} [mA cm^{-2}]	FF	η [%]
GaInN	2.04	0.285	0.69	0.402
Three-junction	2.03	5.79	0.75	8.76
Four-junction	2.85	0.219	0.74	0.460

Figure 9.2: (a) Schematic of a GaInN/GaInP/GaInAs/Ge four-junction solar cell, (b) Solar cell characteristics under AM 1.5G (1 sun) irradiation and (c) Characteristics of each device[59].

In 2019, a four-junction (4J) solar cell with InGaN top cell was reported for the first time using wafer bonding technique [59] (see Fig.9.2). A bonding temperature of 450 °C, bonding pressure of 500 N, and bonding time of 60 min are applied to achieve the optimal bonding between n-GaAs and p-GaN. The bonding strength (as per tensile testing) is 4.5 MPa, which is higher than that of an Au/Au junction (3.3 MPa), despite the PV performance is not satisfactory. The PV performance of the 4J cell will be expected to be greatly enhanced if the current matching is taken into consideration. In this case, 4 terminal scheme of such multi-junction cell is expected to be a more feasible and practical approach.

REFERENCES

[1] M. A. Green, K. Emery, Y. Hishikawa, W. Warta, and E. D. Dunlop, "Solar cell efficiency tables (Version 45)," *Prog. Photovolt. Res. Appl.*, vol. 23, no. 1, pp. 1–9, Jan. 2015, doi: 10.1002/pip.2573.

[2] J. Wu *et al.*, "Superior radiation resistance of In1−xGaxN alloys: Full-solar-spectrum photovoltaic material system," *J. Appl. Phys.*, vol. 94, no. 10, pp. 6477–6482, Nov. 2003, doi: 10.1063/1.1618353.

[3] O. Jani, I. Ferguson, C. Honsberg, and S. Kurtz, "Design and characterization of GaN/InGaN solar cells," *Appl. Phys. Lett.*, vol. 91, no. 13, p. 132117, 2007, doi: 10.1063/1.2793180.

[4] A. G. Bhuiyan, K. Sugita, A. Hashimoto, and A. Yamamoto, "InGaN Solar Cells: Present State of the Art and Important Challenges," *IEEE J. Photovolt.*, vol. 2, no. 3, pp. 276–293, Jul. 2012, doi: 10.1109/JPHOTOV.2012.2193384.

[5] N. G. Toledo and U. K. Mishra, "InGaN solar cell requirements for high-efficiency integrated III-nitride/non-III-nitride tandem photovoltaic devices," *J. Appl. Phys.*, vol. 111, no. 11, p. 114505, Jun. 2012, doi: 10.1063/1.4723831.

[6] C. A. M. Fabien *et al.*, "Simulations, Practical Limitations, and Novel Growth Technology for InGaN-Based Solar Cells," *IEEE J. Photovolt.*, vol. 4, no. 2, pp. 601–606, Mar. 2014, doi: 10.1109/JPHOTOV.2013.2292748.

[7] Y. Zhao, R. M. Farrell, Y.-R. Wu, and J. S. Speck, "Valence band states and polarized optical emission from nonpolar and semipolar III–nitride quantum well optoelectronic devices," *Jpn. J. Appl. Phys.*, vol. 53, no. 10, p. 100206, Oct. 2014, doi: 10.7567/JJAP.53.100206.

[8] E. F. Schubert, *Light-emitting diodes*. Cambridge; New York: Cambridge University Press, 2006.

[9] C. Yang *et al.*, "Photovoltaic effects in InGaN structures with p–n junctions," *Phys. Status Solidi A*, vol. 204, no. 12, pp. 4288–4291, 2007, doi: 10.1002/pssa.200723202.

[10] C. J. Neufeld, N. G. Toledo, S. C. Cruz, M. Iza, S. P. DenBaars, and U. K. Mishra, "High quantum efficiency InGaN/GaN solar cells with 2.95 eV band gap," *Appl. Phys. Lett.*, vol. 93, no. 14, p. 143502, 2008, doi: 10.1063/1.2988894.

[11] S. W. Zeng, B. P. Zhang, J. W. Sun, J. F. Cai, C. Chen, and J. Z. Yu, "Substantial photo-response of InGaN p–i–n homojunction solar cells," *Semicond. Sci. Technol.*, vol. 24, no. 5, p. 055009, 2009, doi: 10.1088/0268-1242/24/5/055009.

[12] R.-H. Horng *et al.*, "Improved Conversion Efficiency of GaN/InGaN Thin-Film Solar Cells," *IEEE Electron Device Lett.*, vol. 30, no. 7, pp. 724–726, Jul. 2009, doi: 10.1109/LED.2009.2021414.

[13] B. R. Jampana *et al.*, “Design and Realization of Wide-Band-Gap (2.67 eV) InGaN p-n Junction Solar Cell,” *IEEE Electron Device Lett.*, vol. 31, no. 1, pp. 32–34, Jan. 2010, doi: 10.1109/LED.2009.2034280.

[14] J. P. Shim, S. R. Jeon, Y. K. Jeong, and D. S. Lee, “Improved Efficiency by Using Transparent Contact Layers in InGaN-Based p-i-n Solar Cells,” *IEEE Electron Device Lett.*, vol. 31, no. 10, pp. 1140–1142, Oct. 2010, doi: 10.1109/LED.2010.2058087.

[15] R. Dahal, B. Pantha, J. Li, J. Y. Lin, and H. X. Jiang, “InGaN/GaN multiple quantum well solar cells with long operating wavelengths,” *Appl. Phys. Lett.*, vol. 94, no. 6, p. 063505, 2009, doi: 10.1063/1.3081123.

[16] K. Y. Lai, G. J. Lin, Y.-L. Lai, Y. F. Chen, and J. H. He, “Effect of indium fluctuation on the photovoltaic characteristics of InGaN/GaN multiple quantum well solar cells,” *Appl. Phys. Lett.*, vol. 96, no. 8, p. 081103, 2010, doi: 10.1063/1.3327331.

[17] R. Dahal, J. Li, K. Aryal, J. Y. Lin, and H. X. Jiang, “InGaN/GaN multiple quantum well concentrator solar cells,” *Appl. Phys. Lett.*, vol. 97, no. 7, p. 073115, 2010, doi: 10.1063/1.3481424.

[18] R. M. Farrell *et al.*, “High quantum efficiency InGaN/GaN multiple quantum well solar cells with spectral response extending out to 520 nm,” *Appl. Phys. Lett.*, vol. 98, no. 20, p. 201107, 2011, doi: 10.1063/1.3591976.

[19] Y. Kuwahara *et al.*, “GaInN-Based Solar Cells Using Strained-Layer GaInN/GaInN Superlattice Active Layer on a Freestanding GaN Substrate,” *Appl. Phys. Express*, vol. 4, no. 2, p. 021001, Jan. 2011, doi: 10.1143/APEX.4.021001.

[20] Y.-J. Lee, M.-H. Lee, C.-M. Cheng, and C.-H. Yang, “Enhanced conversion efficiency of InGaN multiple quantum well solar cells grown on a patterned sapphire substrate,” *Appl. Phys. Lett.*, vol. 98, no. 26, p. 263504, 2011, doi: 10.1063/1.3605244.

[21] C. J. Neufeld *et al.*, “Effect of doping and polarization on carrier collection in InGaN quantum well solar cells,” *Appl. Phys. Lett.*, vol. 98, no. 24, p. 243507, 2011, doi: 10.1063/1.3595487.

[22] G. J. Lin, K. Y. Lai, C. A. Lin, Y. L. Lai, and J. H. He, “Efficiency Enhancement of InGaN-Based Multiple Quantum Well Solar Cells Employing Antireflective ZnO Nanorod Arrays,” *IEEE Electron Device Lett.*, vol. 32, no. 8, pp. 1104–1106, Aug. 2011, doi: 10.1109/LED.2011.2158061.

[23] L. Zhao, W. Hou, Y. Li, T. Detchprohm, and C. Wetzel, “Photocurrent spectroscopy on GaInN/GaN multiple quantum well solar cell structures,” *Phys. Status Solidi C*, vol. 8, no. 7–8, pp. 2469–2472, Jul. 2011, doi: 10.1002/pssc.201001200.

[24] Y.-L. Hu *et al.*, “Effect of quantum well cap layer thickness on the microstructure and performance of InGaN/GaN solar cells,” *Appl. Phys. Lett.*, vol. 100, no. 16, p. 161101, Apr. 2012, doi: 10.1063/1.4704189.

[25] J. J. Wierer, D. D. Koleske, and S. R. Lee, “Influence of barrier thickness on the performance of InGaN/GaN multiple quantum well solar cells,” *Appl. Phys. Lett.*, vol. 100, no. 11, p. 111119, 2012, doi: 10.1063/1.3695170.

[26] P. H. Fu *et al.*, “Efficiency enhancement of InGaN multi-quantum-well solar cells via light-harvesting SiO2 nano-honeycombs,” *Appl. Phys. Lett.*, vol. 100, no. 1, p. 013105, 2012, doi: 10.1063/1.3673838.

[27] C.-H. Ho, K.-Y. Lai, C.-A. Lin, G.-J. Lin, M.-K. Hsing, and J.-H. He, “Microdome InGaN-based multiple quantum well solar cells,” *Appl. Phys. Lett.*, vol. 101, no. 2, p. 023902, 2012, doi: 10.1063/1.4734380.

[28] D.-J. Seo, J.-P. Shim, S.-B. Choi, T. H. Seo, E.-K. Suh, and D.-S. Lee, “Efficiency improvement in InGaN-based solar cells by indium tin oxide nano dots covered with ITO films,” *Opt. Express*, vol. 20, no. S6, p. A991, Nov. 2012, doi: 10.1364/OE.20.00A991.

[29] M. Mori *et al.*, “Correlation between Device Performance and Defects in GaInN-Based Solar Cells,” *Appl. Phys. Express*, vol. 5, no. 8, p. 082301, Jul. 2012, doi: 10.1143/APEX.5.082301.

[30] S. Yamamoto *et al.*, “Properties of nitride-based photovoltaic cells under concentrated light illumination,” *Phys. Status Solidi RRL – Rapid Res. Lett.*, vol. 6, no. 4, pp. 145–147, Apr. 2012, doi: 10.1002/pssr.201206038.

[31] C. H. Ho *et al.*, “An efficient light-harvesting scheme using SiO2 nanorods for InGaN multiple quantum well solar cells,” *Sol. Energy Mater. Sol. Cells*, vol. 103, pp. 194–198, Aug. 2012, doi: 10.1016/j.solmat.2012.04.007.

[32] C. Y. Liu *et al.*, “Nitride-based concentrator solar cells grown on Si substrates,” *Sol. Energy Mater. Sol. Cells*, vol. 117, pp. 54–58, Oct. 2013, doi: 10.1016/j.solmat.2013.05.017.

[33] S. Valdueza-Felip *et al.*, “Photovoltaic Response of InGaN/GaN Multiple-Quantum Well Solar Cells,” *Jpn. J. Appl. Phys.*, vol. 52, no. 8S, p. 08JH05, Aug. 2013, doi: 10.7567/JJAP.52.08JH05.

[34] S.-B. Choi *et al.*, “Effect of indium composition on carrier escape in InGaN/GaN multiple quantum well solar cells,” *Appl. Phys. Lett.*, vol. 103, no. 3, p. 033901, 2013, doi: 10.1063/1.4813623.

[35] S. Valdueza-Felip *et al.*, “Improved conversion efficiency of as-grown InGaN/GaN quantum-well solar cells for hybrid integration,” *Appl. Phys. Express*, vol. 7, no. 3, p. 032301, Mar. 2014, doi: 10.7567/APEX.7.032301.

[36] N. G. Young *et al.*, “High-performance broadband optical coatings on InGaN/GaN solar cells for multijunction device integration,” *Appl. Phys. Lett.*, vol. 104, no. 16, p. 163902, Apr. 2014, doi: 10.1063/1.4873117.

[37] L. Zhao, T. Detchprohm, and C. Wetzel, “High 400 °C operation temperature blue spectrum concentration solar junction in GaInN/GaN,” *Appl. Phys. Lett.*, vol. 105, no. 24, p. 243903, Dec. 2014, doi: 10.1063/1.4904717.

[38] K. Y. Lai, G. J. Lin, Y.-R. Wu, M.-L. Tsai, and J.-H. He, “Efficiency dip observed with InGaN-based multiple quantum well solar cells,” *Opt. Express*, vol. 22, no. S7, p. A1753, Dec. 2014, doi: 10.1364/OE.22.0A1753.

[39] L. Redaelli *et al.*, “Effect of the barrier thickness on the performance of multiple-quantum-well InGaN photovoltaic cells,” *Jpn. J. Appl. Phys.*, vol. 54, no. 7, p. 072302, Jul. 2015, doi: 10.7567/JJAP.54.072302.

[40] D.-H. Lien *et al.*, “Harsh photovoltaics using InGaN/GaN multiple quantum well schemes,” *Nano Energy*, vol. 11, pp. 104–109, Jan. 2015, doi: 10.1016/j.nanoen.2014.10.013.

[41] E. Dogmus *et al.*, “High structural quality InGaN/GaN multiple quantum well solar cells,” *Phys. Status Solidi C*, vol. 12, no. 12, pp. 1412–1415, Dec. 2015, doi: 10.1002/pssc.201510137.

[42] A. Mukhtarova *et al.*, “Dependence of the photovoltaic performance of pseudomorphic InGaN/GaN multiple-quantum-well solar cells on the active region thickness,” *Appl. Phys. Lett.*, vol. 108, no. 16, p. 161907, Apr. 2016, doi: 10.1063/1.4947445.

[43] Z. Bi *et al.*, “An InGaN based solar cell including dual InGaN/GaN multiple quantum wells,” *IEEE Photonics Technol. Lett.*, vol. PP, no. 99, pp. 1–1, 2016, doi: 10.1109/LPT.2016.2575058.

[44] Z. Chen *et al.*, “Positive temperature coefficient of photovoltaic efficiency in solar cells based on InGaN/GaN MQWs,” *Appl. Phys. Lett.*, vol. 109, no. 6, p. 062104, Aug. 2016, doi: 10.1063/1.4960765.

[45] J. Yang *et al.*, “Photovoltaic Response of InGaN/GaN Multi-quantum Well Solar Cells Enhanced by Reducing p-type GaN Resistivity,” *IEEE J. Photovolt.*, vol. 6, no. 2, pp. 454–459, Mar. 2016, doi: 10.1109/JPHOTOV.2015.2504788.

[46] S. Liu *et al.*, “Optimization of growth and fabrication techniques to enhance the InGaN/GaN multiple quantum well solar cells performance,” *Superlattices Microstruct.*, May 2017, doi: 10.1016/j.spmi.2017.05.014.

[47] W. Liu *et al.*, “Influence of Indium Content on the Unintentional Background Doping and Device Performance of InGaN/GaN Multiple-Quantum-Well Solar Cells,” *IEEE J. Photovolt.*, vol. 7, no. 4, pp. 1017–1023, Jul. 2017, doi: 10.1109/JPHOTOV.2017.2699199.

[48] C. Jiang *et al.*, “Enhanced Solar Cell Conversion Efficiency of InGaN/GaN Multiple Quantum Wells by Piezo-Phototronic Effect,” *ACS Nano*, Sep. 2017, doi: 10.1021/acsnano.7b04935.

[49] J. J. Williams *et al.*, "Refractory In_x Ga_{1-x} N Solar Cells for High-Temperature Applications," *IEEE J. Photovolt.*, vol. 7, no. 6, pp. 1646–1652, Nov. 2017, doi: 10.1109/JPHOTOV.2017.2756057.

[50] E. Vadiee *et al.*, "InGaN solar cells with regrown GaN homojunction tunnel contacts," *Appl. Phys. Express*, vol. 11, no. 8, p. 082304, Aug. 2018, doi: 10.7567/APEX.11.082304.

[51] T. Ayari *et al.*, "Heterogeneous Integration of Thin-Film InGaN-Based Solar Cells on Foreign Substrates with Enhanced Performance," *ACS Photonics*, vol. 5, no. 8, pp. 3003–3008, Aug. 2018, doi: 10.1021/acsphotonics.8b00663.

[52] X. M. Cai, Z. W. Zheng, H. Long, L. Y. Ying, and B. P. Zhang, "Abnormal staircase-like I-V curve in InGaN quantum well solar cells," *Appl. Phys. Lett.*, vol. 112, no. 16, p. 161102, Apr. 2018, doi: 10.1063/1.5018481.

[53] Z. Bi *et al.*, "An InGaN/GaN MQWs Solar Cell Improved By a Surficial GaN Nanostructure as Light Traps," *IEEE Photonics Technol. Lett.*, vol. 30, no. 1, pp. 83–86, Jan. 2018, doi: 10.1109/LPT.2017.2775706.

[54] E. Vadiee *et al.*, "Evaluating the performance of InGaN/GaN multi-quantum-well solar cells operated at elevated temperatures via DC and small-signal AC analysis," *Jpn. J. Appl. Phys.*, vol. 58, no. 10, p. 101003, Sep. 2019, doi: 10.7567/1347-4065/ab3b66.

[55] J.-K. Sheu, F.-B. Chen, S.-H. Wu, M.-L. Lee, P.-C. Chen, and Y.-H. Yeh, "Vertical InGaN-based green-band solar cells operating under high solar concentration up to 300 suns," *Opt. Express*, vol. 22, no. S5, p. A1222, Aug. 2014, doi: 10.1364/OE.22.0A1222.

[56] M. Mori *et al.*, "Concentrating Properties of Nitride-Based Solar Cells Using Different Electrodes," *Jpn. J. Appl. Phys.*, vol. 52, no. 8S, p. 08JH02, Aug. 2013, doi: 10.7567/JJAP.52.08JH02.

[57] J. J. Williams *et al.*, "Development of a high-band gap high temperature III-nitride solar cell for integration with concentrated solar power technology," in *2016 IEEE 43rd Photovoltaic Specialists Conference (PVSC)*, 2016, pp. 0193–0195, doi: 10.1109/PVSC.2016.7749576.

[58] X. Huang *et al.*, "High-Temperature Polarization-Free III-Nitride Solar Cells with Self-Cooling Effects," *ACS Photonics*, vol. 6, no. 8, pp. 2096–2103, Aug. 2019, doi: 10.1021/acsphotonics.9b00655.

[59] K. Takahashi *et al.*, "Fabrication of a GaInN/GaInP/GaInAs/Ge four-junction solar cell using the wafer bonding technology," *Jpn. J. Appl. Phys.*, vol. 58, no. 7, p. 072003, Jun. 2019, doi: 10.7567/1347-4065/ab26ad.

[60] X. Huang, H. Fu, H. Chen, Z. Lu, D. Ding, and Y. Zhao, "Analysis of loss mechanisms in InGaN solar cells using a semi-analytical model," *J. Appl. Phys.*, vol. 119, no. 21, p. 213101, Jun. 2016, doi: 10.1063/1.4953006.

[61] X. Huang *et al.*, “Nonpolar and semipolar InGaN/GaN multiple-quantum-well solar cells with improved carrier collection efficiency,” *Appl. Phys. Lett.*, vol. 110, no. 16, p. 161105, Apr. 2017, doi: 10.1063/1.4980139.

[62] X. Huang *et al.*, “Reliability analysis of InGaN/GaN multi-quantum-well solar cells under thermal stress,” *Appl. Phys. Lett.*, vol. 111, no. 23, p. 233511, Dec. 2017, doi: 10.1063/1.5006650.

[63] X. Huang *et al.*, “Energy band engineering of InGaN/GaN multi-quantum-well solar cells via AlGaN electron- and hole-blocking layers,” *Appl. Phys. Lett.*, vol. 113, no. 4, p. 043501, Jul. 2018, doi: 10.1063/1.5028530.

[64] X. Huang *et al.*, “Steep-slope field-effect transistors with AlGaN/GaN HEMT and oxide-based threshold switching device,” *Nanotechnology*, vol. 30, no. 21, p. 215201, Mar. 2019, doi: 10.1088/1361-6528/ab0484.

[65] N. G. Toledo *et al.*, “Design of integrated III-nitride/non-III-nitride tandem photovoltaic devices,” *J. Appl. Phys.*, vol. 111, no. 5, p. 054503, Mar. 2012, doi: 10.1063/1.3690907.

[66] D. Ding, S. R. Johnson, S.-Q. Yu, S.-N. Wu, and Y.-H. Zhang, “A semi-analytical model for semiconductor solar cells,” *J. Appl. Phys.*, vol. 110, no. 12, p. 123104, Dec. 2011, doi: 10.1063/1.3671061.

[67] D. Ding, S. R. Johnson, and Y.-H. Zhang, “A semi-analytical model for semiconductor solar cells: From detailed balance to practical devices,” in *Photovoltaic Specialists Conference (PVSC), 2010 35th IEEE*, 2010, pp. 002908–002911.

[68] S. L. Chuang, *Physics of Photonic Devices*. John Wiley & Sons, 2012.

[69] S. Liu, D. Ding, S. R. Johnson, and Y.-H. Zhang, “Optimal optical designs for planar GaAs single-junction solar cells with textured and reflective surfaces,” 2012, p. 82560M, doi: 10.1117/12.909841.

[70] E. Matioli *et al.*, “High internal and external quantum efficiency InGaN/GaN solar cells,” *Appl. Phys. Lett.*, vol. 98, no. 2, p. 021102, 2011, doi: 10.1063/1.3540501.

[71] C. J. Neufeld *et al.*, “Observation of positive thermal power coefficient in InGaN/GaN quantum well solar cells,” *Appl. Phys. Lett.*, vol. 99, no. 7, p. 071104, 2011, doi: 10.1063/1.3624850.

[72] S. Adachi, *Properties of semiconductor alloys: group-IV, III-V and II-VI semiconductors*. Chichester, U.K: Wiley, 2009.

[73] M. M. Leung, A. B. Djurišić, and E. H. Li, “Refractive index of InGaN/GaN quantum well,” *J. Appl. Phys.*, vol. 84, no. 11, pp. 6312–6317, 1998.

[74] R. W. Martin, P. G. Middleton, K. P. O'Donnell, and W. V. der Stricht, "Exciton localization and the Stokes' shift in InGaN epilayers," *Appl. Phys. Lett.*, vol. 74, no. 2, pp. 263–265, Jan. 1999, doi: 10.1063/1.123275.

[75] M. Yamada *et al.*, "InGaN-based near-ultraviolet and blue-light-emitting diodes with high external quantum efficiency using a patterned sapphire substrate and a mesh electrode," *Jpn. J. Appl. Phys. Part 2-Lett. Express Lett.*, vol. 41, no. 12B, pp. L1431–L1433, Dec. 2002, doi: 10.1143/JJAP.41.L1431.

[76] D. S. Wuu *et al.*, "Defect reduction and efficiency improvement of near-ultraviolet emitters via laterally overgrown GaN on a GaN/patterned sapphire template," *Appl. Phys. Lett.*, vol. 89, no. 16, p. 161105, Oct. 2006, doi: 10.1063/1.2363148.

[77] H. Gao, F. Yan, Y. Zhang, J. Li, Y. Zeng, and G. Wang, "Enhancement of the light output power of InGaN/GaN light-emitting diodes grown on pyramidal patterned sapphire substrates in the micro- and nanoscale," *J. Appl. Phys.*, vol. 103, no. 1, p. 014314, Jan. 2008, doi: 10.1063/1.2830981.

[78] H. Chen *et al.*, "Enhanced Performance of GaN-Based Light-Emitting Diodes by Using Al Mirror and Atomic Layer Deposition-TiO_2 /Al_2O_3 Distributed Bragg Reflector Backside Reflector with Patterned Sapphire Substrate," *Appl. Phys. Express*, vol. 6, no. 2, p. 022101, Feb. 2013, doi: 10.7567/APEX.6.022101.

[79] J. Lee and C. B. Honsberg, "Limiting Efficiencies of Multijunction Solar Cells With Multiple Exciton Generation," *IEEE J. Photovolt.*, vol. 4, no. 3, pp. 874–880, May 2014, doi: 10.1109/JPHOTOV.2014.2307156.

[80] M. Beaudoin, A. J. G. DeVries, S. R. Johnson, H. Laman, and T. Tiedje, "Optical absorption edge of semi-insulating GaAs and InP at high temperatures," *Appl. Phys. Lett.*, vol. 70, no. 26, pp. 3540–3542, Jun. 1997, doi: 10.1063/1.119226.

[81] C. H. Grein and S. John, "Temperature dependence of the Urbach optical absorption edge: A theory of multiple phonon absorption and emission sidebands," *Phys. Rev. B*, vol. 39, no. 2, p. 1140, 1989.

[82] F. Meillaud, A. Shah, C. Droz, E. Vallat-Sauvain, and C. Miazza, "Efficiency limits for single-junction and tandem solar cells," *Sol. Energy Mater. Sol. Cells*, vol. 90, no. 18–19, pp. 2952–2959, Nov. 2006, doi: 10.1016/j.solmat.2006.06.002.

[83] C. H. Qiu, C. Hoggatt, W. Melton, M. W. Leksono, and J. I. Pankove, "Study of defect states in GaN films by photoconductivity measurement," *Appl. Phys. Lett.*, vol. 66, no. 20, pp. 2712–2714, May 1995, doi: 10.1063/1.113497.

[84] A. Cremades, L. Görgens, O. Ambacher, M. Stutzmann, and F. Scholz, "Structural and optical properties of Si-doped GaN," *Phys. Rev. B*, vol. 61, no. 4, pp. 2812–2818, Jan. 2000, doi: 10.1103/PhysRevB.61.2812.

[85] S. Chichibu *et al.*, "Urbach–Martienssen tails in a wurtzite GaN epilayer," *Appl. Phys. Lett.*, vol. 70, no. 25, p. 3440, 1997, doi: 10.1063/1.119196.

[86] N. G. Young *et al.*, “High performance thin quantum barrier InGaN/GaN solar cells on sapphire and bulk (0001) GaN substrates,” *Appl. Phys. Lett.*, vol. 103, no. 17, p. 173903, 2013.

[87] Chun-Ta Yu, Wei-Chih Lai, Cheng-Hsiung Yen, Ching-Wen Chang, Li-Wei Tu, and Shoou-Jinn Chang, “Conversion Efficiency Improvement of InGaN/GaN Multiple-Quantum-Well Solar Cells With Ex Situ AlN Nucleation Layer,” *IEEE Trans. Electron Devices*, vol. 62, no. 5, pp. 1473–1477, May 2015, doi: 10.1109/TED.2015.2415254.

[88] S. P. DenBaars *et al.*, “Development of gallium-nitride-based light-emitting diodes (LEDs) and laser diodes for energy-efficient lighting and displays,” *Acta Mater.*, vol. 61, no. 3, pp. 945–951, Feb. 2013, doi: 10.1016/j.actamat.2012.10.042.

[89] Y. Kawaguchi *et al.*, “Influence of polarity on carrier transport in semipolar ($20\bar{2}1$) and ($20\bar{2}\bar{1}$) multiple-quantum-well light-emitting diodes,” *Appl. Phys. Lett.*, vol. 100, no. 23, p. 231110, Jun. 2012, doi: 10.1063/1.4726106.

[90] H. Fu, Z. Lu, and Y. Zhao, “Analysis of low efficiency droop of semipolar InGaN quantum well light-emitting diodes by modified rate equation with weak phase-space filling effect,” *AIP Adv.*, vol. 6, no. 6, p. 065013, Jun. 2016, doi: 10.1063/1.4954296.

[91] H. Chen, H. Fu, Z. Lu, X. Huang, and Y. Zhao, “Optical properties of highly polarized InGaN light-emitting diodes modified by plasmonic metallic grating,” *Opt. Express*, vol. 24, no. 10, p. A856, May 2016, doi: 10.1364/OE.24.00A856.

[92] L. Sang, M. Liao, Y. Koide, and M. Sumiya, “InGaN-based thin film solar cells: Epitaxy, structural design, and photovoltaic properties,” *J. Appl. Phys.*, vol. 117, no. 10, p. 105706, Mar. 2015, doi: 10.1063/1.4914908.

[93] Y. Enya *et al.*, “531 nm Green Lasing of InGaN Based Laser Diodes on Semi-Polar {20\bar21} Free-Standing GaN Substrates,” *Appl. Phys. Express*, vol. 2, p. 082101, Jul. 2009, doi: 10.1143/APEX.2.082101.

[94] J. T. Leonard *et al.*, “Nonpolar III-nitride vertical-cavity surface-emitting laser with a photoelectrochemically etched air-gap aperture,” *Appl. Phys. Lett.*, vol. 108, no. 3, p. 031111, Jan. 2016, doi: 10.1063/1.4940380.

[95] H. Fu, Z. Lu, X. Huang, H. Chen, and Y. Zhao, “Crystal orientation dependent intersubband transition in semipolar AlGaN/GaN single quantum well for optoelectronic applications,” *J. Appl. Phys.*, vol. 119, no. 17, p. 174502, May 2016, doi: 10.1063/1.4948667.

[96] S. Sakr, E. Giraud, A. Dussaigne, M. Tchernycheva, N. Grandjean, and F. H. Julien, “Two-color GaN/AlGaN quantum cascade detector at short infrared wavelengths of 1 and 1.7 μm,” *Appl. Phys. Lett.*, vol. 100, no. 18, p. 181103, Apr. 2012, doi: 10.1063/1.4707904.

[97] E. Bellotti, K. Driscoll, T. D. Moustakas, and R. Paiella, "Monte Carlo study of GaN versus GaAs terahertz quantum cascade structures," *Appl. Phys. Lett.*, vol. 92, no. 10, p. 101112, Mar. 2008, doi: 10.1063/1.2894508.

[98] V. F. Mymrin, K. A. Bulashevich, N. I. Podolskaya, I. A. Zhmakin, S. Yu. Karpov, and Yu. N. Makarov, "Modelling study of MQW LED operation," *Phys. Status Solidi C*, vol. 2, no. 7, pp. 2928–2931, May 2005, doi: 10.1002/pssc.200461289.

[99] S. F. Chichibu *et al.*, "Origin of defect-insensitive emission probability in In-containing (Al,In,Ga)N alloy semiconductors," *Nat. Mater.*, vol. 5, no. 10, pp. 810–816, Oct. 2006, doi: 10.1038/nmat1726.

[100] S. John, C. Soukoulis, M. H. Cohen, and E. N. Economou, "Theory of Electron Band Tails and the Urbach Optical-Absorption Edge," *Phys. Rev. Lett.*, vol. 57, no. 14, pp. 1777–1780, Oct. 1986, doi: 10.1103/PhysRevLett.57.1777.

[101] R. R. King *et al.*, "Band gap-voltage offset and energy production in next-generation multijunction solar cells," *Prog. Photovolt. Res. Appl.*, vol. 19, no. 7, pp. 797–812, Nov. 2011, doi: 10.1002/pip.1044.

[102] J. R. Lang, N. G. Young, R. M. Farrell, Y.-R. Wu, and J. S. Speck, "Carrier escape mechanism dependence on barrier thickness and temperature in InGaN quantum well solar cells," *Appl. Phys. Lett.*, vol. 101, no. 18, p. 181105, 2012, doi: 10.1063/1.4765068.

[103] H. Fu, X. Huang, H. Chen, Z. Lu, X. Zhang, and Y. Zhao, "Effect of Buffer Layer Design on Vertical GaN-on-GaN p-n and Schottky Power Diodes," *IEEE Electron Device Lett.*, vol. 38, no. 6, pp. 763–766, Jun. 2017, doi: 10.1109/LED.2017.2690974.

[104] D. Disney, H. Nie, A. Edwards, D. Bour, H. Shah, and I. C. Kizilyalli, "Vertical power diodes in bulk GaN," in *2013 25th International Symposium on Power Semiconductor Devices IC's (ISPSD)*, 2013, pp. 59–62, doi: 10.1109/ISPSD.2013.6694455.

[105] M. Qi *et al.*, "High breakdown single-crystal GaN p-n diodes by molecular beam epitaxy," *Appl. Phys. Lett.*, vol. 107, no. 23, p. 232101, Dec. 2015, doi: 10.1063/1.4936891.

[106] H. Ohta *et al.*, "Vertical GaN p-n Junction Diodes With High Breakdown Voltages Over 4 kV," *IEEE Electron Device Lett.*, vol. 36, no. 11, pp. 1180–1182, Nov. 2015, doi: 10.1109/LED.2015.2478907.

[107] H. Fu, X. Huang, H. Chen, Z. Lu, I. Baranowski, and Y. Zhao, "Ultra-low turn-on voltage and on-resistance vertical GaN-on-GaN Schottky power diodes with high mobility double drift layers," *Appl. Phys. Lett.*, vol. 111, no. 15, p. 152102, Oct. 2017, doi: 10.1063/1.4993201.

[108] D. Ji *et al.*, "Large Area In-Situ Oxide, GaN Interlayer Based Vertical Trench MOSFET (OG-FET)," *IEEE Electron Device Lett.*, vol. PP, no. 99, pp. 1–1, 2018, doi: 10.1109/LED.2018.2813312.

[109] S. Nakamura, T. Mukai, and M. Senoh, “Candela-class high-brightness InGaN/AlGaN double-heterostructure blue-light-emitting diodes,” *Appl. Phys. Lett.*, vol. 64, no. 13, pp. 1687–1689, Mar. 1994, doi: 10.1063/1.111832.

[110] Y. Zhao *et al.*, “High-Power Blue-Violet Semipolar ($20\bar{2}\bar{1}$) InGaN/GaN Light-Emitting Diodes with Low Efficiency Droop at 200 A/cm^{2},” *Appl. Phys. Express*, vol. 4, no. 8, p. 082104, Jul. 2011, doi: 10.1143/APEX.4.082104.

[111] R. M. Farrell, E. C. Young, F. Wu, S. P. DenBaars, and J. S. Speck, “Materials and growth issues for high-performance nonpolar and semipolar light-emitting devices,” *Semicond. Sci. Technol.*, vol. 27, no. 2, p. 024001, 2012, doi: 10.1088/0268-1242/27/2/024001.

[112] Z. Lu *et al.*, “Active tracking system for visible light communication using a GaN-based micro-LED and NRZ-OOK,” *Opt. Express*, vol. 25, no. 15, pp. 17971–17981, Jul. 2017, doi: 10.1364/OE.25.017971.

[113] C. Xiong *et al.*, “Integrated GaN photonic circuits on silicon (100) for second harmonic generation,” *Opt. Express*, vol. 19, no. 11, pp. 10462–10470, May 2011, doi: 10.1364/OE.19.010462.

[114] H. Chen *et al.*, “Low loss GaN waveguides at the visible spectral wavelengths for integrated photonics applications,” *Opt. Express*, vol. 25, no. 25, p. 31758, Dec. 2017, doi: 10.1364/OE.25.031758.

[115] N. Vico Triviño, U. Dharanipathy, J.-F. Carlin, Z. Diao, R. Houdré, and N. Grandjean, “Integrated photonics on silicon with wide bandgap GaN semiconductor,” *Appl. Phys. Lett.*, vol. 102, no. 8, p. 081120, Feb. 2013, doi: 10.1063/1.4793759.

[116] H. Chen *et al.*, “Characterizations of nonlinear optical properties on GaN crystals in polar, nonpolar, and semipolar orientations,” *Appl. Phys. Lett.*, vol. 110, no. 18, p. 181110, May 2017, doi: 10.1063/1.4983026.

[117] X. Zheng *et al.*, “High-quality InGaN/GaN heterojunctions and their photovoltaic effects,” *Appl. Phys. Lett.*, vol. 93, no. 26, p. 261108, Dec. 2008, doi: 10.1063/1.3056628.

[118] J. Wu, “When group-III nitrides go infrared: New properties and perspectives,” *J. Appl. Phys.*, vol. 106, no. 1, p. 011101, Jul. 2009, doi: 10.1063/1.3155798.

[119] Y. Kuwahara *et al.*, “Realization of Nitride-Based Solar Cell on Freestanding GaN Substrate,” *Appl. Phys. Express*, vol. 3, no. 11, p. 111001, Oct. 2010, doi: 10.1143/APEX.3.111001.

[120] J. Bai, Y. P. Gong, Z. Li, Y. Zhang, and T. Wang, “Semi-polar InGaN/GaN multiple quantum well solar cells with spectral response at up to 560 nm,” *Sol. Energy Mater. Sol. Cells*, vol. 175, pp. 47–51, Feb. 2018, doi: 10.1016/j.solmat.2017.10.005.

[121] K. Masuko *et al.*, “Achievement of More Than 25% Conversion Efficiency With Crystalline Silicon Heterojunction Solar Cell,” *IEEE J. Photovolt.*, vol. 4, no. 6, pp. 1433–1435, Nov. 2014, doi: 10.1109/JPHOTOV.2014.2352151.

[122] C. Zhang, Y. Kim, C. Ebert, N. N. Faleev, and C. B. Honsberg, "Influence of high growth rate on GaAs-based solar cells grown by metalorganic chemical vapor deposition," in *2015 IEEE 42nd Photovoltaic Specialist Conference (PVSC)*, 2015, pp. 1–5, doi: 10.1109/PVSC.2015.7356064.

[123] M. Vaisman *et al.*, "15.3%-Efficient GaAsP Solar Cells on GaP/Si Templates," *ACS Energy Lett.*, vol. 2, no. 8, pp. 1911–1918, Aug. 2017, doi: 10.1021/acsenergylett.7b00538.

[124] S. Essig *et al.*, "Raising the one-sun conversion efficiency of III–V/Si solar cells to 32.8% for two junctions and 35.9% for three junctions," *Nat. Energy*, vol. 6, p. nenergy2017144, Aug. 2017, doi: 10.1038/nenergy.2017.144.

[125] Y. Zhao *et al.*, "Monocrystalline CdTe solar cells with open-circuit voltage over 1 V and efficiency of 17%," *Nat. Energy*, vol. 1, no. 6, p. 16067, May 2016, doi: 10.1038/nenergy.2016.67.

[126] P. Reinhard *et al.*, "Review of progress toward 20% efficiency flexible CIGS solar cells and manufacturing issues of solar modules," in *2012 IEEE 38th Photovoltaic Specialists Conference (PVSC) PART 2*, 2012, pp. 1–9, doi: 10.1109/PVSC-Vol2.2012.6656789.

[127] A. M. Yong, C. B. Soh, X. H. Zhang, S. Y. Chow, and S. J. Chua, "Investigation of V-defects formation in InGaN/GaN multiple quantum well grown on sapphire," *Thin Solid Films*, vol. 515, no. 10, pp. 4496–4500, Mar. 2007, doi: 10.1016/j.tsf.2006.07.181.

[128] H. Fu *et al.*, "Study of Low-Efficiency Droop in Semipolar (20-2-1) InGaN Light-Emitting Diodes by Time-Resolved Photoluminescence," *J. Disp. Technol.*, vol. 12, no. 7, pp. 736–741, Jul. 2016, doi: 10.1109/JDT.2016.2521618.

[129] R. R. King *et al.*, "Band gap-voltage offset and energy production in next-generation multijunction solar cells," *Prog. Photovolt. Res. Appl.*, vol. 19, no. 7, pp. 797–812, Nov. 2011, doi: 10.1002/pip.1044.

[130] P. Singh and N. M. Ravindra, "Temperature dependence of solar cell performance—an analysis," *Sol. Energy Mater. Sol. Cells*, vol. 101, pp. 36–45, Jun. 2012, doi: 10.1016/j.solmat.2012.02.019.

[131] Y.-F. Wu, D. Kapolnek, J. P. Ibbetson, P. Parikh, B. P. Keller, and U. K. Mishra, "Very-high power density AlGaN/GaN HEMTs," *IEEE Trans. Electron Devices*, vol. 48, no. 3, pp. 586–590, Mar. 2001, doi: 10.1109/16.906455.

[132] H. Fu *et al.*, "Demonstration of AlN Schottky Barrier Diodes With Blocking Voltage Over 1 kV," *IEEE Electron Device Lett.*, vol. 38, no. 9, pp. 1286–1289, Sep. 2017, doi: 10.1109/LED.2017.2723603.

[133] H. Chen *et al.*, "Optical Cavity Effects in InGaN Micro-Light-Emitting Diodes With Metallic Coating," *IEEE Photonics J.*, vol. 9, no. 3, pp. 1–8, Jun. 2017, doi: 10.1109/JPHOT.2017.2690389.

[134] M. Hou, H. So, A. J. Suria, A. S. Yalamarthy, and D. G. Senesky, “Suppression of Persistent Photoconductivity in AlGaN/GaN Ultraviolet Photodetectors Using In Situ Heating,” *IEEE Electron Device Lett.*, vol. 38, no. 1, pp. 56–59, Jan. 2017, doi: 10.1109/LED.2016.2626388.

[135] H. Fu, H. Chen, X. Huang, Z. Lu, and Y. Zhao, “Theoretical analysis of modulation doping effects on intersubband transition properties of semipolar AlGaN/GaN quantum well,” *J. Appl. Phys.*, vol. 121, no. 1, p. 014501, Jan. 2017, doi: 10.1063/1.4972975.

[136] H. M. Branz, W. Regan, K. J. Gerst, J. Brian Borak, and E. A. Santori, “Hybrid solar converters for maximum exergy and inexpensive dispatchable electricity,” *Energy Environ. Sci.*, vol. 8, no. 11, pp. 3083–3091, 2015, doi: 10.1039/C5EE01998B.

[137] C. J. Ercol, J. Jenkins, G. Dakermanji, A. G. Santo, and L. S. Mason, “Prototype solar panel development and testing for a Mercury orbiter spacecraft,” in *Collection of Technical Papers. 35th Intersociety Energy Conversion Engineering Conference and Exhibit (IECEC) (Cat. No.00CH37022)*, 2000, vol. 1, pp. 449–459 vol.1, doi: 10.1109/IECEC.2000.870725.

[138] G. A. Landis, D. Merritt, R. P. Raffaelle, and D. Scheiman, “High-temperature Solar Cell Development,” in *18th Space Photovoltaic Research and Technology Conference*, Paris France, 2005, pp. 241–247.

[139] A. J. Suria *et al.*, “Thickness engineering of atomic layer deposited Al2O3 films to suppress interfacial reaction and diffusion of Ni/Au gate metal in AlGaN/GaN HEMTs up to 600 °C in air,” *Appl. Phys. Lett.*, vol. 110, no. 25, p. 253505, Jun. 2017, doi: 10.1063/1.4986910.

[140] Medjdoub, F, J. F. Carlin, C. Gaquière, N. Grandjean, and E. Kohn, “Status of the Emerging InAlN/GaN Power HEMT Technology,” *Open Electr. Electron. Eng. J.*, vol. 2, no. 1, Jan. 2008.

[141] P. G. Neudeck, R. S. Okojie, and L.-Y. Chen, “High-temperature electronics - a role for wide bandgap semiconductors?,” *Proc. IEEE*, vol. 90, no. 6, pp. 1065–1076, Jun. 2002, doi: 10.1109/JPROC.2002.1021571.

[142] M. Hou and D. G. Senesky, “Operation of ohmic Ti/Al/Pt/Au multilayer contacts to GaN at 600 °C in air,” *Appl. Phys. Lett.*, vol. 105, no. 8, p. 081905, Aug. 2014, doi: 10.1063/1.4894290.

[143] S. Zhao *et al.*, “Temperature Dependence and High-Temperature Stability of the Annealed Ni/Au Ohmic Contact to p-Type GaN in Air,” *J. Electron. Mater.*, vol. 45, no. 4, pp. 2087–2091, Apr. 2016, doi: 10.1007/s11664-015-4278-3.

[144] D. Maier *et al.*, “Testing the Temperature Limits of GaN-Based HEMT Devices,” *IEEE Trans. Device Mater. Reliab.*, vol. 10, no. 4, pp. 427–436, Dec. 2010, doi: 10.1109/TDMR.2010.2072507.

[145] D. Maier *et al.*, "InAlN/GaN HEMTs for Operation in the 1000 °C Regime: A First Experiment," *IEEE Electron Device Lett.*, vol. 33, no. 7, pp. 985–987, Jul. 2012, doi: 10.1109/LED.2012.2196972.

[146] Y. Zhao *et al.*, "InGaN-based solar cells for space applications," in *2017 IEEE 60th International Midwest Symposium on Circuits and Systems (MWSCAS)*, 2017, pp. 954–957, doi: 10.1109/MWSCAS.2017.8053083.

[147] F. Iucolano, F. Roccaforte, A. Alberti, C. Bongiorno, S. Di Franco, and V. Raineri, "Temperature dependence of the specific resistance in Ti/Al/Ni/Au contacts on n-type GaN," *J. Appl. Phys.*, vol. 100, no. 12, p. 123706, Dec. 2006, doi: 10.1063/1.2400825.

[148] F. Lin *et al.*, "Temperature dependence of the specific resistance in Ti/Al/Ni/Au Ohmic contacts on (NH4)2Sx treated n-type GaN," *J. Appl. Phys.*, vol. 105, no. 9, p. 093702, May 2009, doi: 10.1063/1.3120962.

[149] J. C. Zhang *et al.*, "The influence of AlN buffer layer thickness on the properties of GaN epilayer," *J. Cryst. Growth*, vol. 268, no. 1–2, pp. 24–29, Jul. 2004, doi: 10.1016/j.jcrysgro.2004.04.102.

[150] E. Vadiee *et al.*, "High Temperature Characterization of InGaN/GaN Multi-Quantum-Well Solar Cell," in *59th Electronic Materials Conference (EMC), 2017*, 2017.

[151] N. A. K. Kaufmann *et al.*, "Thermal annealing of molecular beam epitaxy-grown InGaN/GaN single quantum well," *Semicond. Sci. Technol.*, vol. 27, no. 10, p. 105023, 2012, doi: 10.1088/0268-1242/27/10/105023.

[152] S. S. Hegedus and W. N. Shafarman, "Thin-film solar cells: device measurements and analysis," *Prog. Photovolt. Res. Appl.*, vol. 12, no. 2–3, pp. 155–176, Mar. 2004, doi: 10.1002/pip.518.

[153] A. J. Suria, A. S. Yalamarthy, H. So, and D. G. Senesky, "DC characteristics of ALD-grown Al 2 O 3 /AlGaN/GaN MIS-HEMTs and HEMTs at 600 °C in air," *Semicond. Sci. Technol.*, vol. 31, no. 11, p. 115017, 2016, doi: 10.1088/0268-1242/31/11/115017.

[154] F. Ren *et al.*, "Surface and bulk leakage currents in high breakdown GaN rectifiers," *Solid-State Electron.*, vol. 44, no. 4, pp. 619–622, Apr. 2000, doi: 10.1016/S0038-1101(99)00196-3.

[155] H. Fu, X. Huang, H. Chen, Z. Lu, and Y. Zhao, "Fabrication and Characterization of Ultra-wide Bandgap AlN-Based Schottky Diodes on Sapphire by MOCVD," *IEEE J. Electron Devices Soc.*, vol. 5, no. 6, pp. 518–524, Nov. 2017, doi: 10.1109/JEDS.2017.2751554.

[156] M. Omori, J. N. Wholey, and J. F. Gibbons, "Accelerated Active Life Test of GaAs FET and a New Failure Mode," in *18th International Reliability Physics Symposium*, 1980, pp. 134–139, doi: 10.1109/IRPS.1980.362929.

[157] E. B. Hakim, “Microelectronic reliability/temperature independence,” *Qual. Reliab. Eng. Int.*, vol. 7, no. 4, pp. 215–220, Jul. 1991, doi: 10.1002/qre.4680070405.

[158] O. V. Sulima *et al.*, “High-temperature AlGaP/GaP solar cells for NASA space missions,” in *Proceedings of 3rd World Conference onPhotovoltaic Energy Conversion, 2003*, 2003, vol. 1, pp. 737-740 Vol.1.

[159] G. A. Landis, “Solar power for near-sun, high-temperature missions,” in *2008 33rd IEEE Photovoltaic Specialists Conference*, 2008, pp. 1–5, doi: 10.1109/PVSC.2008.4922857.

[160] D. Merritt, S. Houlihan, R. P. Raffaelle, and G. A. Landis, “Wide-bandgap space solar cells,” in *Conference Record of the Thirty-first IEEE Photovoltaic Specialists Conference, 2005.*, 2005, pp. 552–555, doi: 10.1109/PVSC.2005.1488190.

[161] S. M. Goodnick *et al.*, “A hybrid concentrating solar thermal/ photovoltaic system using a high temperature III-nitride photovoltaic device,” in *Optics for Solar Energy, OSE 2014*, 2014.

[162] V. V. Tyagi, S. C. Kaushik, and S. K. Tyagi, “Advancement in solar photovoltaic/thermal (PV/T) hybrid collector technology,” *Renew. Sustain. Energy Rev.*, vol. 16, no. 3, pp. 1383–1398, Apr. 2012, doi: 10.1016/j.rser.2011.12.013.

[163] A. Maros *et al.*, “High temperature characterization of GaAs single junction solar cells,” in *Photovoltaic Specialist Conference (PVSC), 2015 IEEE 42nd*, 2015, pp. 1–5, doi: 10.1109/PVSC.2015.7356338.

[164] G. A. Landis, “Review of solar cell temperature coefficients for space,” in *13th Space Photovoltaic Research and Technology Conference (SPRAT 13)*, 1994.

[165] Z. S. Bittner, D. V. Forbes, M. Nesnidal, and S. M. Hubbard, “Gallium phosphide solar cells with indium gallium phosphide quantum wells for high temperature applications,” in *2011 37th IEEE Photovoltaic Specialists Conference*, 2011, pp. 001959–001964, doi: 10.1109/PVSC.2011.6186337.

[166] E. E. Perl, J. Simon, J. F. Geisz, M. L. Lee, D. J. Friedman, and M. A. Steiner, “Measurements and Modeling of III–V Solar Cells at High Temperatures up to 400 °C,” *IEEE J. Photovolt.*, vol. 6, no. 5, pp. 1345–1352, Sep. 2016, doi: 10.1109/JPHOTOV.2016.2582398.

[167] M. A. Steiner, J. F. Geisz, D. J. Friedman, W. J. Olavarria, A. Duda, and T. E. Moriarty, “Temperature-dependent measurements of an inverted metamorphic multijunction (IMM) solar cell,” in *2011 37th IEEE Photovoltaic Specialists Conference*, 2011, pp. 002527–002532, doi: 10.1109/PVSC.2011.6186461.

[168] G. S. Marlow, M. B. Das, and L. Tongson, “The characteristics of Au-Ge-based ohmic contacts to n-GaAs including the effects of aging,” *Solid-State Electron.*, vol. 26, no. 4, pp. 259–266, Apr. 1983, doi: 10.1016/0038-1101(83)90120-X.

[169] J. F. Muth *et al.*, "Absorption coefficient, energy gap, exciton binding energy, and recombination lifetime of GaN obtained from transmission measurements," *Appl. Phys. Lett.*, vol. 71, no. 18, pp. 2572–2574, Nov. 1997, doi: 10.1063/1.120191.

[170] M. Arif *et al.*, "Improving InGaN heterojunction solar cells efficiency using a semibulk absorber," *Sol. Energy Mater. Sol. Cells*, vol. 159, pp. 405–411, Jan. 2017, doi: 10.1016/j.solmat.2016.09.030.

[171] J. J. Wierer, A. J. Fischer, and D. D. Koleske, "The impact of piezoelectric polarization and nonradiative recombination on the performance of (0001) face GaN/InGaN photovoltaic devices," *Appl. Phys. Lett.*, vol. 96, no. 5, p. 051107, Feb. 2010, doi: 10.1063/1.3301262.

[172] M. J. DiNezza, X.-H. Zhao, S. Liu, A. P. Kirk, and Y.-H. Zhang, "Growth, steady-state, and time-resolved photoluminescence study of CdTe/MgCdTe double heterostructures on InSb substrates using molecular beam epitaxy," *Appl. Phys. Lett.*, vol. 103, no. 19, p. 193901, Nov. 2013, doi: 10.1063/1.4828984.

[173] A. T. Meney *et al.*, "Determination of the band structure of disordered AlGaInP and its influence on visible-laser characteristics," *IEEE J. Sel. Top. Quantum Electron.*, vol. 1, no. 2, pp. 697–706, Jun. 1995, doi: 10.1109/2944.401259.

[174] D. A. Browne, B. Mazumder, Y.-R. Wu, and J. S. Speck, "Electron transport in unipolar InGaN/GaN multiple quantum well structures grown by NH_3 molecular beam epitaxy," *J. Appl. Phys.*, vol. 117, no. 18, p. 185703, May 2015, doi: 10.1063/1.4919750.

[175] K. Toprasertpong, S. M. Goodnick, Y. Nakano, and M. Sugiyama, "Effective mobility for sequential carrier transport in multiple quantum well structures," *Phys. Rev. B*, vol. 96, no. 7, Aug. 2017, doi: 10.1103/PhysRevB.96.075441.

[176] E. E. Perl *et al.*, "Development of High-Bandgap AlGaInP Solar Cells Grown by Organometallic Vapor-Phase Epitaxy," *IEEE J. Photovolt.*, vol. 6, no. 3, pp. 770–776, May 2016, doi: 10.1109/JPHOTOV.2016.2537543.

[177] J. J. Becker *et al.*, "Monocrystalline 1.7-eV-Bandgap MgCdTe Solar Cell With 11.2 #x0025; Efficiency," *IEEE J. Photovolt.*, vol. PP, no. 99, pp. 1–6, 2018, doi: 10.1109/JPHOTOV.2017.2769105.

[178] J. R. Wilcox, "Solar cell temperature dependent efficiency and very high temperature efficiency limits," Ph.D., Purdue University, United States -- Indiana, 2013.

[179] S. Marcinkevičius, K. M. Kelchner, L. Y. Kuritzky, S. Nakamura, S. P. DenBaars, and J. S. Speck, "Photoexcited carrier recombination in wide *m* -plane InGaN/GaN quantum wells," *Appl. Phys. Lett.*, vol. 103, no. 11, p. 111107, Sep. 2013, doi: 10.1063/1.4820839.

[180] T. J. Badcock, M. Ali, T. Zhu, M. Pristovsek, R. A. Oliver, and A. J. Shields, "Radiative recombination mechanisms in polar and non-polar InGaN/GaN quantum well LED structures," *Appl. Phys. Lett.*, vol. 109, no. 15, p. 151110, Oct. 2016, doi: 10.1063/1.4964842.

[181] T. Langer *et al.*, “Radiative and nonradiative recombination mechanisms in nonpolar and semipolar GaInN/GaN quantum wells,” *Phys. Status Solidi B*, vol. 253, no. 1, pp. 133–139, Jan. 2016, doi: 10.1002/pssb.201552353.

[182] J. R. Lang, N. G. Young, R. M. Farrell, Y.-R. Wu, and J. S. Speck, “Carrier escape mechanism dependence on barrier thickness and temperature in InGaN quantum well solar cells,” *Appl. Phys. Lett.*, vol. 101, no. 18, p. 181105, Oct. 2012, doi: 10.1063/1.4765068.

[183] X. H. Zhao, S. Liu, C. M. Campbell, Y. Zhao, M. B. Lassise, and Y. H. Zhang, “Ultralow Interface Recombination Velocity (~1 cm/s) at CdTe/MgxCd $_1hbox-$xTe Heterointerface,” *IEEE J. Photovolt.*, vol. 7, no. 3, pp. 913–918, May 2017, doi: 10.1109/JPHOTOV.2017.2666553.

[184] E. E. Perl, D. Kuciauskas, J. Simon, D. J. Friedman, and M. A. Steiner, “Identification of the limiting factors for high-temperature GaAs, GaInP, and AlGaInP solar cells from device and carrier lifetime analysis,” *J. Appl. Phys.*, vol. 122, no. 23, p. 233102, Dec. 2017, doi: 10.1063/1.5003631.

[185] W. Li, Y. Shi, K. Chen, L. Zhu, and S. Fan, “A Comprehensive Photonic Approach for Solar Cell Cooling,” *ACS Photonics*, vol. 4, no. 4, pp. 774–782, Apr. 2017, doi: 10.1021/acsphotonics.7b00089.

[186] M. E. Nell and A. M. Barnett, “The spectral p-n junction model for tandem solar-cell design,” *IEEE Trans. Electron Devices*, vol. 34, no. 2, pp. 257–266, Feb. 1987, doi: 10.1109/T-ED.1987.22916.

[187] S. E. Sofia, N. Sahraei, J. P. Mailoa, T. Buonassisi, and I. M. Peters, “Metal Grid Contact Design for Four-Terminal Tandem Solar Cells,” *IEEE J. Photovolt.*, vol. 7, no. 3, pp. 934–940, May 2017, doi: 10.1109/JPHOTOV.2017.2686651.

[188] S. Essig *et al.*, “Progress Towards a 30% Efficient GaInP/Si Tandem Solar Cell,” *Energy Procedia*, vol. 77, pp. 464–469, Aug. 2015, doi: 10.1016/j.egypro.2015.07.066.

[189] T. Takamoto *et al.*, “InGaP/GaAs and InGaAs mechanically-stacked triple-junction solar cells,” in *Conference Record of the Twenty Sixth IEEE Photovoltaic Specialists Conference - 1997*, 1997, pp. 1031–1034, doi: 10.1109/PVSC.1997.654265.

[190] K. A. Bush *et al.*, “23.6%-efficient monolithic perovskite/silicon tandem solar cells with improved stability,” *Nat. Energy*, vol. 2, p. 17009, Feb. 2017, doi: 10.1038/nenergy.2017.9.

[191] B. Chen *et al.*, “Efficient Semitransparent Perovskite Solar Cells for 23.0%-Efficiency Perovskite/Silicon Four-Terminal Tandem Cells,” *Adv. Energy Mater.*, vol. 6, no. 19, p. 1601128, Oct. 2016, doi: 10.1002/aenm.201601128.

[192] Z. (Jason) Yu, M. Leilaeioun, and Z. Holman, “Selecting tandem partners for silicon solar cells,” *Nat. Energy*, vol. 1, no. 11, p. nenergy2016137, Sep. 2016, doi: 10.1038/nenergy.2016.137.

[193] Y. Zhao, H. Fu, G. T. Wang, and S. Nakamura, “Toward ultimate efficiency: progress and prospects on planar and 3D nanostructured nonpolar and semipolar InGaN light-emitting diodes,” *Adv. Opt. Photonics*, vol. 10, no. 1, p. 246, Mar. 2018, doi: 10.1364/AOP.10.000246.

[194] C. Weisbuch, M. Piccardo, L. Martinelli, J. Iveland, J. Peretti, and J. S. Speck, “The efficiency challenge of nitride light-emitting diodes for lighting,” *Phys. Status Solidi A*, vol. 212, no. 5, pp. 899–913, Jan. 2015, doi: 10.1002/pssa.201431868.

[195] M. Kneissl, T.-Y. Seong, J. Han, and H. Amano, “The emergence and prospects of deep-ultraviolet light-emitting diode technologies,” *Nat. Photonics*, vol. 13, no. 4, pp. 233–244, Apr. 2019, doi: 10.1038/s41566-019-0359-9.

[196] F. A. Chowdhury, M. L. Trudeau, H. Guo, and Z. Mi, “A photochemical diode artificial photosynthesis system for unassisted high efficiency overall pure water splitting,” *Nat. Commun.*, vol. 9, no. 1, p. 1707, Dec. 2018, doi: 10.1038/s41467-018-04067-1.

[197] S. Wang *et al.*, “Monolithic integration of deep ultraviolet LED with a multiplicative photoelectric converter,” *Nano Energy*, vol. 66, p. 104181, Dec. 2019, doi: 10.1016/j.nanoen.2019.104181.

[198] C.-Y. Huang *et al.*, “Mode-Hopping Phenomena in the InGaN-Based Core–Shell Nanorod Array Collective Lasing,” *ACS Photonics*, vol. 5, no. 7, pp. 2724–2729, Jul. 2018, doi: 10.1021/acsphotonics.8b00471.

[199] R. Lin, V. Mazzone, N. Alfaraj, J. Liu, X. Li, and A. Fratalocchi, “On-Chip Hyperuniform Lasers for Controllable Transitions in Disordered Systems,” *Laser Photonics Rev.*, vol. 14, no. 2, p. 1800296, Jan. 2020, doi: 10.1002/lpor.201800296.

[200] H. Amano *et al.*, “The 2018 GaN power electronics roadmap,” *J. Phys. Appl. Phys.*, vol. 51, no. 16, p. 163001, Apr. 2018, doi: 10.1088/1361-6463/aaaf9d.

[201] H. Fu *et al.*, “High Performance Vertical GaN-on-GaN p-n Power Diodes With Hydrogen-Plasma-Based Edge Termination,” *IEEE Electron Device Lett.*, vol. 39, no. 7, pp. 1018–1021, Jul. 2018, doi: 10.1109/LED.2018.2837625.

[202] T. Kachi, “Recent progress of GaN power devices for automotive applications,” *Jpn. J. Appl. Phys.*, vol. 53, no. 10, p. 100210, Sep. 2014, doi: 10.7567/JJAP.53.100210.

[203] A. Chakraborty *et al.*, “Demonstration of Nonpolar m-Plane InGaN/GaN Light-Emitting Diodes on Free-Standing m-Plane GaN Substrates,” *Jpn. J. Appl. Phys.*, vol. 44, no. 1L, p. L173, Jan. 2005, doi: 10.1143/JJAP.44.L173.

[204] K.-C. Kim *et al.*, “Improved electroluminescence on nonpolar m -plane InGaN/GaN quantum wells LEDs,” *Phys. Status Solidi RRL – Rapid Res. Lett.*, vol. 1, no. 3, pp. 125–127, Apr. 2007, doi: 10.1002/pssr.200701061.

[205] K. Okamoto, H. Ohta, S. F. Chichibu, J. Ichihara, and H. Takasu, “Continuous-Wave Operation of m-Plane InGaN Multiple Quantum Well Laser Diodes,” *Jpn. J. Appl. Phys.*, vol. 46, no. 3L, p. L187, Feb. 2007, doi: 10.1143/JJAP.46.L187.

[206] M. C. Schmidt *et al.*, “Demonstration of Nonpolar m-Plane InGaN/GaN Laser Diodes,” *Jpn. J. Appl. Phys.*, vol. 46, no. 3L, p. L190, Feb. 2007, doi: 10.1143/JJAP.46.L190.

[207] H. Fu *et al.*, “Nonpolar vertical GaN-on-GaN p–n diodes grown on free-standing $(10\bar{1}0)$ *m* -plane GaN substrates,” *Appl. Phys. Express*, vol. 11, no. 11, p. 111003, Nov. 2018, doi: 10.7567/APEX.11.111003.

[208] M. Monavarian *et al.*, “High-Voltage Regrown Nonpolar m -Plane Vertical p-n Diodes: A Step Toward Future Selective-Area-Doped Power Switches,” *IEEE Electron Device Lett.*, vol. 40, no. 3, pp. 387–390, Mar. 2019, doi: 10.1109/LED.2019.2892345.

[209] Y. Zhao *et al.*, “Indium incorporation and emission properties of nonpolar and semipolar InGaN quantum wells,” *Appl. Phys. Lett.*, vol. 100, no. 20, p. 201108, May 2012, doi: 10.1063/1.4719100.

[210] S. Nakagawa, H. Tsujimura, K. Okamoto, M. Kubota, and H. Ohta, “Temperature dependence of polarized electroluminescence from nonpolar m-plane InGaN-based light emitting diodes,” *Appl. Phys. Lett.*, vol. 91, no. 17, p. 171110, Jul. 2007, doi: 10.1063/1.2800817.

[211] K. M. Kelchner, L. Y. Kuritzky, K. Fujito, S. Nakamura, S. P. DenBaars, and J. S. Speck, “Emission characteristics of single InGaN quantum wells on misoriented nonpolar m-plane bulk GaN substrates,” *J. Cryst. Growth*, vol. 382, pp. 80–86, Nov. 2013, doi: 10.1016/j.jcrysgro.2013.08.013.

[212] W. Liu, R. Butté, A. Dussaigne, N. Grandjean, B. Deveaud, and G. Jacopin, “Carrier-density-dependent recombination dynamics of excitons and electron-hole plasma in m -plane InGaN/GaN quantum wells,” *Phys. Rev. B*, vol. 94, no. 19, Nov. 2016, doi: 10.1103/PhysRevB.94.195411.

[213] T. J. Badcock *et al.*, “Recombination mechanisms in heteroepitaxial non-polar InGaN/GaN quantum wells,” *J. Appl. Phys.*, vol. 112, no. 1, p. 013534, Jul. 2012, doi: 10.1063/1.4731730.

[214] P. Dawson, S. Schulz, R. A. Oliver, M. J. Kappers, and C. J. Humphreys, “The nature of carrier localisation in polar and nonpolar InGaN/GaN quantum wells,” *J. Appl. Phys.*, vol. 119, no. 18, p. 181505, May 2016, doi: 10.1063/1.4948237.

[215] S. Schulz *et al.*, “Structural, electronic, and optical properties of m-plane InGaN/GaN quantum wells: Insights from experiment and atomistic theory,” *Phys. Rev. B*, vol. 92, no. 23, p. 235419, Dec. 2015, doi: 10.1103/PhysRevB.92.235419.

[216] C. Mounir *et al.*, “Impact of inhomogeneous broadening on optical polarization of high-inclination semipolar and nonpolar ${\mathrm{In}}_{x}{\mathrm{Ga}}_{1\ensuremath{-}x}\mathrm{N}\text{/}\mathrm{G

aN}$ quantum wells," *Phys. Rev. B*, vol. 93, no. 23, p. 235314, Jun. 2016, doi: 10.1103/PhysRevB.93.235314.

[217] S. Marcinkevičius, K. M. Kelchner, S. Nakamura, S. P. DenBaars, and J. S. Speck, "Optical properties and carrier dynamics in m -plane InGaN quantum wells," *Phys. Status Solidi C*, vol. 11, no. 3–4, pp. 690–693, 2014, doi: 10.1002/pssc.201300430.

[218] C. Netzel *et al.*, "Strong charge carrier localization interacting with extensive nonradiative recombination in heteroepitaxially grown m-plane GaInN quantum wells," *Semicond. Sci. Technol.*, vol. 26, no. 10, p. 105017, Oct. 2011, doi: 10.1088/0268-1242/26/10/105017.

[219] S. Marcinkevičius, K. M. Kelchner, L. Y. Kuritzky, S. Nakamura, S. P. DenBaars, and J. S. Speck, "Photoexcited carrier recombination in wide m-plane InGaN/GaN quantum wells," *Appl. Phys. Lett.*, vol. 103, no. 11, p. 111107, Sep. 2013, doi: 10.1063/1.4820839.

[220] M. Shahmohammadi *et al.*, "Enhancement of Auger recombination induced by carrier localization in InGaN/GaN quantum wells," *Phys. Rev. B*, vol. 95, no. 12, p. 125314, Mar. 2017, doi: 10.1103/PhysRevB.95.125314.

[221] Q. L. Zhang, F. Y. Meng, P. A. Crozier, N. Newman, and S. Mahajan, "Effects of stress on phase separation in InxGa1−xN/GaN multiple quantum-wells," *Acta Mater.*, vol. 59, no. 10, pp. 3759–3769, Jun. 2011, doi: 10.1016/j.actamat.2010.11.020.

[222] S. Pereira *et al.*, "Compositional pulling effects in ${\mathrm{In}}_{x}{\mathrm{Ga}}_{1\ensuremath{-}x}\mathrm{N}/\mathrm{G}\mathrm{a}\mathrm{N}$ layers: A combined depth-resolved cathodoluminescence and Rutherford backscattering/channeling study," *Phys. Rev. B*, vol. 64, no. 20, p. 205311, Nov. 2001, doi: 10.1103/PhysRevB.64.205311.

[223] Y. Lee *et al.*, "Study of the Excitation Power Dependent Internal Quantum Efficiency in InGaN/GaN LEDs Grown on Patterned Sapphire Substrate," *IEEE J. Sel. Top. Quantum Electron.*, vol. 15, no. 4, pp. 1137–1143, Jul. 2009, doi: 10.1109/JSTQE.2009.2014967.

[224] H. Wang *et al.*, "Influence of excitation power and temperature on photoluminescence in InGaN/GaN multiple quantum wells," *Opt. Express*, vol. 20, no. 4, pp. 3932–3940, Feb. 2012, doi: 10.1364/OE.20.003932.

[225] P. Corfdir *et al.*, "Intrinsic dynamics of weakly and strongly confined excitons in nonpolar nitride-based heterostructures," *Phys. Rev. B*, vol. 83, no. 24, p. 245326, Jun. 2011, doi: 10.1103/PhysRevB.83.245326.

[226] J. Bellessa, V. Voliotis, R. Grousson, X. L. Wang, M. Ogura, and H. Matsuhata, "Quantum-size effects on radiative lifetimes and relaxation of excitons in semiconductor nanostructures," *Phys. Rev. B*, vol. 58, no. 15, pp. 9933–9940, Oct. 1998, doi: 10.1103/PhysRevB.58.9933.

[227] L. C. Andreani, F. Tassone, and F. Bassani, "Radiative lifetime of free excitons in quantum wells," *Solid State Commun.*, vol. 77, no. 9, pp. 641–645, Mar. 1991, doi: 10.1016/0038-1098(91)90761-J.

[228] B. Deveaud, T. C. Damen, J. Shah, and C. W. Tu, “Dynamics of exciton transfer between monolayer-flat islands in single quantum wells,” *Appl. Phys. Lett.*, vol. 51, no. 11, pp. 828–830, Sep. 1987, doi: 10.1063/1.98826.

[229] Y.-R. Wu, R. Shivaraman, K.-C. Wang, and J. S. Speck, “Analyzing the physical properties of InGaN multiple quantum well light emitting diodes from nano scale structure,” *Appl. Phys. Lett.*, vol. 101, no. 8, p. 083505, Aug. 2012, doi: 10.1063/1.4747532.

[230] S. Khatsevich and D. H. Rich, “The effects of crystallographic orientation and strain on the properties of excitonic emission from wurtzite InGaN/GaN quantum wells,” *J. Phys. Condens. Matter*, vol. 20, no. 21, p. 215223, May 2008, doi: 10.1088/0953-8984/20/21/215223.

[231] T. Zhu *et al.*, “Local carrier recombination and associated dynamics in *m* -plane InGaN/GaN quantum wells probed by picosecond cathodoluminescence,” *Appl. Phys. Lett.*, vol. 109, no. 23, p. 232103, Dec. 2016, doi: 10.1063/1.4971366.

[232] W. Bao, Z. Su, C. Zheng, J. Ning, and S. Xu, “Carrier Localization Effects in InGaN/GaN Multiple-Quantum-Wells LED Nanowires: Luminescence Quantum Efficiency Improvement and ‘Negative’ Thermal Activation Energy,” *Sci. Rep.*, vol. 6, p. 34545, Sep. 2016, doi: 10.1038/srep34545.

[233] D. V. Dinh, S. Presa, P. P. Maaskant, B. Corbett, and P. J. Parbrook, “Exciton localization in polar and semipolar ($11\bar{2}2$) In0.2Ga0.8N/GaN multiple quantum wells,” *Semicond. Sci. Technol.*, vol. 31, no. 8, p. 085006, Jun. 2016, doi: 10.1088/0268-1242/31/8/085006.

[234] T. Lu *et al.*, “Temperature-dependent photoluminescence in light-emitting diodes,” *Sci. Rep.*, vol. 4, no. 1, p. 6131, May 2015, doi: 10.1038/srep06131.

[235] X. H. Zheng *et al.*, “Influence of the deposition time of barrier layers on optical and structural properties of high-efficiency green-light-emitting InGaN/GaN multiple quantum wells,” *J. Appl. Phys.*, vol. 96, no. 4, pp. 1899–1903, Aug. 2004, doi: 10.1063/1.1769099.

[236] S. Rudin, T. L. Reinecke, and B. Segall, “Temperature-dependent exciton linewidths in semiconductors,” *Phys. Rev. B*, vol. 42, no. 17, pp. 11218–11231, Dec. 1990, doi: 10.1103/PhysRevB.42.11218.

[237] A. K. Viswanath, J. I. Lee, D. Kim, C. R. Lee, and J. Y. Leem, “Exciton-phonon interactions, exciton binding energy, and their importance in the realization of room-temperature semiconductor lasers based on GaN,” *Phys. Rev. B*, vol. 58, no. 24, pp. 16333–16339, Dec. 1998, doi: 10.1103/PhysRevB.58.16333.

[238] J. Lee, E. S. Koteles, and M. O. Vassell, “Luminescence linewidths of excitons in GaAs quantum wells below 150 K,” *Phys. Rev. B*, vol. 33, no. 8, pp. 5512–5516, Apr. 1986, doi: 10.1103/PhysRevB.33.5512.

[239] R. Seguin *et al.*, “Multi-excitonic complexes in single InGaN quantum dots,” *Appl. Phys. Lett.*, vol. 84, no. 20, pp. 4023–4025, May 2004, doi: 10.1063/1.1751214.

[240] R. Saran, A. Heuer-Jungemann, A. G. Kanaras, and R. J. Curry, “Giant Bandgap Renormalization and Exciton–Phonon Scattering in Perovskite Nanocrystals,” *Adv. Opt. Mater.*, vol. 5, no. 17, p. 1700231, Sep. 2017, doi: 10.1002/adom.201700231.

[241] A. D. Wright *et al.*, “Electron–phonon coupling in hybrid lead halide perovskites,” *Nat. Commun.*, vol. 7, no. 1, pp. 1–9, May 2016, doi: 10.1038/ncomms11755.

[242] J. Jasinski, Z. Liliental-Weber, S. Estrada, and E. Hu, “Microstructure of GaAs/GaN interfaces produced by direct wafer fusion,” *Appl. Phys. Lett.*, vol. 81, no. 17, pp. 3152–3154, Oct. 2002, doi: 10.1063/1.1515116.

[243] T. Plach, K. Hingerl, S. Tollabimazraehno, G. Hesser, V. Dragoi, and M. Wimplinger, “Mechanisms for room temperature direct wafer bonding,” *J. Appl. Phys.*, vol. 113, no. 9, p. 094905, Mar. 2013, doi: 10.1063/1.4794319.

[244] D. Liang *et al.*, “Low-Temperature, Strong SiO2-SiO2 Covalent Wafer Bonding for III–V Compound Semiconductors-to-Silicon Photonic Integrated Circuits,” *J. Electron. Mater.*, vol. 37, no. 10, pp. 1552–1559, Oct. 2008, doi: 10.1007/s11664-008-0489-1.

[245] S. Estrada *et al.*, “Wafer-fused AlGaAs/GaAs/GaN heterojunction bipolar transistor,” *Appl. Phys. Lett.*, vol. 82, no. 5, pp. 820–822, Jan. 2003, doi: 10.1063/1.1541946.

[246] F. Dimroth *et al.*, “Four-Junction Wafer-Bonded Concentrator Solar Cells,” *IEEE J. Photovolt.*, vol. 6, no. 1, pp. 343–349, Jan. 2016, doi: 10.1109/JPHOTOV.2015.2501729.

[247] A. S. Cutress Ian, “GlobalFoundries Stops All 7nm Development: Opts To Focus on Specialized Processes.” [Online]. Available: https://www.anandtech.com/show/13277/globalfoundries-stops-all-7nm-development. [Accessed: 12-Sep-2018].

[248] “Intel Won’t Have 10nm CPUs Ready Until the End of 2019 - ExtremeTech.” [Online]. Available: https://www.extremetech.com/computing/274373-intel-wont-have-10nm-cpus-ready-until-the-end-of-2019. [Accessed: 12-Sep-2018].

[249] J. D. Meindl, Q. Chen, and J. A. Davis, “Limits on Silicon Nanoelectronics for Terascale Integration,” *Science*, vol. 293, no. 5537, pp. 2044–2049, Sep. 2001, doi: 10.1126/science.293.5537.2044.

[250] J. A. del Alamo, “Nanometre-scale electronics with III–V compound semiconductors,” *Nature*, vol. 479, no. 7373, pp. 317–323, Nov. 2011, doi: 10.1038/nature10677.

[251] B. Radisavljevic, A. Radenovic, J. Brivio, V. Giacometti, and A. Kis, “Single-layer MoS2 transistors,” *Nat. Nanotechnol.*, vol. 6, no. 3, pp. 147–150, Mar. 2011, doi: 10.1038/nnano.2010.279.

[252] D. Kong *et al.*, “Ambipolar field effect in the ternary topological insulator $(Bi_xSb_{1-x})_2Te_3$ by composition tuning,” *Nat. Nanotechnol.*, vol. 6, no. 11, pp. 705–709, Nov. 2011, doi: 10.1038/nnano.2011.172.

[253] S. Choi *et al.*, “SiGe epitaxial memory for neuromorphic computing with reproducible high performance based on engineered dislocations,” *Nat. Mater.*, vol. 17, no. 4, pp. 335–340, Apr. 2018, doi: 10.1038/s41563-017-0001-5.

[254] Q. Huang *et al.*, “A novel Si tunnel FET with 36mV/dec subthreshold slope based on junction depleted-modulation through striped gate configuration,” in *2012 International Electron Devices Meeting*, 2012, pp. 8.5.1-8.5.4, doi: 10.1109/IEDM.2012.6479005.

[255] S. Salahuddin and S. Datta, “Use of Negative Capacitance to Provide Voltage Amplification for Low Power Nanoscale Devices,” *Nano Lett.*, vol. 8, no. 2, pp. 405–410, Feb. 2008, doi: 10.1021/nl071804g.

[256] H. Tian *et al.*, “A Graphene-Based Filament Transistor with Sub-10 mVdec $^{-1}$ Subthreshold Swing,” *Adv. Electron. Mater.*, vol. 4, no. 4, p. 1700608, Apr. 2018, doi: 10.1002/aelm.201700608.

[257] J. Park, D. Lee, J. Yoo, and H. Hwang, “NbO2 based threshold switch device with high operating temperature (>85 °C) for steep-slope MOSFET (~2mV/dec) with ultra-low voltage operation and improved delay time,” in *2017 IEEE International Electron Devices Meeting (IEDM)*, 2017, pp. 23.7.1-23.7.4, doi: 10.1109/IEDM.2017.8268449.

[258] N. Shukla *et al.*, “A steep-slope transistor based on abrupt electronic phase transition,” *Nat. Commun.*, vol. 6, p. 7812, Aug. 2015, doi: 10.1038/ncomms8812.

[259] A. Verma *et al.*, “Steep Sub-Boltzmann Switching in AlGaN/GaN Phase-FETs With ALD VO_2,” *IEEE Trans. Electron Devices*, vol. 65, no. 3, pp. 945–949, Mar. 2018, doi: 10.1109/TED.2018.2795105.

[260] J. Song, J. Woo, A. Prakash, D. Lee, and H. Hwang, “Threshold Selector With High Selectivity and Steep Slope for Cross-Point Memory Array,” *IEEE Electron Device Lett.*, vol. 36, no. 7, pp. 681–683, Jul. 2015, doi: 10.1109/LED.2015.2430332.

[261] J. Song *et al.*, “Monolithic integration of AgTe/TiO2 based threshold switching device with TiN liner for steep slope field-effect transistors,” in *2016 IEEE International Electron Devices Meeting (IEDM)*, 2016, pp. 25.3.1-25.3.4, doi: 10.1109/IEDM.2016.7838478.

[262] S. Lim, J. Yoo, J. Song, J. Woo, J. Park, and H. Hwang, “Excellent threshold switching device (Ioff ~ 1 pA) with atom-scale metal filament for steep slope (< 5 mV/dec), ultra low voltage (Vdd = 0.25 V) FET applications,” in *2016 IEEE International Electron Devices Meeting (IEDM)*, 2016, pp. 34.7.1-37.7.4, doi: 10.1109/IEDM.2016.7838543.

[263] S. Tappertzhofen, S. Menzel, I. Valov, and R. Waser, “Redox processes in silicon dioxide thin films using copper microelectrodes,” *Appl. Phys. Lett.*, vol. 99, no. 20, p. 203103, Nov. 2011, doi: 10.1063/1.3662013.

[264] W. Chen, H. J. Barnaby, and M. N. Kozicki, “Impedance Spectroscopy of Programmable Metallization Cells With a Thin SiO lt;sub gt;2 lt;/sub gt; Switching Layer,” *IEEE*

Electron Device Lett., vol. 37, no. 5, pp. 576–579, May 2016, doi: 10.1109/LED.2016.2542239.

[265] W. Chen, S. Tappertzhofen, H. J. Barnaby, and M. N. Kozicki, "SiO2 based conductive bridging random access memory," *J. Electroceramics*, vol. 39, no. 1, pp. 109–131, Dec. 2017, doi: 10.1007/s10832-017-0070-5.

[266] M. Lübben, S. Menzel, S. G. Park, M. Yang, R. Waser, and I. Valov, "SET kinetics of electrochemical metallization cells: influence of counter-electrodes in SiO_2/Ag based systems," *Nanotechnology*, vol. 28, no. 13, p. 135205, Mar. 2017, doi: 10.1088/1361-6528/aa5e59.

[267] A. Mehonic *et al.*, "Silicon Oxide (SiOx): A Promising Material for Resistance Switching?," *Adv. Mater.*, p. 1801187, Jun. 2018, doi: 10.1002/adma.201801187.

[268] Z. Zhang *et al.*, "Studies on High-Voltage GaN-on-Si MIS-HEMTs Using LPCVD Si_3N_4 as Gate Dielectric and Passivation Layer," *IEEE Trans. Electron Devices*, vol. 63, no. 2, pp. 731–738, Feb. 2016, doi: 10.1109/TED.2015.2510445.

[269] Z. Zhang *et al.*, "AlGaN/GaN MIS-HEMTs of Very-Low $V_sf th$ Hysteresis and Current Collapse With In-Situ Pre-Deposition Plasma Nitridation and LPCVD-Si3N4 Gate Insulator," *IEEE Electron Device Lett.*, vol. 38, no. 2, pp. 236–239, Feb. 2017, doi: 10.1109/LED.2016.2636136.

[270] K. Fu *et al.*, "Threshold switching and memory behaviors of epitaxially regrown GaN-on-GaN vertical p-n diodes with high temperature stability," *IEEE Electron Device Lett.*, pp. 1–1, 2019, doi: 10.1109/LED.2019.2891391.

[271] K. Fu *et al.*, "Investigation of GaN-on-GaN vertical p-n diode with regrown p-GaN by metalorganic chemical vapor deposition," *Appl. Phys. Lett.*, vol. 113, no. 23, p. 233502, Dec. 2018, doi: 10.1063/1.5052479.

[272] W. Chen *et al.*, "A CMOS-compatible electronic synapse device based on Cu/SiO_2/W programmable metallization cells," *Nanotechnology*, vol. 27, no. 25, p. 255202, Jun. 2016, doi: 10.1088/0957-4484/27/25/255202.

[273] W. Chen *et al.*, "A Study of Gamma-Ray Exposure of Cu–SiO$_2$ Programmable Metallization Cells," *IEEE Trans. Nucl. Sci.*, vol. 62, no. 6, pp. 2404–2411, Dec. 2015, doi: 10.1109/TNS.2015.2478883.

[274] I. Valov, R. Waser, J. R. Jameson, and M. N. Kozicki, "Electrochemical metallization memories—fundamentals, applications, prospects," *Nanotechnology*, vol. 22, no. 28, p. 289502, Jul. 2011, doi: 10.1088/0957-4484/22/28/289502.

[275] Z. Zhang *et al.*, "Fabrication of normally-off AlGaN/GaN metal–insulator–semiconductor high-electron-mobility transistors by photo-electrochemical gate recess etching in ionic liquid," *Appl. Phys. Express*, vol. 9, no. 8, p. 084102, Aug. 2016, doi: 10.7567/APEX.9.084102.

[276] T. Wu *et al.*, “Toward Understanding Positive Bias Temperature Instability in Fully Recessed-Gate GaN MISFETs,” *IEEE Trans. Electron Devices*, vol. 63, no. 5, pp. 1853–1860, May 2016, doi: 10.1109/TED.2016.2539341.

[277] J. Song *et al.*, “Steep Slope Field-Effect Transistors With Ag/TiO2-Based Threshold Switching Device,” *IEEE Electron Device Lett.*, vol. 37, no. 7, pp. 932–934, Jul. 2016, doi: 10.1109/LED.2016.2566661.

APPENDIX A

STEEP-SLOPE FIELD-EFFECT TRANSISTORS WITH ALGAN/GAN HEMT AND OXIDE BASED THRESHOLD SWITCHING DEVICE

Nowadays, the continuance of Moore's law has become quite stringent for semiconductor foundries due to the limits of physics and fabrications [247], [248]. Meanwhile, conventional Si based MOSFETs are facing the fundamental limitation of the subthreshold swing (SS) by Boltzmann's theory[249] . To keep providing faster computing systems for customers in the future generation electronics, innovative materials and technologies have been explored extensively. These include III-V compounds [250], two-dimensional (2D) materials [251], topological insulators [252] and neural networks[253].

Recently, researchers proposed to employ tunneling FETs and integrate ferroelectric materials on gate of FETs to realize the steep subthreshold switching [254], [255]. However, the average SS of these devices was larger than 30 mV/decade, which is still unsatisfying. Another effort includes adopting graphene-based resistive-switching device to achieve steep slope (sub-10 mV/decade) and low leakage current [256]. It's claimed that this filament transistor can be scaling down to sub-10 nm without sacrificing performance. Nonetheless, the repeatability and homogeneity still remain a critical challenge for such 2D material-based devices.

An alternative approach is to combine phase-change materials with conventional FETs to realize phase-FET or hyper-FET. The metal-insulator-transition (MIT, or Mott insulator) materials such as VO_2 and NbO_2 are commonly utilized on gate or source electrodes to obtain SS less than 8 mV/dec [257]–[259]. For example, a GaN-based phase-FET was demonstrated which integrated AlGaN/GaN MOS-HEMT with a VO_2 resistor [259]. Nonetheless, the claimed steep-switching occurred at the current saturation region in transfer characteristics and the SS at threshold voltages (V_{th}) has not been modulated by VO_2. In addition, Mott insulators suffer from thermal instability in high frequency

applications. Another effort includes adopting threshold switching device based on Ag and Cu to achieve steep slope (sub-5 mV/decade) and low leakage current [260]–[262].

In this study, we implemented SiO_2-based threshold switching device with the advanced AlGaN/GaN metal-insulator-semiconductor HEMTs (MIS-HEMTs) on Si substrates and demonstrated a steep-slope transistor (SST). Compared to Mott insulators, SiO_2 -based resistive random-access memory (RRAM) is favored primarily owing to the low leakage current and compatibility in the back-end-of-line (BEOL) processing in integrated circuits foundries [263]–[267]. This integrated SS-HEMT device achieved ~ 5mV/dec subthreshold swing with a transition range of over 10^5 in the transfer characteristics in both scan directions at RT. The V_{th} was also improved significantly. This SS-HEMT also inherited low leakage current (~10^{-5} μA/μm) and a high I_{ON}/I_{OFF} ratio (>10^7) from the original MIS-HEMTs. These results not only enable this novel transistor architecture to extend to other transistor systems, but also offer considerable possibilities for low-power switching and high frequency applications.

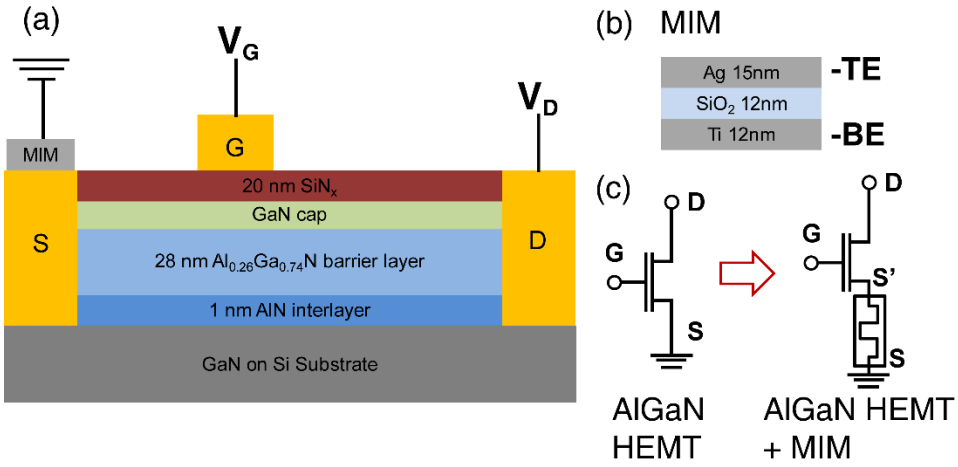

Fig. A1. (a) Schematic cross-section view of the steep-threshold-switching AlGaN MIS-HEMT, (b) schematic structure of MIM used in this study and (c) schematic circuit

diagrams of the stand-alone (left) and integrated steep-switching AlGaN MIS-HEMT device (right).

The AlGaN/GaN device epilayers for the MIS-HEMTs were grown by the metalorganic chemical vapor deposition (MOCVD) on 2-inch Si substrates. Trimethylgallium (TMGa) and trimethylaluminum (TMAl) were used as the precursors for Ga and Al, respectively, and ammonia (NH_3) was the source for N. The carrier gas is H_2. As showed in Fig. 1(a), the heterostructure consists of a highly resistive GaN buffer layer grown on a Si substrate, a 100-nm GaN channel layer, a 1 nm AlN interlayer, a 28 nm $Al_{0.26}Ga_{0.74}N$ barrier layer, and a 2 nm GaN-cap layer. A 20-nm Si_3N4 layer grown by low-pressure chemical vapor deposition (LPCVD) serves as the gate dielectrics and a passivation layer. The LPCVD-grown Si_3N_4 layer was deposited at 780 °C with ammonia (NH_3) flow of 280 sccm, a SiH_2Cl_2 flow of 70 sccm, and a deposition rate of 3.5 nm/min [268].

The AlGaN/GaN HEMTs were fabricated using the conventional photolithography. The wafer was cleaned in acetone and isopropyl alcohol under ultrasonic, and then dipped briefly in hydrochloric acid before metal depositions. Planar device isolation was achieved by multi-energy fluorine-ion implantation [269]. The LPCVD- Si_3N_4 in the source/drain contacting area was etched away by reactive ion etching (RIE). Ohmic contacts for source and drain regions were formed by e-beam evaporation of Ti/Al/Ni/Au (20/130/50/150 nm) and annealed at 890 °C for 30 s in N_2 ambient. Then gate metals were deposited by e-beam evaporation with Ni/Au (50/150nmm) and lift-off process. The gate-to-source space, the gate-to-drain space, the gate width, and the gate length are 4, 15, 100, and 4 μm, respectively. After the MIS-HEMT fabrication, a 2-D electron gas density of ~ 1×10^{13}

cm^{-2} and electron Hall mobility of ~1800 $cm^2/(V \cdot s)$ were measured at room temperature. More details on device fabrications can be found in references [269]–[271], [207]. The circuit symbols for MIS-HEMT device denoting the source (S), gate (G) and drain (D) terminals are illustrated in Fig. A1(a).

Threshold switching devices with a metal-insulator-metal (MIM) structure were then fabricated on the source contacts of the MIS-HEMT, as showed in Fig.A1 (a). Figure A1(b) shows the MIM structure including a 12 nm Ti bottom electrode (BE), a 12nm SiO_2 switching layer and a 15 nm Ag top electrode (TE), sequentially deposited by e-beam evaporation without interrupting the vacuum. Each MIM cell is circular with a diameter of 30 μm. No thermal annealing was conducted afterwards. The finial devices were denoted SS-HEMT. More details on the deposition and fabrication of SiO_2-based threshold switching cells can be found in [272]. DC characterizations of oxide-based threshold switching devices were carried out using a Keithley 2400 sourcemeter and transfer curves of the MIS-HEMTs and SS-HEMTs were performed using a Keithley 4200-SCS parameter analyzer. All measurements were performed at room temperature.

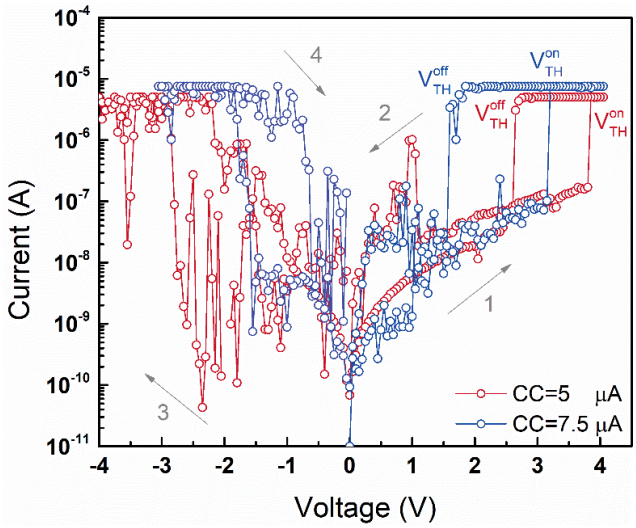

Fig. A2. Representative current–voltage characteristics of the Ag/SiO_2/Ti oxide-based threshold switching devices showing the resistive switching processes at current compliance of 5 μA (in red) and 7.5 μA (in blue). The scan sequence follows the labeled number: 1-2-3-4. "V_{TH}^{on}" and "V_{TH}^{off}" represent the threshold voltages of MIM device switching to "ON" and "OFF" states, respectively.

Figure A2 shows the representative resistive switching curves of the Ag/SiO_2/Ti oxide-based threshold switching devices at two different current compliances (I_{CC}) of 5 μA (in red) and 7.5 μA (in blue). The scan was taken at a sequence of 1-2-3-4, as labeled in the Figure A2. For each current compliance, ~ 30 cycles were conducted to ensure the device repeatability and endurance. Threshold switching devices will go from a high resistance state (HRS) to a low resistance state (LRS) or "ON" state at a threshold voltage (V_{th}). All V_{th} values are marked in the Figure 2. For I_{CC} = 7.5 μA, V_{TH}^{on} are ~ 3.7 V for positive scans and ~ −1.8V for negative scans. In contrast for I_{CC} = 5 μA, V_{TH}^{on} are ~ 3.2 V and ~ −2.8V. In addition, the ON state switched back to OFF state when the voltage sweeps back to a low level (V_{TH}^{off} =1.5V for I_{CC} = 7.5 μA and V_{TH}^{off} =2.5V for I_{CC} = 5 μA). The rectifying ratio of ~ 10^2 can be further enhanced with smaller MIM devices due to the inverse proportional relation between HRS and device size[262]. The device performance can be improved by reducing surface roughness of source electrodes and optimizing fabrication process. The possible threshold switching mechanism is proposed as the formation of unstable or even discontinuous conductive filaments at low compliance currents. More details on resistive switching mechanisms of the SiO_2-based threshold switching devices can be found in [273], [274].

Figure A3 (a) illustrates the I_D-V_{GS} transfer characteristics of the stand-alone AlGaN/GaN MIS-HEMTs at drain voltages (V_{DS}) from 3V to 9V and gate voltages (V_{GS}) from −14V to 4V in both linear and logarithmic scales. The threshold voltage for HEMT (V_{th}), defined as the voltage at a current of 10^{-2} μA/μm, was determined as −12.28 V at a V_{DS} of 6 V in the forward scan. In addition, the hysteresis of V_{th} values between forward and backward scans is also obtained from Fig. A2(b) and (c). The hysteresis of V_{th} (ΔV_{th}) is defined by the following equation: $\Delta V_{th} = V_{th}$ (backward) − V_{th} (forward). The ΔV_{th} can originate from the acceptor-like trap states in the Si_3N_4/GaN interface [275], [276]. At V_{DS} = 6 V, a low ΔV_{th} of 0.22 V was observed due to a high quality interface between GaN and Si_3N_4 grown by LPCVD [269]. It's also noteworthy that hysteresis ΔV_{th} has a tendency to reduce as V_{DS} increases. This can be ascribed to the fact that fewer electrons would be captured by those aforementioned trap states when V_{DS} increases and then the electrical stress between gate and drain (V_{GD}) reduces. The saturation drain current (I_D) at V_{GS} = 4V and V_{DS} = 9V is 515 μA/μm. The ON/OFF ratio of over 10^7 was also achieved in this stand-alone AlGaN MIS-HEMT device.

Figure A3 (b) and (c) show the I_D-V_{GS} transfer characteristics of integrated SS-HEMT at V_{DS} from 5V to 10V for both forward scans and backward scans in logarithmic scales. The steep-subthreshold-switching behaviors were clearly observed in both scan directions. This steep slope switching occurs at a huge current range from ~10^{-5} μA/μm to more than 10^2 μA/μm, indicating a high ON/OFF ratio of more than 10^7. This large current transition range of over 7 decades is 100 times greater than previous report on Ag/TiO_2-Based steep-slope transistor [277]. All subthreshold-switching values are below 5 mV/dec. In addition, the drain current (I_D) was suppressed in the SS-HEMT compared to the stand-

alone MIS-HEMT. This can be ascribed to the additional source resistance from the SiO_2-based threshold switching devices, leading to the reduction of the actual bias applied on the drain and thus the decrease of the drain current. For instance, at V_{GS} = 3V and V_{DS} = 9V, the drain current was 432 μA/μm for SS-HEMT device while it was 513 μA/μm for the stand-alone MIS-HEMT. This suppressed I_D phenomena is also consistent with previous reports on steep-slope transistors, such as AlGaN phase-FET with VO_2 [259], a Si MOSFET with NbO_2 on gate [257] and a Si MOSFET with atom switch devices based on Ag and Cu [262]. On the other hand, a positive shift in V_{th} values was observed in both scan directions compared to the standalone HEMT in Fig.A3(a). This trend is also consistent with previous work on steep-switching transistors [257]–[262], [277]. This shifting V_{TH} can be attributed to the intrinsic low leakage current and high resistance of SiO_2. SiO_2 has a huge bandgap of ~9.0 eV. This leads to the lower leakage current, larger current transition and smaller SS in our demonstrated steep-slope transistors. Once the threshold switching device is switched on, the integrated transistor will immediately rectify to the current saturation mode since the standalone HEMT is already turned on given the same gate voltage. In comparison, TiO_2 and other oxides typically have a relatively small bandgap between 3.0 and 6.0 eV. The leakage current or OFF current would be higher in transfer characteristics (I_D-V_{GS} measurements) and such steep-threshold-switching performance would be less pronounced if these oxides are adopted in our design. More details will be discussed in the later section.

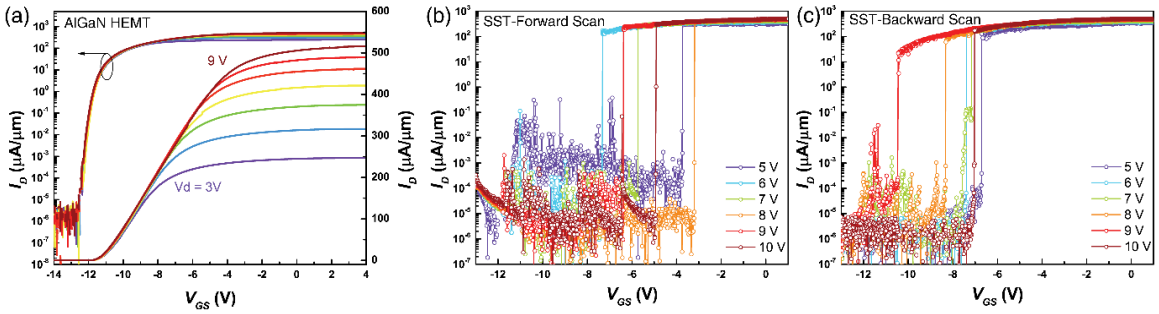

Fig. A3. The I_D-V_{GS} transfer characteristics of (a) the stand-alone AlGaN/GaN MIS-HEMTs in both logarithmic(left) and linear (right) scales, and the integrated steep-slope AlGaN/GaN HEMTs (SST) for (b) the forward scan and (c) the backward scan in logarithmic scales.

Figure A4 (a)-(h) show the extracted subthreshold swing (SS) as a function of the drain current for the integrated SS-HEMTs at V_{DS}= (a) 5 V, (b) 6V, (c) 7V, (d) 8V, (e) 9V and (f) 10V in both scan directions, and (g) for the stand-alone AlGaN/GaN MIS-HEMTs at V_{DS}= 6V. For the MIS-HEMT device, the SS values were much higher than the Boltzmann limit of 60 mV/dec at RT and the minimum values were ~ 85 mV/dec in the forward scan and ~80 mV/dec in the backward scan, respectively. With the integration of silica-based threshold switching devices, the steep subthreshold switching occurs at an abrupt transition range of drain current, which is higher than 5 orders of magnitude in forward scans [See Figure A4(a)-(f)]. Figure A4(h) shows the summary of SS values at a function of applied drain voltage V_{DS}. Starting from V_{DS}= 5 V, the SS-HEMT exhibited the steep-subthreshold-switching behavior and dropped dramatically to 1.94 mV/dec, 1.79 mV/dec, 1.47 mV/dec, 1.47 mV/dec, 1.40 mV/dec and 4.07 mV/dec at V_{DS}= 5 V, 6V, 7V, 8V, 9V and 10V in the forward scans. In backward scans, SS values were still far smaller than the Boltzmann limit of 60 mV/dec at RT, i.e., 1.81 mV/dec, 1.49 mV/dec, 2.96 mV/dec, 2.04 mV/dec, 2.02 mV/dec and 1.90 mV/dec at V_{DS}= 5 V, 6V, 7V, 8V, 9V and 10V,

respectively. It's worth pointing out that in the steep-slope ranges, SS values are comparable in both scan directions. However, this is not a general case for measurement results of more than 50 times. SS values in backward scans are generally larger than in the forward scans, which has previously been observed in the steep-switching AlGaN phase-FET with VO_2 [259]. This can be attributed to the fact that more electrons are accumulated in the SiO_2-based threshold switching devices during sweeping of V_{GS} from negative to positive range. Future work on characterizing the switching performance of this type of integrated AlGaN/GaN SS-HEMTs will be conducted to investigate the modulation capability.

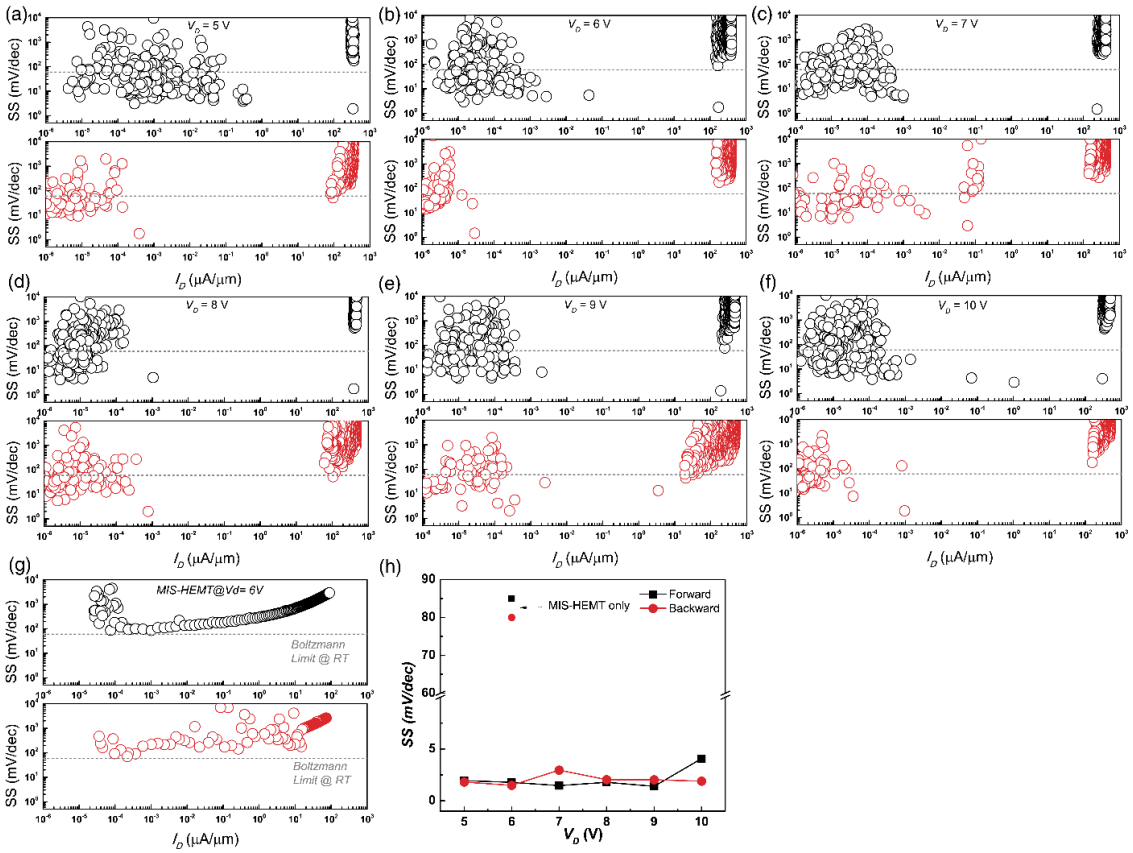

Fig. A4. The extracted subthreshold swing (SS) as a function of the drain current (I_D) for the integrated steep-switching AlGaN/GaN HEMTs (SS-HEMTs) at V_{DS}= (a) 5 V, (b) 6V,

(c) 7V, (d) 8V, (e) 9V and (f) 10V, and (g) the stand-alone AlGaN/GaN MIS-HEMTs at V_{DS}=6V. (h) shows the summary of the SS values at a function of the applied drain voltages V_{DS} of the SS-HEMT and the stand-alone HEMT at V_{DS}= 6V. All data displayed in black indicated the forward scan and the red for the backward scan. Grey dash lines indicate the subthreshold swing limit at room temperature for traditional transistor.

In order to confirm the repeatability of the steep-slope HEMT device, we performed I_{DS}-V_{GS} measurements on multiple devices for more than 50 times. Summary of V_{SS} values (defined as the gate voltage where the steep slope transition occurs) at a function of applied drain voltages V_{DS} in the SS-HEMT and the summary of SS values at a function of applied drain voltages V_{DS} are shown in the Figure A5 (a) and (b), respectively. For each sweep direction of each drain voltages V_{DS}, more than 10 I_{DS}-V_{GS} curves were chosen to calculate the statistical distribution of V_{SS} and SS values. We can see that a positive shift in all subthreshold gate voltages where the steep slope transition occurs (V_{SS}) compared to those in a normal stand-alone HEMT device (~ -12.5 V). In addition, V_{SS} in backward scans are generally more negative than these in forward scans. This can be accounted for by electron accumulation in both MIM and HEMT devices during sweeps. As for SS ranges shown in Figure 5 (b), SS appears to be more stable at around 2 to 5 mV/dec as V_{DS} increases. Future work on achieving better stability of SS and device can be incorporating GaN-based threshold switching devices [270] and improving fabrication process.

The proposed threshold switching mechanisms are concluded as follows: with the SiO_2 threshold switching device on the source of a HEMT, the original gate voltage V_{GS} is composed of 2 parts: $V_{GS'}$ and $V_{S'S}$ [see Figure A1(c)]. The $V_{S'S}$ (<0V) is equal to the condition where Ag electrode was applied a positive voltage, namely $V_{SS'}$ >0, since this is

a depletion-mode HEMT and steep switching occurs at a negative V_{GS}. There are three possible device operation scenarios:

(1) As $V_{GS} < V_{th}$ of HEMT [V_{th} (HEMT) ~ -12 V], the integrated HEMT behaves like a stand-alone HEMT and the device was turned off;

(2) As $V_{th} < V_{GS} < 0$, at a certain level of V_{GS}, $V_{S'S}$ will exceed the V_{th} of the SiO_2 threshold switching device [V_{th} (MIM)]. Then conductive filaments form between top and bottom electrodes. As the MIM device turns to LRS, the integrated transistor (HEMT in this case) will immediately rectify to the current saturation region and the steep switching occurs. This is due to the similar resistance states for both for SiO_2 MIM structure and HEMT since the OFF current is in the range from 10^{-9} to 10^{-7} A for SiO_2 MIM structure while the OFF current of HEMT is lower than 1×10^{-8} A (this is the detection limit of the setup-up).

(3) As V_{GS} sweep back, $V_{S'S}$ will exceed the V_{th} (MIM) at another certain level of V_{GS}. Then conductive filaments break, the MIM device turns to HRS, the steep switching occurs, and the transistor turns off.

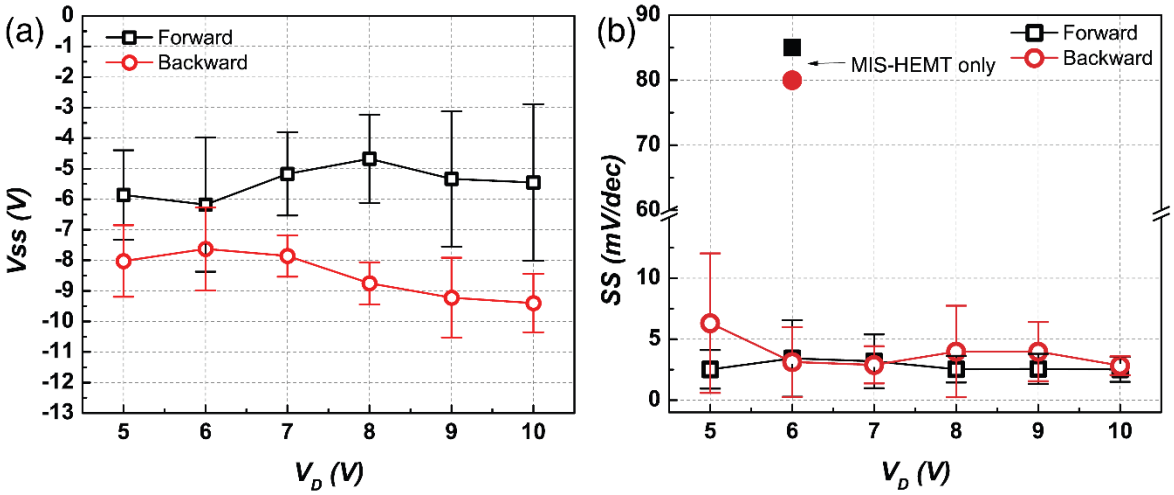

Fig. A5. (a) Summary of V_{SS} values (defined as the gate voltage where the steep slope transition occurs) at a function of applied drain voltages V_{DS} of the SS-HEMT and (b)

Summary of SS values at a function of applied drain voltages V_{DS} of the SS-HEMT. SS values of the stand-alone HEMT at V_{DS}= 6V are also plotted for reference.

In summary, we implemented the SiO_2-based threshold switching devices on the improved AlGaN/GaN MIS-HEMTs on Si substrates and demonstrated a steep-slope transistor. This integrated SS-HEMT device achieved ~ 5mV/dec subthreshold swing with a current transition range of over 10^5 in the transfer characteristics in both scan directions at RT. It also inherited low leakage current (~10^{-5} μA/μm) and a high I_{ON}/I_{OFF} ratio (>10^7) from the MIS-HEMTs. Advantages of SiO_2-based threshold switching devices include intrinsic low leakage current, facile fabrication process, CMOS-compatible and controllable switching properties. Further engineering approaches can be adopted to fabricate the steep-slope transistor with desired switching behavior. For example, an enhancement-mode GaN HEMT, III-V transistors and even Si FinFETs can also be integrated with such SiO_2-based threshold switching devices. In addition, OFF current level can be further reduced by laterally scaling down the size of MIM structure. Therefore this novel transistor design harnesses the unique properties of facile and CMOS-compatible SiO_2-based threshold switching devices and promises numerous performance advantages over conventional three-terminal transistors.